UNIVERSITY OF SÃO PAULO
POLYTHECNIC SCHOOL OF THE UNIVERSITY OF SÃO PAULO

GUSTAVO MATTOS FORTES

Anionic segregation of chloride and fluoride doped-nano ZnO: microstructure evolution, electrical conductivity and photocatalysis

São Paulo - SP
2022

GUSTAVO MATTOS FORTES

Anionic segregation of chloride and fluoride doped-nano ZnO: microstructure evolution, electrical conductivity and photocatalysis

Corrected Version

Thesis presented to the Polytechnic School of São Paulo University for the degree of Doctor in Science.

Concentration area:
Metallurgic and Materials engineering

Advisor at USP
Prof. Ph.D. Douglas Gouvêa

São Paulo - SP
2022

Este exemplar foi revisado e alterado em relação à versão original, sob responsabilidade única do autor e com a anuência de seu orientador.

São Paulo, 21 de dezembro de 2022

Assinatura do autor Gustavo Mattos Fortes

Assinatura do orientador

Catalogação-na-publicação

Fortes, Gustavo
Anionic segregation of chloride and fluoride doped-nano ZnO: microstructure evolution, electrical conductivity and photocatalysis / G. Fortes - São Paulo, 2022.
109 p.

Tese (Doutorado) - Escola Politécnica da Universidade de São Paulo. Departamento de Engenharia Metalúrgica e de Materiais.

1.ZnO nanoparticles 2.interface excess 3.selective lixiviation 4.Cl and F doping 5.artificial photosynthesis I.Universidade de São Paulo. Escola Politécnica. Departamento de Engenharia Metalúrgica e de Materiais II.t.

AGRADECIMENTOS

Primeiramente, gostaria de agradecer a minha família, pelos exemplos e ensinamentos, proporcionando o suporte essencial para eu concluir esta tese. Em especial agradeço a minha mãe pelo seu exemplo de força, dedicação e conquista, ao meu falecido pai que me ensinou a amar a vida e os seus valores, aos meus irmãos, Laura e Francisco, pelo apoio. Também à minha namorada Joseleine pela compreensão e incentivo. E agradeço a Deus pela minha vida.

Agradeço a orientação do Prof. Dr. Douglas Gouvêa, pelos ensinamentos de nano-óxidos e pela possibilidade do estágio do doutorado sanduíche. Agradeço ao Dr. Fábio Coral Fonseca pelas medidas de impedância no IPEN e pelos ensinamentos com o tratamento dos resultados destas medidas. Agradeço ao Prof. Dr. Ricardo H. R. Castro pela possibilidade do doutorado sanduíche e toda a atenção e suporte durante a estadia na UCD, em Davis, Califórnia (EUA). Agradeço ao Prof. Dr. Roland Faller pelos ensinamentos em *Molecular Dynamics*, e a paciência com o meu aprendizado desde o início. E também aos colegas de trabalho pelo convívio no laboratório e aprendizado em conjunto: André Bernardes, Matheus, Lorena, André Silva, Bruno, Cátia, Henry, Raphael, Débora. Da UCD: Isabella, Kimiko, Spencer, Luis, Profa. Vânia, Profa. Izabel, Yihan e Brad. Do IPEN: Francisco, Vivian, Vanessa.

Agradeço ao RCGI e à Shell pelo vínculo deste projeto de pesquisa. Agradeço as bolsas de doutorado durante a pesquisa concedidas por: CNPq, FUSP/RCGI, PrInt/CAPES (doutorado sanduíche), IEL (programa Inova Talentos).

Sou imensamente grato também a USP, ao PMT e seus professores e secretaria da pós-graduação, assim como ao LPC (Laboratório de Processamento Cerâmico), por toda a contribuição e estrutura para minha formação e elaboração deste trabalho.

Muito Obrigado!

"It is the nature of reason properly applied to perceive things truly, that is, as they are in themselves not as contingently existing as revealed to us by sensory experience"

– Benedict de Spinoza.

"they're developing a way to turn sunlight and water into fuel for our cars" – Barack Obama.

RESUMO

Os níveis de emissão de CO_2 na atmosfera são uma preocupação crescente devido a sua associação ao aquecimento global. Assim, são propostas soluções engenhosas como a fotossíntese artificial (FA), pois não apenas consumiriam o CO_2, mas também armazenariam energia quimicamente na forma de combustíveis. De fato, FA consiste em converter CO_2 e H_2O em moléculas orgânicas, como metano (CH_4), metanol (CH_3-OH), e etanol (C_2H_5-OH). Neste estudo, o nano-ZnO foi escolhido como fotocatalisador da FA, já que o ZnO é um semicondutor intrínseco do tipo n de largo *band gap* (E_g = 3.37 eV). Além de que sua superfície, elevada devido ao tamanho dos nano-cristalitos, apresenta uma alta afinidade para adsorver ambos CO_2 e H_2O para as reações de redução e oxidação. As dopagens com cloretos ou fluoretos foram empregadas para a nano-estabilização e para melhorar a condutividade elétrica intergranular, através do contorno de grão (CG), assim favorecendo a separação de cargas em detrimento da recombinação. As nanopartículas de ZnO foram obtidas pelo método dos precursores poliméricos e dopadas com cloretos: 0, 1, 3, 4 e 6 %mol, enquanto outras com fluoretos: 0, 1, 3, 5 e 7 %mol. As amostras em pó foram caracterizadas por DRX, FRX, BET (adsorção de N_2 para medir área superficial), picnometria a He, DRIFT e MET, enquanto pastilhas das amostras prensadas foram analisadas em espectrometria de impedância para medir a condutividade elétrica. Algumas amostras dopadas exibiram pequeno tamanho de cristalito de 23 nm e alcançaram alta área superficial específica de 18 m^2/g. As amostras apresentaram segregação dos dopantes na superfície e no CG, que beneficiou a condutividade elétrica no CG, mas dificultou a adsorção de CO_2 e H_2O na superfície. A remoção do excesso de Cl^- da superfície por lixiviação seletiva reduziu a condutividade elétrica quando comparado com as amostras originais, mas após a lixiviação, as amostras ainda apresentaram maios condutividade elétrica do que o ZnO não-dopado. A lixiviação afetou principalmente os íons de Cl^- segregados na superfície que contribuíam para o transporte de carga, possivelmente por espécies iônicas Cl^- e defeitos eletrônicos. Entretanto, o Cl^- segregado na interface sólido-sólido é menos afetado pela lixiviação. Assim, o contorno de grão do ZnO dopado com Cl^- reteve o dopante durante a lixiviação e melhorou a condutividade eletrônica. A atividade fotocatalítica do ZnO foi melhorada com a dopagem com Cl^- e a lixiviação, demonstrando a direta correlação entre um bom transporte de cargas no contorno de grão e a melhora na atividade catalítica.

Palavras-chave: nanopartículas de ZnO, dopagem com Cl^-, dopagem com F^-, excesso de interface, lixiviação seletiva, energia de interface, abatimento de CO_2, fotossíntese artificial.

ABSTRACT

CO_2 emission levels in the atmosphere are of increasing concern as it is associated with global warming. Thus, smart solutions such as artificial photosynthesis (AP) are proposed, because not only do these consume CO_2, but they also can chemically store energy as fuels. Indeed, AP consists of converting CO_2 and H_2O into organic molecules, such as methane (CH_4), methanol (CH_3-OH), and ethanol (C_2H_5-OH). In this study, nano-ZnO was selected to perform AP's photocatalytic reactions, since ZnO is an intrinsic n-type wide band gap (Eg = 3.37 eV) semiconductor. The ZnO surface, significantly increased due to the nanosized crystallites, presents a high affinity to adsorb CO_2 and H_2O for reduction/oxidation reactions. Further, chloride or fluoride doping was employed for nano-stabilization and to improve intergranular electrical conductivity through the grain boundary (GB), thus benefiting charge separation instead of recombination. The ZnO nanoparticles were prepared by polymeric precursor method and doped with chloride: 0, 1, 3, 4, and 6 mol%, while others with fluoride: 0, 1, 3, 5, and 7 mol%. Powder samples were characterized by XRD, XRF, BET (N_2 adsorption for surface area measurement), He pycnometry, DRIFT, and TEM, while pressed pellets of the samples were tested in impedance spectroscopy to measure the electrical conductivity. Some doped samples exhibited a fine crystalline size of 23 nm, and a high specific surface area of 18 m^2/g was achieved. These samples presented surface and GB dopant segregation, which demonstrated to enhance GB conductivity, but to hinder CO_2 and H_2O surface adsorption. Removing excess Cl^- from the surface by selective lixiviation decreased the electrical conductivity compared to pristine samples, but after lixiviation, samples still showed higher electrical conductivity than the undoped ZnO. Lixiviation affects mainly the surface segregated Cl^- ions that contribute to the charge transport, possibly by both Cl^- ionic species and electronic defects. On the other hand, the Cl^- segregated in the solid-solid interface is less affected by lixiviation. Thus, Cl^--doped ZnO grain boundaries retain the dopant upon lixiviation and enhance electronic conduction. The photocatalytic activity of ZnO was improved with Cl^--doping and its lixiviation, demonstrating a direct relationship between improved charge transport at the grain boundary and enhanced catalytic activity.

Keywords: ZnO nanoparticles, Cl^--doping, F^--doping, interface excess, interface energy, selective lixiviation, CO_2 abatement, artificial photosynthesis.

LIST OF FIGURES

LIST OF TABLES

LIST OF ABBREVIATIONS

AP	Artificial Photosynthesis
AC	Alternating Current
BET	Brunauer Emmett Teller
CB	Conduction Band
CVD	Chemical Vapor Deposition
DRIFT	Diffuse Reflectance Infrared Fourier Transform Spectroscopy
DSC	Differential Scanning Calorimetry
FTIR	Fourier Transform Infrared Spectroscopy
GB	Grain Boundary
HCP	Hexagonal Closed Packed
HRTEM	High Resolution Transmission Electron Microscopy
IR	Infrared (electromagnetic radiation)
ISE	Ion Selective Electrode
JCPDS	Joint Committee on Powder Diffraction Standards
NHE	Normal Hydrogen Electrode
NP	Natural Photosynthesis
PVD	Physical Vapor Deposition
RC	Resistance Capacitor
SSA	Specific Surface Area
TEM	Transmission Electron Microscopy
TOC	Transparent Oxide Conductors
TVIPS	Tietz Video and Image Processing Systems
UV	Ultraviolet (electromagnetic radiation)
VB	Valence Band
XRD	X-Ray Diffraction
XRF	X-Ray Fluorescence

LIST OF SYMBOLS

A_i	Interface area
$\mathbf{A}_{\Phi}$	Circular cross-section area of the cylindrical pellets
B4, B3, B1	Specific Strukturbericht designations (according to the Strukturbericht Journal)
bh_p	Height of the cylindrical pellets
C	Capacitance
c	Speed of light in vacuum
C_{GB}	Grain boundary capacitance
D	Diffusion coefficient
d	Thickness of the electron depletion layer
d	Crystallite size
d_{hkl}	Interplanar displacement in the crystalline lattice
E_a	Activation energy of electrical conductivity
E_g	Band gap energy
e^-	Electron
$\lvert e \rvert$	Modulus of electron charge ($\lvert e \rvert = 1.6 \text{ x } 10^{-19}$ C)
f	Alternative current frequency at the relaxation frequency
G	Gibbs free energy
$GB_{sat.}$	Grain boundary saturation
H	Enthalpy
h	Planck’s constant ($h = 6.62607015 \times 10^{-34}$ J·s)
h^+	Hole
I	Transmitted light intensity
I_0	Incident light intensity
i	Order of reflection for X-ray diffraction (always an integer number)
K	Shape factor of Scherrer formula
k	Crystal momentum
L	Particle size
l	Thickness of a medium
L_0	Initial particle size
m	Mass unit of undoped ZnO sample (ZnO-0)
M^{n+}	Metallic cation in the polymeric precursor method
N	Number of charge carriers (electron or holes)

n	Exponential of Ostwald ripening model
n	Number of electrons per m^3
$\mathrm{N_d}$	Charge carrier concentration within the electron depletion layer
${n_{Dop.}}^{bulk}$	Number of moles of dopant dissolved in the bulk of crystallites per gram of powder
${n_{Dop.}}^{GB}$	Number of moles of dopant imprisoned in the grain boundary per gram of powder
${n_{Dop.}}^{S}$	Number of moles of dopant lixiviated from the surface per gram of powder
${n_{Dop.}}^{T}$	Total number of moles of dopant per gram of powder
n_i	Number of mols at the interface
P	Pressure
p	Number of holes per m^3
R	Electrical resistance
R	Ideal gas constant (R = 8.314 J/K.mol or 0.0000862 eV/K)
r	Crystallite radius
$\mathrm{R_G}$	Grain electrical resistance
$\mathrm{R_{GB}}$	Grain boundary electrical resistance
S	Entropy
S_{BET}	Specific surface area measured by N_2 gas adsorption BET method
S_{GB}	Specific grain boundary area
S_T	Specific total interface area of crystallites
T	Temperature
t	Time
V	Unit cell volume for undoped ZnO sample (ZnO-0)
$\mathrm{V_O^{\bullet\bullet}}$	Oxygen vacancy
x_a	Solubility in the matrix (molar fraction)
$\mathrm{X_C}$	Capacitive reactance
Z’	Resistive response in impedance measurement
Z”	Reactance response in impedance measurement
$\mathrm{Zn_i^{\bullet\bullet}}$	Zinc interstitial
α	Adsorption constant
β	Full width at half maximum of peaks
Γ	Interface excess
Γ_a	Interface excess of element a
${\Gamma_{Cl}}^{GB}$	Chloride grain boundary excess
${\Gamma_{Cl}}^{S}$	Chloride surface excess

$\boldsymbol{\Gamma_{Dop.}}^{GB}$	Dopant excess at the grain boundary
$\boldsymbol{\Gamma_{Dop.}}^{S}$	Dopant excess at the surface
$\boldsymbol{\Gamma_F}^{GB}$	Fluoride grain boundary excess
$\boldsymbol{\Gamma_F}^{S}$	Fluoride surface excess
$\boldsymbol{\gamma^{GB}}$	Grain boundary energy
$\boldsymbol{\gamma_i}$	Interface energy
$\boldsymbol{\gamma^S}$	Surface energy
$\Delta \boldsymbol{H_{seg}}$	Enthalpy of segregation
$\boldsymbol{\varepsilon_0}$	Permittivity of free space (8.85 x 10^{-12} F/m)
$\boldsymbol{\varepsilon_r}$	Relative permittivity
$\boldsymbol{\theta}$	Incident X-ray angle in an X-ray diffraction analysis
$\boldsymbol{\lambda}$	Wave length
$\boldsymbol{\mu_{Dop.}}$	Chemical potential of a dopant
$\boldsymbol{\mu_e}$	Mobility of electrons
$\boldsymbol{\mu_h}$	Mobility of holes
$\boldsymbol{\mu_i}$	Chemical potential at the interface
$\boldsymbol{\rho}$	Real density
$\boldsymbol{\rho_e}$	Electrical resistivity
$\boldsymbol{\sigma}$	Electrical conductivity
$\boldsymbol{\sigma_G}$	Grain electrical conductivity
$\boldsymbol{\sigma_i}$	Intrinsic electrical conductivity
$\boldsymbol{\varphi_B}$	Potential barrier height
$\boldsymbol{\omega}$	Alternative current frequency
$\boldsymbol{\omega_0}$	Relaxation frequency

SUMMARY

1 INTRODUCTION

The increasing level of CO_2 emission in the atmosphere is causing significant environmental concerns related to global warming. Nevertheless, CO_2 is just fully oxidized carbon; thus, it can be thought of as an alternative carbon resource that could be transformed into fuel [1]. Such an idea mimic what plants do in photosynthesis; hence it was entitled artificial photosynthesis (AP), and its concept would be to convert CO_2 and H_2O into organic molecules, chemically storing energy as fuels. AP primary product outcomes obtained are methane (CH_4), methanol (CH_3-OH), and ethanol (C_2H_5-OH) [2-4].

The basic mechanism of AP is to promote a reaction between CO_2 and H_2O, in which CO_2 would be reduced, C-O bonds are broken to form C-H, while jointly H_2O would be oxidized, H-O bonds broken, forming O_2 and giving the H^+ (proton) for the CO_2 reduction. For such reactions to occur, the reactants need to be fixed to a surface that can supply charge carriers, electrons (e^-) for the CO_2 reduction, and holes (h^+) for the H_2O oxidation [5]. Conveniently, when semiconductors absorb an energetic photon, it generates a pair of e^- and h^+, which can move throughout the material and even be given at the surface. Moreover, many semiconductor oxides exhibit affinity to adsorb H_2O and CO_2 on their surface, especially ZnO [6]. Therefore, some AP approaches utilize ZnO, or systems involving ZnO, in an attempt to achieve an effective yield of photocatalysis [3, 7-9].

ZnO nanoparticles are a step further, aiming to improve AP efficiency through maximizing surface area, where CO_2 and H_2O adsorb and react. Nanosized crystallites that together usually constitute nano to micron-sized particles can have in the order of thousands of atoms/ions in an ordered assemble. Such a small atomic gather and size demand an inherent high interface area, these interfaces being between solid-gas, e.g., surfaces, and solid-solid, e.g., grain boundaries. While interfaces attribute exceptional properties to nanomaterial, these are discontinuities of high energy, which lead to the nanomaterial's main downside in achieving nanostability, as grain growth is driven to eliminate the interface energy [10].

Doping nanoparticles have been proven to enhance nanostability as the dopant segregates to the interfaces reducing its intrinsic energy [10]. Anion doping is considered a better route to attain high concentration and mobility of e^- and h^+, increasing the electrical conductivity and hindering the recombination of these charge carriers [11].

Halogens, such as Cl^- and F^-, have been shown to decrease the grain boundary potential barrier allowing a better intergranular electrical conductivity [12-15].

Therefore, in this work, we are studying Cl^- and F^--doped ZnO nanoparticles to improve the properties of the synthesized nanoparticles towards AP's efficiency. Hence, we aim for smaller crystallites, significant interface dopant-segregation, and the consequent improvement in electrical conductivity without harming CO_2 and H_2O adsorption on the surface.

2 OBJECTIVES

The main objective of this work is to obtain an improved photocatalyst by Cl^- and F^--doping ZnO nanoparticles.

As specific goals:

- To synthesize chloride or fluoride doped ZnO nanoparticles with adequate characteristics (size, specific surface area, segregation of dopants) for photocatalysis;
- To correlate grain boundary composition with its electrical conductivity;
- To verify the photocatalytic activity via photocatalytic decomposition of acetaminophen;
- To analyze how surface composition influences H_2O and CO_2 adsorption and co-adsorption preferences.
- To measure the surface and grain boundary energies of the doped and undoped nanoparticles.

3 LITERATURE REVIEW

3.1 Artificial Photosynthesis

3.1.1 CO_2 abatement

CO_2 emissions worldwide are a growing concern for humanity. Even though the major part of the CO_2 balance is related to natural cycles, the CO_2 concentration in the atmosphere has risen from 278 ppm before the pre-industrial era (18th century) to the current level of 405 ppm [16]. This 45% increase of CO_2 in the atmosphere, mainly attributed to human activities of deforestation and burning of fossil fuels [17], has achieved levels not reached since 20 million years ago [18]. The anthropogenic-related emission keeps rising at an alarming rate; this rate has been above 2 ppm/year in the last 20 years and accelerating [19], thus endangering the natural CO_2 balance. Earth's natural rate of imprisoning carbon in life forms and storing it in fossil fuel might not be able to compete with humanity's desires for energy and consumption [9]. It leads us not only, towards the environmental problem of global warming, with the increase of greenhouse effects, but also acidifying oceans, since these act as sinks and uptake extra CO_2 forming a carbonic acid [16].

An alternative way to face these alarming statistics is to consider this extra CO_2 as an available carbon resource, the essential element of all fossil fuels. Thus, artificial photosynthesis (AP) presents itself as a smart and intelligent solution to mitigate these environmental problems while simultaneously consuming a non-explored resource. The idea is to mimic how plants produce their aliment in nature, transforming CO_2, H_2O, and sunlight into carbohydrates (e.g., $6CO_2 + 6H_2O + \text{light} \rightarrow C_6H_{12}O_6 + 6O_2$) [20], but for AP producing fuels that meet humanity's machinery energy demanded. Hence, AP, via photocatalytic reactions, converts CO_2 and H_2O into organic molecules, chemically storing energy, to form products such as formic acid (CH_2O_2), formaldehyde (CH_2O), methane (CH_4), methanol (CH_3-OH), and ethanol (C_2H_5-OH) [2-4].

3.1.2 Artificial Photosynthesis concept

The word photocatalysis is of Greek origin, having the prefix “photo” derived from *phos*, meaning light, and “catalysis” derived from *katalyo*, meaning break apart or decompose [21]. The word synthesis also has a Greek origin from *sunthesis*, meaning “putting together”; hence photosynthesis is a specific case of photocatalysis because to form new molecules, it is necessary to break apart some bonds. Although there is no unanimous definition of photocatalysis, it is a process that uses light to activate a photocatalyst, which accelerates the reaction by lowering the free activation enthalpy of the reaction [21]. However, the photocatalyst is not involved in the chemical reaction itself; it is not consumed as a reactant.

The concept of AP was first published in 1912 when Giacomo Luigi Ciamician from the University of Bologna, in his lecture entitled *“The Photochemistry of the Future,”* proposed to harvest light to make CO_2 renewable [1]. Later, in 1989, Meyer [22] study of natural photosynthesis (NP) built a description of AP in a two-step reaction mechanism as it is currently understood, consisting of water photolysis and CO_2 reduction aided by light. In the range of visible and UV, electromagnetic radiation is essential to promote charge-separated states, which participate in the oxidation-reduction reactions observed in NP's mechanism. However, the first step towards AP appeared earlier in 1972, when Honda and Fujishima [23], using TiO_2, a semiconductor, and light, achieved a direct photochemical water-split (photolysis) producing H_2 and O_2, basically attaining the first-half of AP.

Today, there are five different approaches to developing AP processes [24, 25]:

1. gene-modified microorganisms;
2. hybrid systems immobilizing enzymes on electrodes;
3. metal-organic molecules;
4. photochemically/catalytically active surfaces of semiconductor particles;
5. photoelectrochemical/photoelectrocatalytic devices using semiconductors equipped with catalysts.

It was through the 4th approach that Honda and Fujishima [23] accomplished their H_2O-split feature. Although they did not intend to reduce CO_2 with light, on their work, similar methodologies exploiting TiO_2 and other semiconductive oxides successfully reached both H_2O-split and CO_2 reduction concomitantly.

Watanabe [5], in 1992, showed that pure ZnO could be used to produce methanol and methane from CO_2 and H_2O with visible light. Figure 1 represents his proposed photocatalysis mechanism that takes place on the active surfaces of semiconductors resulting in AP. CO_2 and H_2O are adsorbed on the semiconductor's surface, which absorbs photons of specific energy, from ultraviolet to visible light. The absorbed energy promotes an electron (e^-) from the valance band (VB) to the conduction band (CB), leaving a hole (h^+) in the VB. These charge carriers separately promote on the surface the H_2O-split with the h^+ (oxidation), releasing a hydrogen ion (proton, H^+), which along with the e^-, will cause the CO_2 reduction [9]. The break of C-O bonds to build C-H is the first step to forming organic molecules, forming intermediate products as formic acid (CH_2O_2) [5]. Several other reactions involve a different number of electrons to reach final products, e.g., for forming formic acid, methanol, and methane, it is required 2, 6, and 8 electrons, respectively [9].

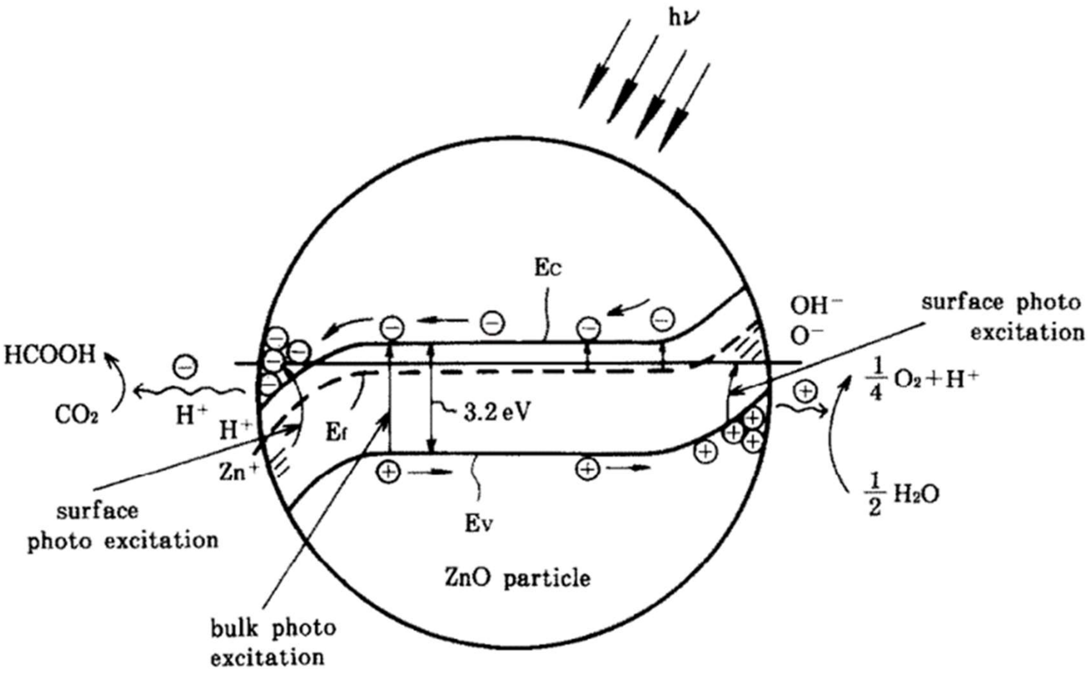

Figure 1. Photodissociation of H_2O and photoformation of formic acid from CO_2 as proposed by Watanabe [5].

In this work, AP's chosen approach uses the active surface of a semiconductor's doped-nanoparticles for photocatalysis. Other processes use semiconductors combined with catalysts, such as Pt, Rh, Pd, Ir, Ag, Au, and other noble metals [9]. Although this approach shows to be efficient, future scalability concerns point to the drawback of availability and price of noble metals. Thus, we have chosen only the oxides of more abundant elements. Metal oxides, such as TiO_2, ZnO, and SnO_2, are the leading choices for basic research and practical applications due to their high activity, low cost, high stability, nontoxicity, and chemical inertness [26]. Semiconductors by themselves present a combination of light absorption properties, electronic structure, charge transport characteristics, and excited-state lifetimes that are desirable for AP [21]. In the next section, while the AP's efficiency features are explained, the motivation and the believed enhancement for AP that this proposal offers will be clarified.

3.1.3 Efficiency features

AP is a heterogeneous photocatalytic reaction because it occurs at the photocatalyst interface immersed in the fluids (liquid or gas phase) containing reactants and products [21]. As the reaction takes place on active surfaces, increasing specific surface area (SSA) would favor adsorption of the reactants, H_2O and CO_2, tending to present a higher yield. Indeed, one of the best paths to have an edge of SSA is to use nanoparticles [9, 27], which easily reach values above 1 m^2/g of powder.

The semiconductor harvests light to create charge carriers: e^- on the CB and an h^+ in the VB. These can be separated by electric fields that are induced by the space charge layer at the interface of the fluid-semiconductor [21]. This charge separation has a particular stability depending on the band configuration and energy levels within the band gap. Still, recombination can occur if these charges are kept close to each other. Signs of recombination are characteristic light emissions detected in the photoluminescence spectroscopy [28]. Thus, created charges must move freely in the semiconductor and even through different grains; this decreases the recombination rate and enhances AP yield [3, 9, 28]. In this work, the strategy to increase intergranular conductivity was by doping the nanoparticles.

The charge carrier transfer from the photocatalyst to the adsorbed reactants is critical to the feasibility of photocatalytic reactions. The efficiency of interfacial electron transfer depends on the position of the semiconductor's VB- and CB-edges relative to the adsorbed molecule's redox potential. For the catalyst to transfer an e^-, its donor potential should be located above (more negative than) the acceptor species. Similarly, for the catalyst to transfer an h^+, or actually accept an e^-, the donor potential should be located below (more positive than) the acceptor species [21]. The H_2O oxidation reaction present a redox potentials versus Normal Hydrogen Electrode (NHE) at pH 7 of 0.82 V ($H_2O + h^+ \rightarrow 2H^+ + ½O_2$), while CO_2 reduction reactions range from −0.24 V ($CO_2 + 8H^+ + 8e^- \rightarrow CH_4 + 2\ H_2O$) to −1.9 V ($CO_2 + e^- \rightarrow CO_2^-$) [9]. The semiconductors ZnO and TiO_2 intrinsically possess the same redox potential NHE vs. V at pH 5 for the VB edge of 2.67 V, while for the CB edge, −0.41 V and −0.32 V, respectively [2]. Thus, both semiconductors have potentials in the range to transfer e^- and h^+ to CO_2 and H_2O for reduction/oxidation reactions.

There are other aspects of semiconductive doped-nanoparticles that can further improve the efficiency of AP, such as crystalline facet, surface defects, and heterojunctions (interface of two different crystalline phases) [9]. Still, these are out of the scope of the analysis.

Some of the usually explored semiconductor photocatalysts for AP are TiO_2, ZnO, α-Fe_2O_3, WO_3, CuO, $ZnFe_2O_4$, ZnO, $ZnGe_2O_4$, $ZnGa_2O_4$, g-C_3N_4, SiC, ZnS, CdS, CdSe, GaP, InP, ZnTe [9, 29]. Among these, ZnO exhibits a great affinity to adsorb both for CO_2 and H_2O [6, 7, 30-35]. Moreover, several works point out ZnO efficiency as a photocatalyst and a strong candidate for AP performance [3, 7-9].

3.2 ZnO

3.2.1 Crystalline structure

Zinc oxide (ZnO) is a semiconductor of group II-VI. At ambient conditions, its thermodynamic stable crystalline structure is wurtzite (B4), a hexagonal closed packed (HCP) structure, in which each anion presents tetrahedral coordination by four cations and vice versa [36]. This coordination is typical of sp^3 covalent bonds, but ZnO presents a considerable ionic character of 62%; thus, its chemical bonds are at the borderline between covalent and ionic semiconductors [36-38]. Another way to visualize this structure is as two interpenetrating HCP sub-lattices, one formed by Zn^{2+} and the other by O^{2-}, according to Figure 2. The lattice parameters of wurtzite are a = 3.24 Å (hexagonal size) and c = 5.20 Å (height of the hexagonal prims), and the ratio c/a = 1.63 a structure that belongs to the spatial group $P6_3mc$ [36]. The ionic radius depends on how much the bond is considered of ionic or covalent character. For purely ionic bonds, the Zn^{2+} radius varies between 0.74 Å to 0.83 Å. Whereas the O^{2-} radius varies from 1.32 Å to 1.40 Å, while the elementary radius in the predominantly covalent bonds is of 1.31 Å for the Zn and 0.66 Å for the O [39].

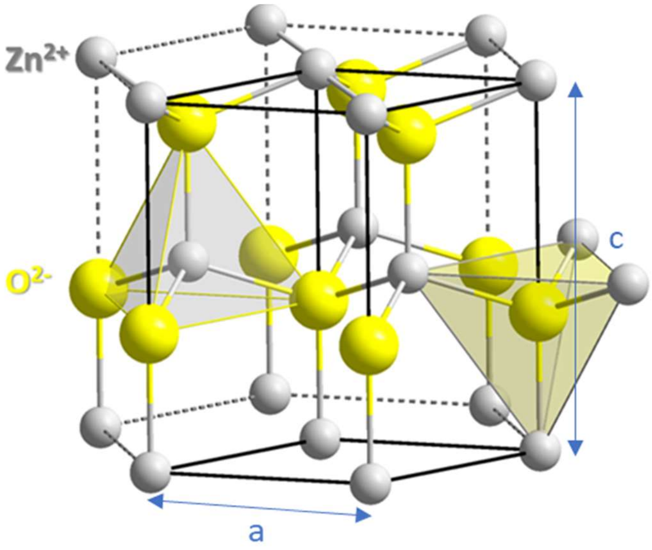

Figure 2. A representation of the ZnO wurtzite crystalline structure, where the grey spheres represent Zn^{2+} cations and the yellow ones O^{2-} anions. The lattice parameters a and c are indicated in the illustration Source: adapted from Solid State [40].

Although wurtzite is the most common phase, in some specific conditions, ZnO can assume different structures, such as the zinc blend (B3), and, more rarely, rocksalt (B1). The zinc blend, which also has sp^3 tetrahedral coordination, can be stabilized when ZnO is grown on cubic substrates. In contrast, the rocksalt (NaCl) structure, with octahedral coordination, can only be achieved in relatively high pressures [36]. Wurtzite real density (specific mass) is 5.60 g/cm^3 [41].

3.2.2 Properties and applications

Zinc oxide (ZnO) has a large variety of applications, from construction admixture to health products and optoelectronics. It can be used as a white pigment in painting and coloring [35]. In the rubber industry, ZnO accelerates sulfur-induced vulcanization mainly for tires, in which it is crucial to dissipate heat during the use [35, 42]. In concretes, an admixture of ZnO improves the resistance to water [42], and due to its antiseptic properties, it can be used as ointments for skin and wound treatment [7].

Related to ZnO's semiconductive properties, its most famously used in varistors [13, 43], but it can also be used as piezoelectric transducers, optical waveguides, acousto-optic media, transparent conductive electrodes [43], and as a sensor for hydrogen and carbon hydrides since its conductivity varies significantly with H_2 pressure [35]. Furthermore, specific for photoelectric properties, ZnO can be used in UV-blocker in suntan lotions, as transparent oxide conductors (TOC), for front contact for solar cells and liquid crystal displays [42]. There are studies of LEDs (Light-Emitting Diodes) of ZnO [36, 42]. Moreover, as a photocatalyst for organic molecules degradation [44], as well as, it seems promising for organic molecule formation [3, 7-9]. It is worth mentioning that ZnO, actually ZnO-based compounds, e.g., Cu/ZnO/Al_2O_3, have been used as a heterogeneous catalyst since 1960 for the methanol production [35]. Pure ZnO can also be used to produce methanol using CO_2 and H_2O as precursors [5].

Polycrystalline ZnO is widely used as low-resistance electrodes, as well as in thin-film transistors, solar cells, photocatalysis, artificial photosynthesis, and thermoelectric (TE) devices [45]. These materials are composed of micro/nano-crystallites joined by grain boundaries (GBs), which consist of a few atomic layers of disordered atoms. The GBs usually present several crystallographic defects such as dislocations, vacancies, interstitial, dangling bonds, and distorted bond angles. These irregularities lead to the formation of electronic states, which may have energies in the band gap, acting as trap centers for charge carriers [46]. The GBs can exhibit an electron depletion layer that induces an electric potential across the barrier that controls the charge carrier mobility. Thus, the GB region's properties play a crucial role in controlling the charge transport properties of polycrystalline materials [46].

The potential barrier at the GBs is usually described by a model used for metal oxide varistor systems [13, 47]. Electrons flow into the GBs until the Fermi level reaches the same value throughout the whole material. In the GBs, these electrons are trapped by defects, creating a negative charge at the boundary. As the local electrical neutrality must be maintained, a depletion layer, positively charged, is formed on both sides of the GB. These layers create an electrostatic field in the form of a boundary barrier, which is known as the *Double Schottky Barrier* (DSB) [13, 47]. This electric potential barrier at the GBs prevents the intergranular transport of electrons (e^-) and holes (h^+), reduces the band gap, and increases the electron-phonon non-adiabatic couplings [14], leading to an increased charge recombination [13-15]. Therefore, the composition of the GB plays a crucial role in controlling the charge transport properties of polycrystalline materials [45, 46, 48], even when in the challenging form of unsintered pressed powder. Surface-segregated dopant and adsorbed molecules also affect both the DSB at the GB by injecting or extracting electrons in the depletion layer, thus altering the barrier height [49] and the surface conductivity due to high mobile ions.

ZnO is a wide band gap semiconductor with a band gap energy (E_g) of 3.37 eV [36]. Despite the considerable large band gap that absorbs only UV-light < 368 nm, according to $E_g < h\,(c/\lambda)$, where h is Planck's constant, λ wavelength, and c the speed of light in vacuum, this value can be altered by doping which creates intermediate energy levels within the band gap. Undoped ZnO is an intrinsic n-type semiconductor, with electrons being the main charge carries due to the formation of oxygen vacancies ($\mathrm{V_O^{\cdot\cdot}}$) ($O_O^{\times} = 1/2\,O_2(\mathrm{g}) + \mathrm{V_O^{\cdot\cdot}} + 2e'$) and interstitial zinc ($\mathrm{Zn_i^{\cdot\cdot}}$) ($\mathrm{Zn_{Zn}^{\times}} + O_O^{\times} = \mathrm{Zn_i^{\cdot\cdot}} + 2\,e' + 1/2\,O_2(\mathrm{g})$) [36, 50-52], achieving very high electron density of about 10^{21} $\mathrm{cm^{-3}}$ [53]. However, it can also have an extrinsic contribution of H atoms allocated within the interstice of the lattice, which creates shallow donor states of 60 meV [36] or as has been measured around 30 to 50 meV [54-57]. For extrinsic n-type semiconductors, ZnO can also be doped with: Al, Ga, In, that substitute Zn, making high conductive films, or doped with Cl^- and I^-, substituting O^{2-} [36].

3.2.3 Photoelectronic conductivity

Electromagnetic radiation interacts with solids in a way that, from an incident beam of light, a part can be transmitted, another reflected, and yet part absorbed. The optical absorption of a material is given by the absorption constant α. Disconsidering reflection and other interference effects, the transmitted light intensity I is grated approximately by Beer's Law (Equation 1), where l is the thickness of the medium with absorption constant α and I_0 the incident light intensity [58-60].

$$I = I_0 \exp{(-\alpha l)} \tag{1}$$

Worth mentioning that α for interband absorption for semiconductors is usually large, for example, for Si near the UV has a value of 10^6 cm^{-1} (λ = 400 nm), while near the cutoff wavelength, it drops to 1 cm^{-1} (λ = 1100 nm) [61].

The intrinsic conductivity (σ_i) of a semiconductor is given by Equation 2, where $|e|$ is the modulus of electron charge ($|e|$ = 1.6 x 10^{-19} C), n and p are the number of electrons and holes per m^3, respectively; and μ_e and μ_h are the mobility of electrons and holes, respectively. For every electron promoted to the CB, a hole is left in the VB, thus $n = p$, but always $\mu_e > \mu_h$ [58].

$$\sigma_i = n\,|e|\,\mu_e + p\,|e|\,\mu_h \tag{2}$$

However, when doping elements are present in adequate content in a semiconductor, the material can exhibit extrinsic conductivity that surpasses intrinsic conductivity by creating new energy levels within the band gap extremities. Practically, all semiconductor applications demand extrinsic semiconductors [58].

When an element of higher positive valence is added to the semiconductor, it replaces a lattice element, and all its electrons will be bond to the closest neighbors, except the extra electron, which will be loosely bond at a new donor state within the band gap, but slightly below the CB. The energy required to excite a donor electron to the CB is much smaller than the band gap. Usually, the thermal energy at room temperature promotes this transition, and the free electron in the CB can conduct. Semiconductors doped this way are known as n-type semiconductors, with electrons as the major charge carriers ($n >> p$), its conduction is given by Equation 3 [58]:

$$\sigma \cong n\,|e|\mu_e \tag{3}$$

On the other hand, if an element of lower positive valence is introduced in a semiconductor, one chemical bond is left incomplete and can be represented as a hole weakly bonded to the doping atom. This doping creates a new acceptor state within the band gap yet very close above the VB. Permitting that with little energy, an electron of the VB transitions to this acceptor state, creating a hole in the VB, which conducts similarly to an electron in the CB. These semiconductors are called p-type semiconductors due to holes being their primary charge carrier ($p >> n$) its conduction is given by Equation 4 [58]:

$$\sigma \cong p\,|e|\mu_h \qquad (4)$$

The electronic configuration of compounds can lead to direct or indirect band gaps, which affect how the excitation of electrons from the VB to the CB, as illustrated in Figure 3. Figure 3 (a) demonstrates a direct band gap, the case of wurtzite ZnO, in which the VB maximum and CB minimum have the same crystal momentum (k) and hence do not require any phonon, only a photon to make the interband transition. Conversely, Figure 3 (b) shows an indirect band gap (e.g., anatase TiO_2), in which the band extrema are not aligned, thus depending on a phonon of quantified energy together with photon for the transition to occur [60, 62]. The absorption of photons and phonons is a quantized phenomenon related to their density and involves probabilistic chances of occurring [61]. The phonon energies are usually much smaller than E_g (~0.01 to 0.03 eV) so that with enough thermal energy, most phonon can be absorbed [38].

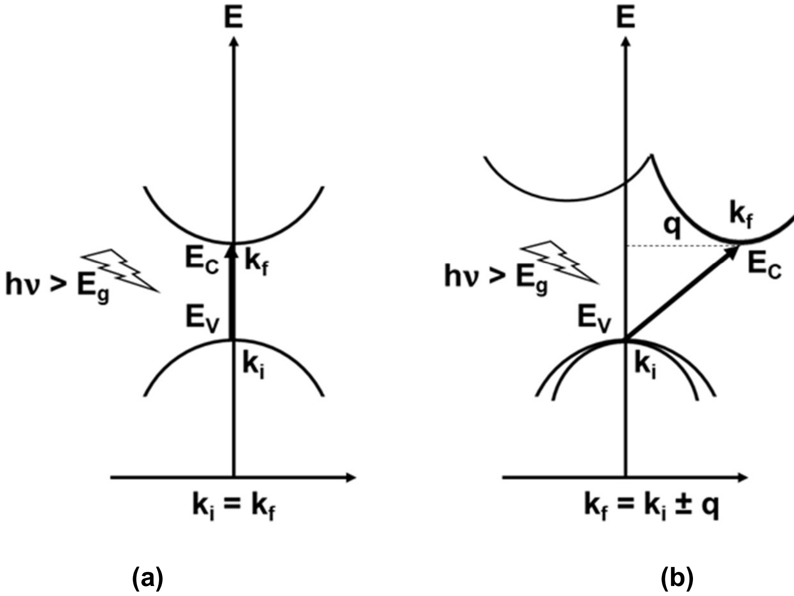

(a) (b)

Figure 3. (a) Direct and (b) indirect transitions associated with the interband absorption process in semiconductors. Source: by the author adapted from [61].

Besides, all presented regarding intragranular electrical conductivity, nanoparticles have immense GB quantities, and overcoming the know GB potential barrier is a concern. The GB potential barrier has been described by the model for metal oxide varistors systems. It mentions that metal atoms are segregated at the GB. These transition metals on the surface adsorb oxygen, which causes a concentration of electrons at the interfaces. Local electrical neutrality at the interfaces must be maintained; thus, an electron depletion region is formed adjacent to the GB and acts as a potential barrier, a Schottky-type barrier [13]. As this barrier hinders the passage of e^- and h^+, as well as reduces the band gap and increases the coupling [14], the GB is a known site for charge recombination's [13-15]. Thus, enabling a higher amount of charge carriers to pass through the GB, by enhancing its conductivity, would increase the mean free path of e^- and h^+, elongating their recombination time. Simulations have shown that Cl^--doping on the GB can decrease the coupling, thereby slowing down the recombination [14].

3.2.4 Interface energy and adsorption

ZnO hexagonal crystalline structure has on the surface the polar basal crystalline planes (0001)-Zn and $(000\bar{1})$-O, respectively, constituted of only Zn and O atoms, and the non-polar prismatic planes $(10\bar{1}0)$ and, the less common, $(11\bar{2}0)$ made of a dimer of Zn-O [35]. All these are represented in Figure 4. These surfaces have a high affinity to adsorb CO_2 and H_2O [6, 7, 30-35]. Adsorption on surfaces (facets) can be categorized as (1) Physisorption, when the adsorption energy is smaller, due to van der Waals forces, with values up to 7 or 10 kcal/mol, or (2) Chemisorption, when a stronger covalent or ionic bond is involved, which can have energies higher than 40 kcal/mol [63-65].

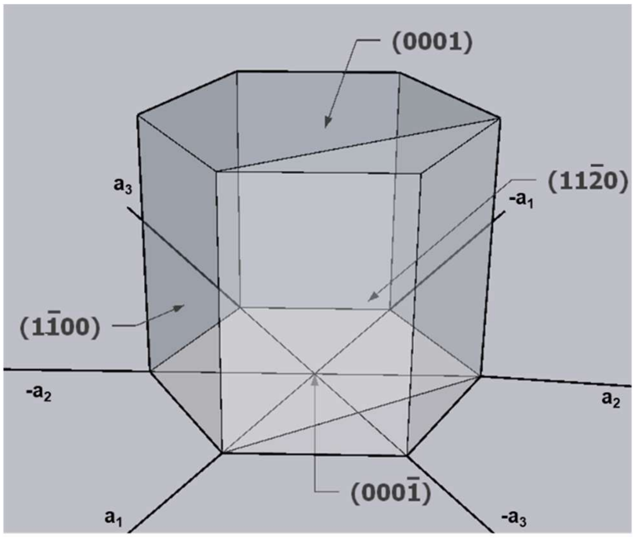

Figure 4. Principal crystalline planes for wurtzite ZnO surface. Polar planes (0001)-Zn and $(000\bar{1})$-O, and non-polar planes $(1\bar{1}00)$ and $(11\bar{2}0)$. Source: by the author adapted from Padilha (1997) [66].

The H_2O molecule adsorbs on all previously mentioned facets. The first layers are chemisorbed with a differential enthalpy of adsorption reaching values of 140 to 160 kJ/mol for coverages of 2.5 H_2O/nm^2 [6]. Water adsorbs on the $(10\bar{1}0)$ forming two stable low-energy structures that dynamically switches between them. The first adsorption structure consists of a pair of water molecules, one dissociated (H^+ and HO^- adsorbed), and one molecular H_2O adsorbed. While the second, less stable, forms a non-dissociated layer of H_2O adsorbed [30].

The polar basal surfaces (0001)-Zn and $(000\bar{1})$-O have higher surface energy calculated to be 1.23 J/m^2 and 1.11 J/m^2, respectively. Whereas, the prismatic surfaces $(10\bar{1}0)$ and $(11\bar{2}0)$ are calculated to be 0.88 J/m^2 and 0.93 J/m^2, respectively [32]. Higher surface energy makes the polar basal surfaces more favorable for adsorption. Even older studies were performed on polar surfaces already covered by a H monolayer because of the difficulty in removing it [7, 35]. On the $(000\bar{1})$-O very unstable facet, a rearrangement of $V_O^{\cdot\cdot}$ may form rows where H or dissociated water adsorbs. Over this first chemisorbed layer of H_2O, two water layers can adsorb, a stronger hydrogen bond with oxygen pointed towards the adsorbed H and a weaker with the H pointing at the first water layer [67]. On the (0001)-Zn facet, H_2O molecules are chemisorbed, with their O atom bonding with the Zn on the surface. Consequently, the H points outwards, allowing other layers of water to adsorb over the first via hydrogen bonds [34]. Another H_2O adsorption which occurs on common defect sites of the (0001)-Zn are O adatoms (adsorbed single O atom) and triangular cavities or islands. On the O adatom, H_2O chemisorbs dissociatively, while on the cavities, molecular adsorption occurs on both these defect sites the energy involved is fold-times higher than on the perfect (0001)-Zn facet [32].

CO_2 also adsorbs on all mentioned facets. The first layers are chemisorbed with a differential enthalpy of adsorption with values of 100 to 120 kJ/mol for coverages of 2.6 CO_2/nm^2 [6]. CO_2 adsorbs on the $(10\bar{1}0)$ either in the form of carbonate (CO_3^{2-}) or associated with a $V_O^{\cdot\cdot}$ forming a $(ZnCO_2)^-$ complex. As this facet consists of Zn-O dimers, CO_2 molecular physisorption occurs in a tridentate configuration, with the C atoms bonded to the surface O, while the O atoms of CO_2 bond each to different surface Zn, one of the same dimer and one of another [35].

At the polar surfaces, on the $(000\bar{1})$-O, CO_2 adsorbs forming carbonate, but in a bidentate carbonate configuration associated with a $V_O^{\cdot\cdot}$ [31, 35]. Conversely, on stochiometric (0001)-Zn facet, CO_2 adsorption is rather low, but on defective surfaces, it is significantly increased; consequently, CO_2 adsorbs on defect sites [33].

Undistinguishing the ZnO facet, CO_2 and H_2O completely adsorb on the particle's surface to decrease its surface energy. Gouvea [6] has observed that H_2O adsorption can replace adsorbed CO_2, but not the other way around. However, high-temperature desorption data showed that all water could be desorbed at 500°C, while CO_2 desorption can prevail up to 800°C, probably due to specific adsorption sites and high energy bonds [6].

3.3 Nanoparticles

3.3.1 Size and interface area

Nanomaterials are defined as refine polycrystalline materials single or multi-phased with at least one dimension in the range of 1 to 100 nm [68]. Because of these small dimensions, a considerable amount of atoms are located at the grain interface, as illustrated in Figure 5. For instance, a crystallite of 15 nm, with an interface thickness of 0.5 nm, would have roughly 20% of its atoms in its interface volume, and this amount still increases drastically with smaller crystallites [69]. Interfaces for most dry nanopowders can be of two main types: solid-gas (e.g., surfaces, pores) and solid-solid (e.g., grain boundaries).

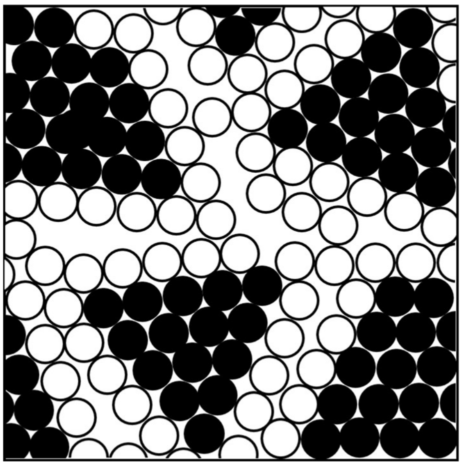

Figure 5. Representation of the bidimensional section of a nanocrystalline material, where all disks are atoms, the black ones are atoms of the bulk of crystallites, while the white ones are at the interface of crystallites. Source: by the author adapted from [68].

This more substantial fraction of interfaces for nanocrystalline than for microcrystalline materials causes significant changes in microstructure-sensitive physical and chemical properties due to: reduced grain size, crystallite form, lower overall density (because of interface contribution), and interface atoms coordination, even for materials with the same chemical composition [70, 71]. Several properties can be altered, many times enhanced by reducing grain sizes, such as self and solute diffusion, solid solubility, specific heat, magnetic properties, and mechanical properties (e.g., hardness and fracture stress) [71].

3.3.2 Synthesis method

There are two basic main approaches to synthesize nanomaterials. The first is the top-down synthesis that starts from a larger bulk and deconstructs into smaller units destructively. Examples of this method are grinding/milling, chemical etching, sputtering, laser ablation, electro-explosion [72].

The second approach is bottom-up, which consists in assembling atoms/ions from liquid/gel solutions or vapor to build up nanosized bulks. Hence, the techniques include precipitation, sol-gel techniques, chemical vapor deposition (CVD), physical vapor deposition (PVD), spinning, plasma or flame spray, laser pyrolysis, biological synthesis, hydrothermal, polymeric precursor method [72].

Based on the Maggio Pechini patent [73], and later improved by Tai and Lessing [74], the polymeric precursor method presents remarkable features to obtain nanosized oxide powder. The nanometric size particles present high specific surface area combined with a high chemical homogeneity. All in a simple process, even for doping, and that can be thought of for scalability. Thus, it was the technique chosen for this work.

3.4 Dopants segregation

3.4.1 Thermodynamics of dopant segregation

Regarding these unique properties, nanomaterials are thought for ultimate applications and even in harsh environments. However, the uniqueness of nanomaterial, large interface area, can be the cause of its failure as some of these uses require chemical, temperature, and pressure stability. For these high interface area nanomaterials, it is essential to consider the interface contribution on the total Gibbs free energy (G), as shown in Equation 5 [75]:

$$dG = -SdT + VdP + \sum \mu_i dn_i + \sum \gamma_i dA_i \tag{5}$$

In fact, on a close system, when a single particle undergoes grain growth at constant pressure, composition and high-temperature Equation 5 can be simplified to its last term, Equation 6, demonstrating how the product of interface energy (γ_i) and interface area (A_i) governs the thermal stability of polycrystalline materials regarding grain growth [75]. Thus, any increase of the term $\gamma_i dA_i$ acts as driving energy for grain growth. Coarsening is a spontaneous phenomenon for nanomaterials driven by the reduction of total free energy. Hence, nanoparticles are unstable, and coarsening is the conceivable mechanism to reduce free energy via interface area reduction.

$$dG = \sum (\gamma_i dA_i)_{T,P,n} \tag{6}$$

Nanoparticle stability is then defined as resistance against coarsening and can be managed by understanding the kinetics and thermodynamics factors involved. Ostwald ripening model, Equation 7 [76], describes the kinetics of grain growth, where K is a constant dependent on the material and temperature, n is an exponential ranging from 2 to 3, L is the particle size after time t, L_0 is the initial particle size, D is the diffusion coefficient, and γ_i is the interface energy.

$$L^{\mathrm{n}} - L_0^{\mathrm{n}} = KD\gamma_i t \tag{7}$$

Recent studies [10, 77-87] have shown that particle growth can be controlled by decreasing the interface energy γ_i, which decreases the driving energy for coarsening. From Equation 6, it can be inferred that what determines the equilibrium size of crystals is neither its minimum area nor its specific interface energy minimized, but the sum of the product of these to be at its minimum [77]. As it is harder to control the interface area, the approach tends to reduce the interface energy.

Doping nanocrystals with additives (elements) is one of the alternatives to modify interface energy and hence alter particle growth driving energy. A dopant added to crystalline material can: (1) solubilize into the bulk-forming a solid solution, (2) segregate at the interface within the host crystalline structure, or (3) after a certain threshold of concentration nucleate as a second phase possessing its own crystalline structure [10]. Ions tend to segregate to the surface and the grain boundary only if the energy balance is favorable. Thus, the interface energy decrease must be higher than the energy decrease of the solute staying in the crystalline bulk [78], for segregation to occur. As interface energy diminishes, the driving energy for grain growth drops stabilizing nanoparticles, as presented in Figure 6 [10, 79].

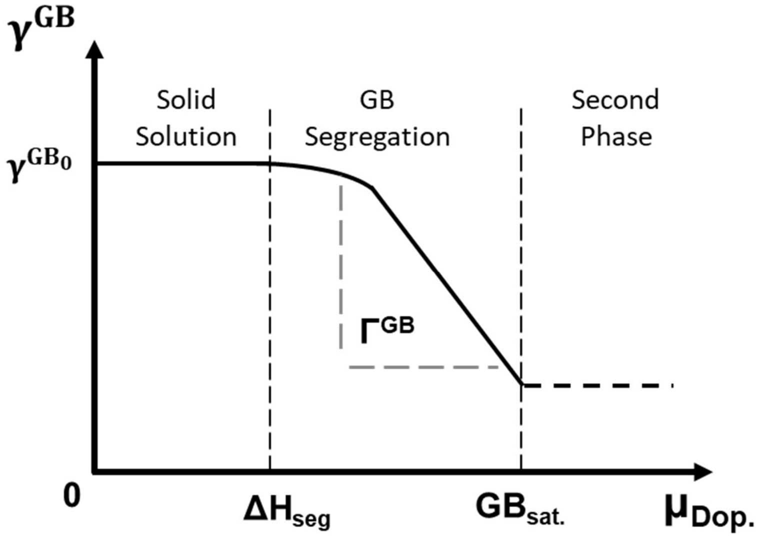

Figure 6. Schematics of how grain boundary (GB) energy varies as a function of the chemical potential of dopant ($\mu_{Dop.}$) and its distribution through the crystal. For low concentrations, a solid solution is expected without significant change in the interface energy. GB segregation directly reduces GB energy but is limited by GB saturation ($GB_{sat.}$). A higher excess will eventually cause a second phase formation. Source: by the author adapted from [10].

The interfacial segregation is driven by the enthalpy of segregation (ΔH_{seg}), which, in crystalline systems, is associated with four types of driving energies, that are (1) the difference in surface energy between the doping oxide and the host, (2) an elastic solute strain energy due to the size difference between dopant and host ions, (3) solute-solvent interaction, and (4) electrostatic potential/charge compensation [27].

Moreover, interface segregation causes a kinetic effect as it reduces the mobility of the GB. This has been shown by several metallurgy studies [88-90], in which impurity atoms or phases pin the GBs. Therefore, doping has been widely used for nano-stabilization, both in applications and to improve the sintering processes at high temperatures [80-83]. In the case of sintering and densification, the correct dosage of an additive, which is prone to segregate at the interfaces, is used to alter the interface's energy balance, increasing the thermodynamic stability of nanoparticles that hinder growth and simultaneously favoring pore elimination [10].

The thermodynamic interpretation of segregation using Gibbs Adsorption Theory, which correlates the variation of the interface energy (γ_i) due to the segregation of the solute (a), is presented in Equation 8. Where Γ_a is the interface excess (mol.m^{-2}) and x_a is the solubility in the matrix expressed as the molar fraction.

$$\Gamma_a = -\frac{\partial \gamma_i}{RT\partial ln x_a} \tag{8}$$

Equation 9, an integrated version of Equation 8, demonstrates how a direct increase of interface excess reduces the interface energy, responsible for generating higher interface stability even for high specific interface areas [75, 86, 87, 91]. In Equation 9, the interface energy of the pure material γ_0 is diminished by segregation to γ and depends on the interface excess itself, the energetic contribution of the heat of segregation ΔH_{seg}, and the solubility. Changes in temperature will alter the solubility and the heat of segregation, thus affecting the process of segregation.

$$\gamma = \gamma_0 + \Gamma_a \, . \Delta H_{seg} \tag{9}$$

As the value of γ_0 changes through dopant segregation, we might analyze Equation 7 to understand that the most affected variables are interface energy and diffusion coefficient [10], which control grain growth. These Equations 7 and 9 show that for the same time of sintering, particles with dopant segregation will result in smaller and more stable particles.

3.4.2 Role of Cl^- and F^- at the interfaces

In literature, for overall purposes, cationic doping is usually more studied than anionic doping. The electrical properties of ZnO have been modified by dopants, such as Co, Ni, In, Ga, Sn, and Cl^- [92-96]. However, anionic doping presents some compelling benefits regarding photoelectric enhancements [12, 97-99]. Instead of metallic cation, anion doping is considered a better route to obtain charge carrier concentration and mobility while maintaining high transparency. Such an advantage is because the CB of semiconductors is formed from the metal orbitals, sublevel d, and other cations would cause a disturbance in the CB, leading to an increase in scattering events, hence decreasing mobility and conductivity. Whereas in the case of anions, which possess valence electrons in sublevel p, the perturbation is restricted to the VB, and scattering of conduction electrons is minimized [11].

For Cl^--doped ZnO, it has been observed that electrical conductivity can be increased by five orders of magnitude, with a resistivity of 2 x 10^{-5} Ω.m [99]. Structurally, Cl^- is known to replace O^{2-} in the lattice [12, 36, 97, 100, 101] causing lattice expansion due to its larger ionic radius, r(O^{2-}) = 0.140 nm, while r(Cl^-) = 0.181 nm, i.e. 29% larger, mainly tensile strain in the c-axis [97, 98]. The calculated lattice strain of *c* for Cl^--doped ZnO is 0.30% [97]. Computational simulations demonstrated that the nearest neighbor O-Zn for a perfect ZnO is 1.95 Å. At the same time, the Cl-Zn bond in ZnO is 2.33 Å, also showing that the energy of formation of interstitial Cl^- is much higher and unlikely to occur than Cl^- substituting O^{2-} in the lattice [101]. Another study found similar values for stochiometric ZnO the O-Zn bond length is 1.97 Å, while Cl-Zn ranges from 2.38-2.43 Å in ZnO [102]. Oxygen vacancy makes pure ZnO an n-type intrinsic semiconductor, as this defect creates a donor-type low energy level; therefore, it is valuable for the ZnO conductivity [103]. Although, halogens tend to passivate $V_O^{\cdot\cdot}$, attributed to the green light emission (~530nm), and with higher Cl^- concentration increasing V_{Zn}” associated to blue emission (~630nm) [98, 100], it does not diminish conductivity, but improves it, by mechanisms still not fully understood. Another significant contribution of Cl^- doping is how it modifies morphology. Increasing dosages cause crystallites to shift from hexagonal section long needle or equiaxial particles to hexagonal disks or even flakes [100]. Favoring ZnO polar facets, which have different semiconducting characteristics with an indirect band gap of 0.34 eV [32]. This relatively low band gap enables the harvest of visible light, and the indirect band gap hinders the recombination of opposite charges, facilitating its separation. Making Cl^--doped ZnO a material of high potential for photocatalytic applications [12].

F^--doped ZnO is already an usual option for transparent oxide conductors (TOC), but F^--doped SnO2 is still widely the most used TOC [11]. F^--Doping has been extensively studied, and the resulting materials show excellent electrical and optical properties [104-106]. Structurally, as F^- (r(F^-) = 0.133 nm) is 5% smaller than O^{2-} (r(O^{2-}) = 0.140 nm), the replacement in the lattice [12, 97, 105] causes lattice shrinkage, compressive strain, mainly along the c-axis [97, 98]. The calculated lattice strain of *c* for F^--doped ZnO is -0.035% [97], even with the predicted bond length of F-Zn (2.11 Å) longer than (O-Zn 1.95 Å) [101]. Despite the relatively low electron concentration of F^--doped ZnO (2 x 10^{20} cm^{-3}) in comparison to other TOC, it is higher than pure ZnO (7 x 10^{19} cm^{-3}). It has the advantages of highest transparency, most resistance to H plasma reduction, low price and lowest toxicity [11]. Therefore, F^--doped ZnO presents a great combination of characteristics for photovoltaic/solar cells [106], heat mirror [105], and thus potentially for photocatalysis.

The relevance of the surface species in catalysis, a common topic of concern is the segregation of the dopants in that interface. Notably, the presence of Cl^- at the ZnO surface is reported to be responsible for catalyst deactivation due to the formation of Zinc

Chloride ($ZnCl_2$), a phenomenon known as *chloride poisoning* [107]. However, this is not a permanent structural damage, as this very soluble salt can be washed out, restoring the catalytic activity of the doped ZnO [107]. The ZnO surface at neutral pH (~7) is positively charged, and soluble Cl^- would be strongly adsorbed, hindering the adsorption of organic reactants [108]. In the particular case of photocatalysis, the adsorbed Cl^- sterically blocks the adsorption of organic molecules inhibiting the photocatalytic process, while consuming the photogenerated holes, hindering the formation of highly-reactive oxygen species, responsible for the oxidation of organic pollutants [109]. The photodegradation processes are driven by reactive radicals, which are formed by photogenerated electrons and holes. The e^- reacts with oxygen molecules (O_2) to produce superoxide anions ($\bullet O^{2-}$), whereas h^+ react with water molecules or hydroxide ion (OH^-) to produce hydroxyl radicals ($\bullet OH$) [110]. These powerful oxidizing radicals can oxidize many organic compounds, e.g., acetaminophen can be degraded into CO_2, H_2O, and mineral acids [110].

Considering the contrasting effects of Cl^- on the properties of doped ZnO, the present study aims at a well-established selective lixiviation method [27] to remove most of the Cl^- from the surface to reduce the poisoning effect while preserving the Cl^- in the GB to enhance electronic conductivity, hindering e^-/h^+ recombination, thus improving the photocatalytic activity.

4 METHODS AND TECHNIQUES

4.1 Synthesis of Cl^- and F^--doped ZnO powder

4.1.1 Polymeric precursor method

The polymeric precursor method consists of complexing a specific cation by carboxylic acid groups, followed by a polyesterification of the monomer with the complexes using a polyalcohol. Later, the polymeric resin is burned to remove carbon and other volatiles, thus obtaining the oxide. The most used reagents are citric acid as a carboxylic acid, ethylene glycol as a polyalcohol, and salts (nitrates, chlorides, carbonates, hydroxides, and isopropoxides) as a source of cations [111].

Specifically, for this work, the reactants and the quantities used were: 45.8 wt-% of anhydrous citric acid (Synth, $C_6H_8O_7$) and 30.5 wt-% of ethylene glycol (Synth, $C_2H_6O_2$) to form the polymeric matrix and 23.6 wt-% of hydrated zinc nitrate (Synth, $Zn(NO_3)_2.6H_2O$) as the source of Zn. In the first step, the citric acid dissolution in ethylene glycol was carried out at 70 ± 10°C, followed by the zinc nitrate dissolution, in both cases observing the homogeneity and the transparency of the solution. Then the temperature was raised to 120 ± 5°C to trigger the polymerization. The complete desired polyesterification was achieved after 15 to 20 minutes at this temperature, while volatiles were eliminated, such as NO_x (orange smoke) from the nitrates and H_2O as a co-product of the polyesterification. In the formed polymer, the complexed Zn^{2+} is homogeneously distributed throughout the polymeric chains [112]. Figure 7 illustrates the mechanism of complexation of the cation (M^{n+}) and the polyesterification reaction. During the polyesterification, small quantities of distilled water can be added to aid the release of NO_x and to control the viscosity of the resin.

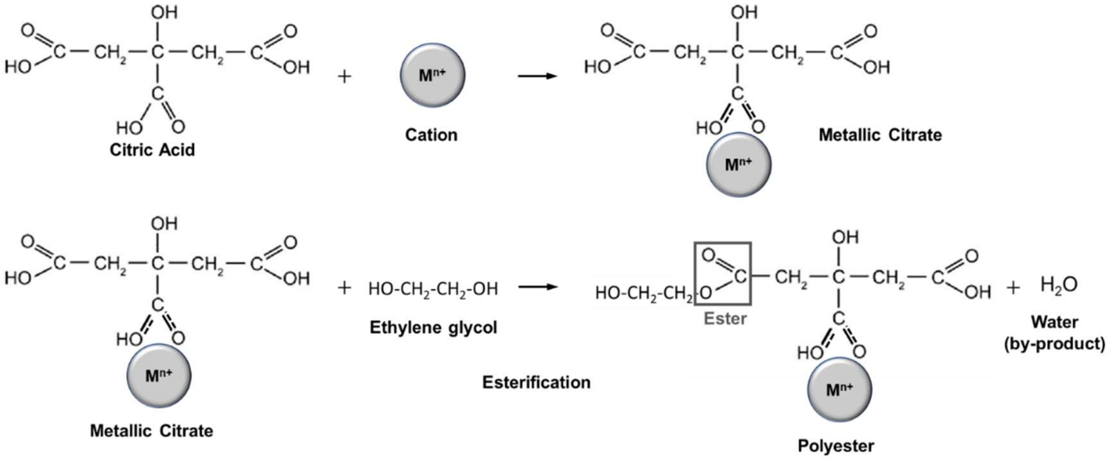

Figure 7. Mechanism of complexation and polyesterification, steps of polymeric precursors method. Source: by the author adapted from [113].

4.1.2 Doping and calcination

Besides the pure sample, the doping anions were added into the zinc resin as aqueous solutions of NH_4Cl (Synth) and NH_4F (Synth), for the Cl^- and F^-, respectively. Both solutions had a concentration of 0.24 M and were added into the resin with magnetic agitation at around 60°C. The Cl^--doping aimed for 1, 3, 4, and 6 mol% while the F^--doping targeted 1, 3, 5, and 7 mol%. The calcination was carried out in 2 steps, both at 360°C under excess air in the furnace, the first for 5 h to pyrolyze most of the resin, and the second, after mortar grinding, for 15 h to finish the oxidation of residual carbon and stabilize particle size.

4.2 Characterization techniques

4.2.1 X-ray fluorescence

X-ray fluorescence (XRF) is a chemical analysis technique in which X-Ray photons interact with the sample removing an electron from inner orbitals. As electrons from outer orbitals decay to fill the vacant orbital, a fluorescence photon is emitted. This fluorescence is of characteristic energy according to the element, enabling it to identify and quantify the element. Results are given in weight %, and usually, cations are expressed in their oxide form, while anions (i.e., Cl^- and F^-) in elemental form.

The equipment used was a Zetium (Malvern Panalytical). The powder samples were pressed before the measurement. Usually, XRFs can analyze a range of elements from fluorine to uranium.

4.2.2 Ion selective electrode

The ion selective electrode (ISE) is a technique that uses a sensor to convert a specific ion's activity in a solution into an electrical potential. The voltage usually expressed in mV is measured in a potentiometer to which the ISE is connected. This voltage depends on the logarithm of the ionic activity, according to the Nernst equation [114]. Hence, a calibration with known concentration solutions is always needed to link this value to a voltage. Preferably with a wider concentration range than the sample. Nernst equation can be linearized to $y = ax + b$, where y is the voltage in mV, a and b are constants from the line obtained during the calibration, and x is – log [ion] (minus logarithm of the ion concentration). Thus, $10^{(-1)(-\log[\text{ion}])}$ will be the concentration in mol/l.

Chloride selective electrode can measure in the range of 1 to 5×10^{-5} mol/l, and the solution needs to be at a pH of 2 to 11. Fluoride selective electrode is even more precise, measuring in the range of 1 to 10^{-7} mol/l but demands a narrower pH range of 5 to 8. Still, both use solid-state membranes in the electrode's tip, which adsorbs preferably the desired ions [114].

A precise determination of Cl^- and F^- was done using the respective ISE from Hanna Instruments, connected to a potentiometer pH300M from Analyser. For total dopant content, an amount of ~50 mg of each sample was totally dissolved in 10 ml of 1 N H_2SO_4 solution and further neutralized with 6 ml of 2 M KOH solution to fit the pH operation range of the electrodes. The segregated Cl^- and F^- at the surface of ZnO nanoparticles were measured by selective lixiviation of ~200 mg of each sample using 1.8 ml of distilled water as a solvent and submitted to ultrasound agitation for 1h. The supernatant was separated from solid ZnO by centrifugation twice at 13,000 rpm, 10,390 G-force.

4.2.3 X-ray diffraction

X-ray diffraction (XRD) is a technique mainly used for crystalline phase identification, but it also supplies information about crystallite size, lattice strain, and lattice parameters. X-rays are electromagnetic radiation of high energy and wavelengths in the order of atomic spacing in solids. When a beam of X-rays reaches a crystal, phenoms of absorption, transmission, and diffraction will occur, however, XRD's geometrical configuration is built to collect the latter signal [58]. The X-Ray diffracted from a crystalline phase can result in either constructive or destructive inference depending on the incident angle, as visualized in Figure 8. This phenomenon is represented by Bragg's law (Equation 10), where d_{hkl} is interplanar displacement, θ is the incident angle, λ is the X-ray's wavelength, and i is the order of reflection, always an integer number. When Bragg's law is obeyed, an ideal combination of θ, d_{hkl}, and λ causes a constructive interference supplying a signal to generate a diffractogram, a characteristic set of peaks at specific angles that are unique to each crystalline phase [58].

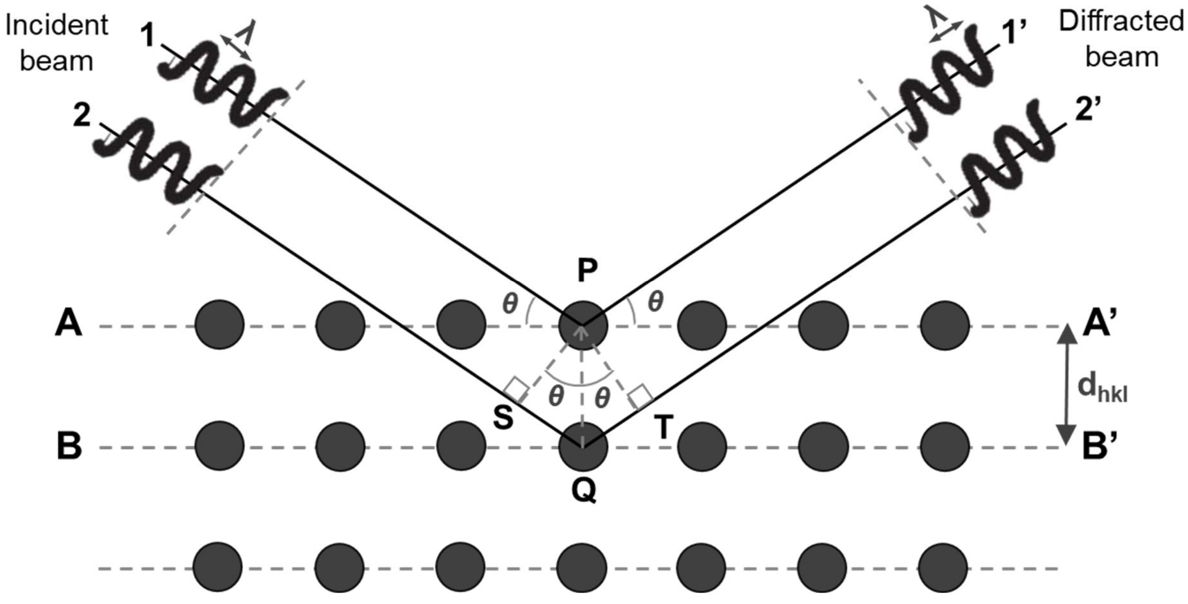

Figure 8. Schematic illustration of constructive X-ray interference on a crystalline material according to Bragg's law. The diffraction occurred on crystalline planes A-A' and B-B', and in both cases, the incident and diffracted beam have their pair of rays 1, 2 and 1', 2' in phase with each other. Source: by the author adapted from [58].

$$2\ d_{hkl}\ sen\theta = i\lambda \tag{10}$$

From the diffractogram, the crystallite size can be calculated by some methods. The Rietveld method is one of these, which utilizes a refinement by least-squares to obtain the best fit for the theoretical diffractogram. Then it is calculated through models of chemical composition, crystalline structure, operational parameters, and mainly the real sample's diffractogram. All this fitting is done point-by-point; thus, XRD measurement for size and strain purposes is usually done with a low angular pace allowing a more significant amount of data to be collected to improve the size-strain precision analysis [115].

Another tool that gives a direct and comparative idea of crystallite size is the Scherrer formula presented in Equation 11, where d is crystallite size, λ is the X-ray's wavelength, β is the full width at half maximum of peaks, and K is a shape factor that can range from 0.62 to 2.08 but is usually 0.89. Even without calculating, just by noticing the inverse d to β correlation, we infer that as the width of the peaks increases, the crystallites get smaller. Although there are limitations to this rule, it is only valid for crystallite below 100 nm [116].

$$d = \frac{K\lambda}{\beta\ cos\theta} \tag{11}$$

The equipment used was an X'PERT-MDP (Philips). The radiation of kα-Cu, power of 45 kV, and current of 40 mA. The analysis was done in a prepared powder sample in the 2θ range of 5° to 70° degrees, at a pace of 0.022°/s. The crystallite size and lattice strain were calculated by the Rietveld method using the software X'Pert Highscore Plus from Malvern Panalytical. As a reference input, a standard powder of $MgAl_2O_4$ was always analyzed with each new set of samples, to ensure the same instrumental conditions.

4.2.4 Helium pycnometry

The Helium Pycnometry is a technique used to determine the real density of a solid by the variation of pressure of He gas in a chamber of known volume. The noble gas He is used due to its chemical inertia and small atomic radius, which eases the fill of pores in the sample.

The pycnometer possesses two chambers interconnected of know volume, the sample chamber, and the expansion chamber. With the valve between chambers closed, the sample chamber is filled to a pre-established pressure. Then, the opening to the expansion chamber causes a pressure drop, which determines the exact volume of the sample, and previously knowing the sample's mass, the real density ρ can be calculated ($\rho = mass/volume$) [111].

Before the analysis, the samples were pre-dried at 105°C for 12 hours. Later, in the sample chamber, the sample went through 200 cycles of purge with He gas to assure the removal of adsorbed impurities and moisture. The Helium pycnometer used was an AccuPyc II 1340 (Micromeritics).

4.2.5 N_2 adsorption for specific surface area

The specific surface area (SSA) of the powder can be measured by the BET (Brunauer, Emmett, and Teller) method, based on the N_2 adsorption isotherms [117]. The amount of N_2 gas adsorbed depends on the available surface area, temperature, and gas pressure, as N_2 already possesses a strong interaction with most solids [118].

Before any measurement, pretreatment is required to remove gases and moisture that could be physically adsorbed on the sample surface. This is carried out by heating up the sample in vacuum. For the test itself, it is necessary to reduce the thermal mobility of N_2 gas, enhancing its adsorption on the sample surface. Thus experiments are performed at cryogenic temperature, usually at 77 K, achieved using liquid N_2. After the cooling of the sample in a cell, known doses of N_2 gas are introduced stepwise in the cell, until a saturation pressure is reached. Ideally, under these conditions, on the sample surface, only a monolayer of N_2 should be adsorbed. Then the cell is removed from the liquid N_2, and as it heats up, it releases the adsorbed N_2, which the equipment quantifies [117, 118]. Previously, knowing the mass of the sample tested, the SSA can be calculated.

The samples were pretreatment for 12 hours at 300°C in a cell of vacuum VacPrep 061 (Micromeritics). The measurements were later performed in a Gemini III 2375 Surface Area Analyzer (Micromeritics).

4.2.6 Transmission electron microscopy

The transmission electron microscopy (TEM) is one of the electron microscopy techniques that uses a beam of electrons onto the sample to form images, measure, create models, and manipulate matter [119]. The greatest advantage of the use of electrons is the resolution that reaches the atomic level. While visible light minimum wavelength (λ) is 400 nm, which results in a naked eye resolution of 0.1 mm, a 100 KeV electron λ ~4 pm (0.004 nm) can reach sizes smaller than the diameter of an atom. Resolution advanced even further in the ‘80s and ‘90s with high-resolution TEM (HRTEM), which could reach 400 KeV and above, unraveling the crystalline lattice and grain boundaries in images [119]. Distinctively, from scanning electron microscopy (SEM), TEM electrons pass through the sample, which has the drawback of not revealing a depth perspective (3 dimensions); however, TEM’s resolution is higher.

The equipment used for imaging was a JEM-2100 (Jeol) TEM operated with a parallel beam at 200 kV. Loose powder images were recorded with a 4kx4k (TVIPS) camera.

4.2.7 Impedance spectroscopy

Impedance Spectroscopy (IS) is the name given to the combined action of a material's resistive and reactance responses when submitted to an alternating current (AC) [120]. Impedance spectroscopy is a technique that measures both contributions the resistive (Z’) and the reactance (Z”) as a range of AC frequency is scanned. The output is plotted on the impedance diagram, as presented in Figure 9, usually forming a semicircle in the complex plane. The vertical axis (imaginary) gives the capacitance magnitude, while the horizontal axis (real) gives from 0 to R the resistance value. Frequency (ω) is shown to increase counterclockwise, but the scanning starts from high frequencies to low ones, clockwise. At the relaxation frequency (ω_0), capacitance (C) is maximized because the electric dipoles achieve resonance. C can be calculated by Equation 12, where f is the AC frequency at ω_0 and X_C is the capacitive reactance [120, 121].

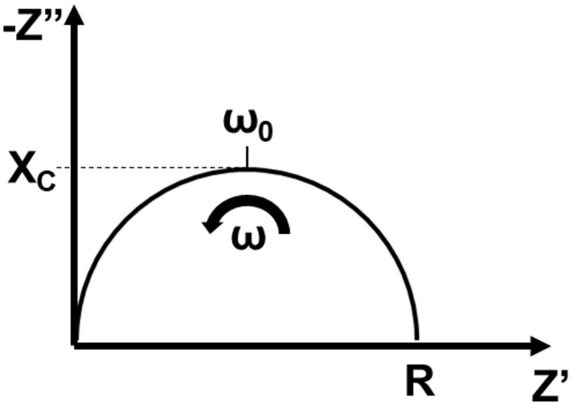

Figure 9. Representation of an impedance diagram. Source: by the author.

$$C = \frac{1}{2\pi f X_C} \tag{12}$$

The interest of impedance spectroscopy for this work is to measure the electrical conductivity and understand the effect of microstructural contributions. A sample's conductivity is directly linked to chemical composition, composition homogeneity, lattice defects (punctual and dislocations), distribution and volume of pores, grain size, grain boundaries, and dopant segregation [13, 14, 58, 122]. Thereby, the impedance diagram allows the distinction of microstructural features, forming more than one semicircle, the first resembling the grain and a second the GB [13]. Though for ZnO, a semiconductor, the grain can show no semicircle, just a displacement in the Z' axis resembling the grain resistance, and the one semicircle corresponds to the GB [122]. Each semicircle can be represented by a resistance-capacitor (RC) in parallel, forming an equivalent circuit, as shown in Figure 10a, or in the ZnO mentioned case, the grain act as resistance (R_G) in series with the GB, which is a RC (R_{GB} and C_{GB}) parallel equivalent circuit, Figure 10b.

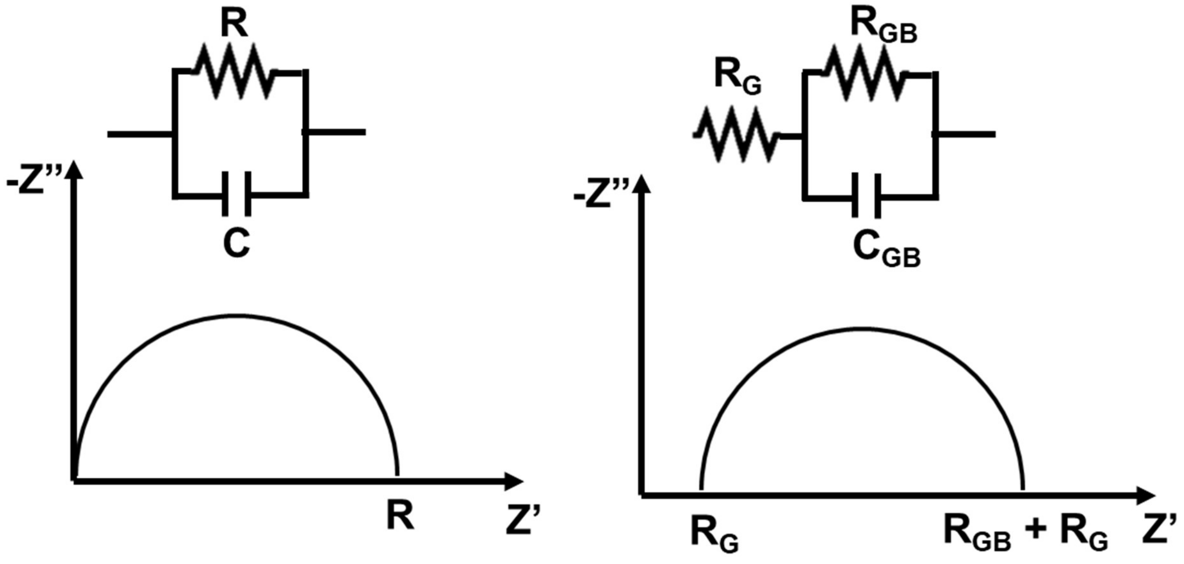

(a) **(b)**

Figure 10. (a) representation of the impedance diagram as a parallel RC equivalent circuit. (b) representation of the ZnO impedance diagram, in the case the grain is only resistive, while the GB is both resistive and capacitive. Source: by the author.

Impedance measurements were performed using an Impedance Meter SI 1260 / Gain-Phase Analyzer (Solartron), with the measuring device built in a closed furnace to control temperature and atmosphere. The second batch of samples was measured with the Impedance Meter and Gain-Phase Analyzer (Novocontrol Alpha-A analyzer). Measurements were obtained in the software's ZPlot and ZView and later treaded with Origin and Excel. The alternated current scanned the frequency range of 3×10^7 Hz to 1 Hz with an amplitude of 500 mV. Samples were first heated up to 200°C with a steady flux of synthetic dry air to ensure the desorption of most of H_2O and CO_2 from the surface. The flux of synthetic dry air was kept constant, and the furnace was cooled down to 200°C, 150°C, and 100°C for the impedance measurements at each of these temperatures. The powder samples were pressed with 125 MPa into 5 mm (3.5 mm for the second batch) thick and 11 mm of diameter cylindrical pellets and submitted to a thermal treatment at 370°C for 1 hour to promote grain boundary area increase with minimal dopant loss.

4.2.8 Infrared spectroscopy

The Fourier transform infrared spectroscopy (FTIR) is a technique that allows the identification of functional groups in the molecule of the sample. The infrared (IR) radiation is absorbed by changes in the dipole moment presented in the vibration of atoms or groups of atoms in a compound. Each different deformation in interatomic bonds absorbs energy at a specific frequency; thus, it is possible to identify the functional groups in a compound by the characteristic absorption bands in the IR spectrum [121, 123].

Further, FTIR techniques were developed, aiming more at how the powder surface and the surface adsorbed molecules interact with IR rather than the bulk. This purpose is achieved with the diffuse reflectance infrared Fourier transform (DRIFT), which with a proper optical setup (concave mirror), collects all the diffusively scattered reflection from the sample focusing on a detector. Hence, the output information allows the identification of surface composition and surface adsorbed compounds [121, 123].

Diffuse reflectance infrared Fourier transform (DRIFT) spectroscopy analyses were carried out to determine adsorbed species using a Thermo-Nicolet Magna 560 with a 4 cm^{-1} resolution and scanning range from 500 to 5000 cm^{-1} (medium IR).

4.2.9 Water adsorption microcalorimetry

Water adsorption microcalorimetry is based on the thermodynamics of water adsorption on a bare surface. Specifically, aiming to measure the heat of adsorption of water molecules on the oxide surface as a function of relative pressures. Due to the strong eagerness of oxide surfaces to adsorb water and atmospheric gases, i.e., CO_2, to achieve a proper oxide surface, the sample must undergo a pretreatment that combines high temperature and vacuum. The water adsorption on an anhydrous surface happens in three subsequent stages: (1) the first molecules adsorb on the surface in a dissociative manner; hence the adsorption enthalpies are the most more exothermic; (2) the next is a transient layer, where adsorbed molecules are still affected by the surface, but not as strong; (3) at a specific coverage, water builds up physisorbed layers, in which the outermost molecules are not affected by the oxide surface. At this point, the water adsorption enthalpy becomes equal to the one of liquid water (−44 kJ/mol), which corresponds to a surface energy of 0.072 J/m^2 [124]. Castro and Gouvea suggest that surface influences very little adsorbed molecules after five monolayers of water [10].

Castro and Quach [124] stated that a water adsorption experiment in a closed system would change the surface energy according to Equation 13. Where φ is the surface coverage, ΔH_{ads} is the measured heat of adsorption, and $\gamma_{anhydrous}$ and $\gamma_{hydrated}$ are the surface energies before and after the given adsorption coverage, respectively. This equation establishes a correspondence between surface energies at any given water coverage, which enables calculating the surface energy when the adsorbed amount and heat of adsorption are known [10].

$$\gamma_{hydrated} = \gamma_{anhydrous} + \varphi\, \Delta H_{ads} \tag{13}$$

The pretreatment and the water adsorption microcalorimetry measurement were carried out in an ASAP 2020 sorption system (water micro-dosimeter) connected to a Calvet-type microcalorimeter (Setaram DSC-111). The pretreatment was carried out by subjecting the sample to 250°C at a vacuum of 10^{-4} mmHg for 12 h. After cooling down, it was set to 25°C, and microdoses of water (1 µmol) were gradually dosed equally in the sample and reference chamber by a bifurcation. It was given enough time for water to be adsorbed and the system to re-establish equilibrium by programming dosing steps at each 4 h down to at least 30 min. The equilibrium is reached when the pressure in the sample and the reference chamber are the same. The ASAP 2020 keeps track of the pressure and water coverage at each new equilibrium, while the DSC-111 monitors the heat of adsorption at each step by reporting the difference between the sample and reference chambers. The dosing continues until a chosen relative pressure is reached [118].

4.2.10 Photocatalytic performance

In a borosilicate glass test tube, 5-mg of the powder samples were suspended in 4 mL of a 5 ppm solution of acetaminophen (APAP) prepared in deionized water. The tube was irradiated by a UV-A LED chip from Dongguan Hongke Lighting Co. with a nominal potency 100 W, the emisson range from 350 to 420 nm and peak emission at 370 nm. The provided irradiance was of 4.2 mW/cm^2 at the outer walls of the test tube, positioned 10 cm from the light source. The content of each tube was magnetically agitated. 100-µL aliquots were collected periodically, diluted, filtered, and stored under refrigerated conditions prior to the analysis. APAP was quantified by UPLC (20-AF, Shimadzu Co.), as described elsewhere [125, 126].

5 RESULTS AND DISCUSSIONS

In order to standardize the label of samples throughout this section, we define labeling parameters by the order in which they appear. In the whole study, it was necessary to make two batches of materials, which are indicated at the beginning of the sample tag, the first batch denoted by #1 and the second by #2. Followed by the added dopant, in this case, the undoped ZnO sample is tagged ZnO-0, and the Cl^--doped samples are ZnOCl-1, ZnOCl-3, ZnOCl-4, ZnOCl-6, and F^--doped samples: ZnOF-1, ZnOF-3, ZnOF-5, ZnOF-7. At the end of these tags, the number resembles the added integer number in mol% of the doping anion, i.e., ZnOCl-3 is the 3 mol% of Cl^- in the ZnO sample. In the second batch, #2, a lixiviation of the samples was investigated, adding 1LX in the end for once lixiviated, i.e., ZnOCl-1 1LX. Because a considerable amount of the dopants was measured at the surface of 1LX samples, a more severe lixiviation methodology was performed only in samples ZnOCl-1 and ZnOCl-6. Sample ZnOCl-4 and its lixiviation forms oddly reached the same composition as ZnOCl-3, and presented outlier properties. Thus its results are discarded to understand the doping phenomena better. This intensive lixiviation consisted of repeating the lixiviation method four additional times, ensuring an excessive lixiviation of Cl^- from the ZnO surfaces. These samples were given the corresponding labels of ZnOCl-1 5LX and ZnOCl-6 5LX.

5.1 Powder characterization

5.1.1 Chemical composition

The first technique used to determine the chemical composition of the powders samples was X-ray fluorescence (XRF), and its results are presented in Table 1. The whole XRF's chemical composition showed ZnO as the major component (≥ 99.40 wt.-%) with minor traces of other oxides (≤ 0.25 wt.-%) such as SiO_2, MgO, Al_2O_3, and SO_3 as impurities from reactants. A significant loss of Cl^- is already noticed in terms of the added quantities, while no F^- was detected. All F^--doped samples showed more Cl^- than the ZnO-0, but considerably less than the least Cl^--doped sample (#1ZnOCl-1), suggesting that NH_4F could have some Cl^- as impurity. The SO_3 content exhibits an apparent increase with both Cl^- and F^--doping; hence it can be an impurity of the doping compounds NH_4Cl and NH_4F. As the aim of XRF was to evaluate trace elements besides the dopants, which showed up to be of no concern, and as both batches used the sample precursors, a XRF analysis was not performed for the second batch (#2).

Table 1. XRF's chemical composition of all ZnO powder samples #1. It is highlighting the main compound ZnO, the halogen doping ions and traces of impurities. For a clear view, some oxides that were evaluated: Fe_2O_3, TiO_2, CaO, K_2O, P_2O_5, NiO, are not presented due to values ≤ 0.02 wt.-%.

Sample	wt.-% of the compound							mol% in ZnO	
	ZnO	Cl^-	F^-	SiO_2	MgO	Al_2O_3	SO_3	Cl^-	F^-
#1ZnO-0	99.60	0.01	0.00	0.20	0.08	0.07	0.02	0.02	0.00
#1ZnOCl-1	99.50	0.17	0.00	0.15	0.08	0.04	0.04	0.39	0.00
#1ZnOCl-3	99.50	0.33	0.00	0.04	0.00	0.05	0.06	0.74	0.00
#1ZnOCl-6	99.40	0.53	0.00	0.04	0.14	0.03	0.17	1.22	0.00
#1ZnOF-1	99.60	0.04	0.00	0.04	0.14	0.02	0.09	0.09	0.00
#1ZnOF-3	99.60	0.03	0.00	0.06	0.13	0.02	0.09	0.07	0.00
#1ZnOF-5	99.40	0.04	0.00	0.25	0.09	0.04	0.15	0.09	0.00
#1ZnOF-7	99.40	0.05	0.00	0.11	0.14	0.03	0.22	0.12	0.00

Despite zero fluoride values in F^--doped samples, the physical evidence further discussed of smaller crystallite size indicated a F^- presence in ZnO. Thus, a more sensitive technique was required, such as ion-selective electrode. Using both a Cl^- selective electrode and a F^- selective electrode, we could determine these species in ZnO more precisely. This first allowed us to check the values with the XRF results, shown in Figure 11, exhibiting a good agreement between the techniques, guaranteeing the reliability of the selective electrode's preparation of solutions. Therefore, for this work, we established the selective electrodes results as the trusted composition for both halogens ions and batches, presented in Table 2.

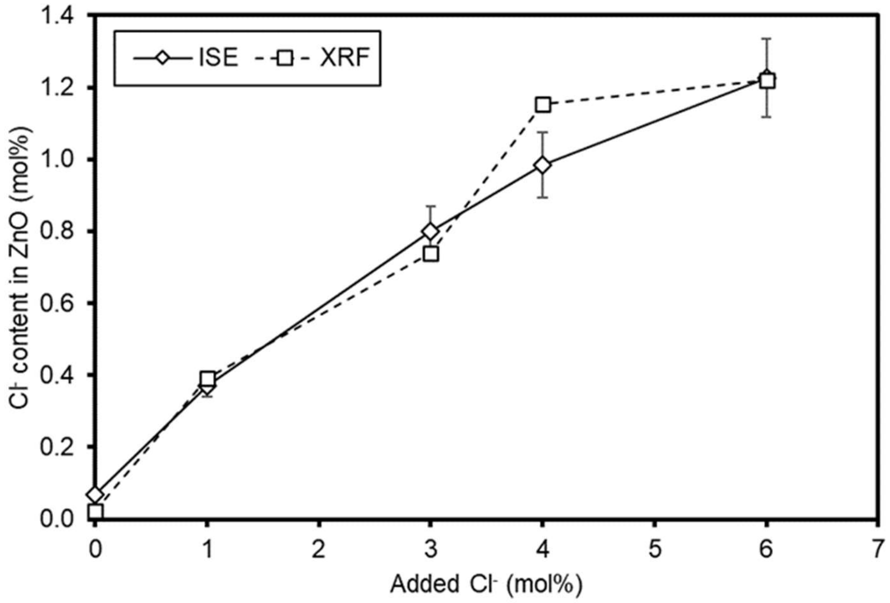

Figure 11. Cl⁻ content measurement by two different techniques Cl⁻ selective electrode (ISE) and X-ray fluorescence (XRF) for the purpose comparison. Batch #1.

Table 2. ISE's chemical composition of all ZnO powder samples #1 and #2. Exceptionally, due to F⁻ relative lower content, three decimal places are shown to ensure at least two significant figures.

Sample	#1 mol% in ZnO		#2 mol% in ZnO	
	Cl⁻	F⁻	Cl⁻	F⁻
ZnO-0	0.07 ± 0.01	0.015 ± 0.001	0.07 ± 0.01	0.012 ± 0.001
ZnOCl-1	0.37 ± 0.03		0.43 ± 0.04	
ZnOCl-3	0.80 ± 0.07		1.03 ± 0.09	
ZnOCl-4	0.98 ± 0.09			
ZnOCl-6	1.23 ± 0.11		1.25 ± 0.11	
ZnOF-1		0.038 ± 0.003		0.011 ± 0.001
ZnOF-3		0.043 ± 0.004		0.013 ± 0.001
ZnOF-5		0.054 ± 0.005		0.034 ± 0.003
ZnOF-7		0.032 ± 0.003		0.033 ± 0.003

The amount of Cl⁻ and F⁻ retained in the samples was much lower than the target composition referenced by the name of the sample, as Table 2 shows a significant dopant loss. In every case, more than 60% of these anions were lost. Interestingly, even the undoped samples showed traces of 0.07 mol% Cl⁻ and ~0.013 mol% F⁻, probably as contamination from reactants. There is no proportional correlation between the added quantity regarding the retained amount of dopants. But instead, a systematical decrease, on average Cl^--doped batches, in the dopant retainment with 40, 31, 26, and 21% for ZnOCl-1, ZnOCl-3, ZnOCl-4, and ZnOCl-6, respectively. The compositions were very similar between Cl^--doped batches, with the standard deviation overlapping equivalent dopant contents, except for ZnOCl-3, which slightly diverged.

The mentioned systematical decrease, in dopant retainment, was also noticed for the #1 F^--doped with 3.8, 1.4, 1.1, and 0.5% for ZnOF-1, ZnOF-3, ZnOF-5, and ZnOF-7, respectively. While #2 presented a greater F^- loss, only ZnOF-1 barely retained more than 1% of the initially added dopant. For #2, the greater the amount added, the greater the amount retained. Overall, F^- smaller retention in ZnO can justify these composition variations between the two batches. The halogens ions lost are probably happening during the pyrolysis of the Zn resin. However, it is hard to affirm if this loss happens in the calcination's heating ramp while it is still a Zn resin or if it happens after the ZnO powder is achieved via diffusion to the surface and evaporation. Perhaps, both play a significant role in the loss of dopants, as added dopants did affect crystallite size.

Lixiviated samples from #2 had their dopant content also evaluated; the results are shown in Table 3, and as expected, lixiviation caused a significant dopant reduction. For Cl^--doped once lixiviated samples (1LX), the smallest reduction was 15% for the undoped sample, increased ~45% for the ZnOCl-1, and reached a stable value of ~60% for the three higher dosages. The five-times lixiviated samples (5LX) reached ~85% reduction of Cl^-, with the total Cl^- content nearing that of the undoped sample. The F^- content not only exhibited reductions as observed in the two higher dosages but also increased. This is due to its small content in the samples, thus resulting in overlapping standard deviations.

Table 3. ISE's chemical composition of lixiviated ZnO powder samples #2. Exceptionally, due to F^- relative lower content, three decimal places are shown to ensure at least two significant figures.

Sample	#2 mol% in ZnO	
	Cl^-	F^-
ZnO-0 1LX	0.06 ± 0.01	0.018 ± 0.002
ZnOCl-1 1LX	0.23 ± 0.02	_
ZnOCl-3 1LX	0.41 ± 0.04	_
ZnOCl-6 1LX	0.47 ± 0.04	_
ZnOCl-1 1LX	0.07 ± 0.01	
ZnOCl-6 1LX	0.26 ± 0.03	
ZnOF-1 1LX		0.018 ± 0.002
ZnOF-3 1LX		0.019 ± 0.002
ZnOF-5 1LX		0.021 ± 0.002
ZnOF-7 1LX	_	0.027 ± 0.003

5.1.2 Crystallite structure and size

Figures 12 and 13 show the XRD patterns of #1 Cl^--doped and F^--doped ZnO samples, respectively, in both the ZnO wurtzite (JCPDS card no. 36-1451) was the only identified phase, indicating single-phase samples and confirming the purity of the samples. Visually comparing the samples ZnOCl-3, ZnOCl-4, ZnOF-3, ZnOF-5, and ZnOF-7 exhibit slightly broader peaks than the other diffractograms. According to the Scherrer equation (Equation 11), broader peaks are associated with smaller crystallite sizes.

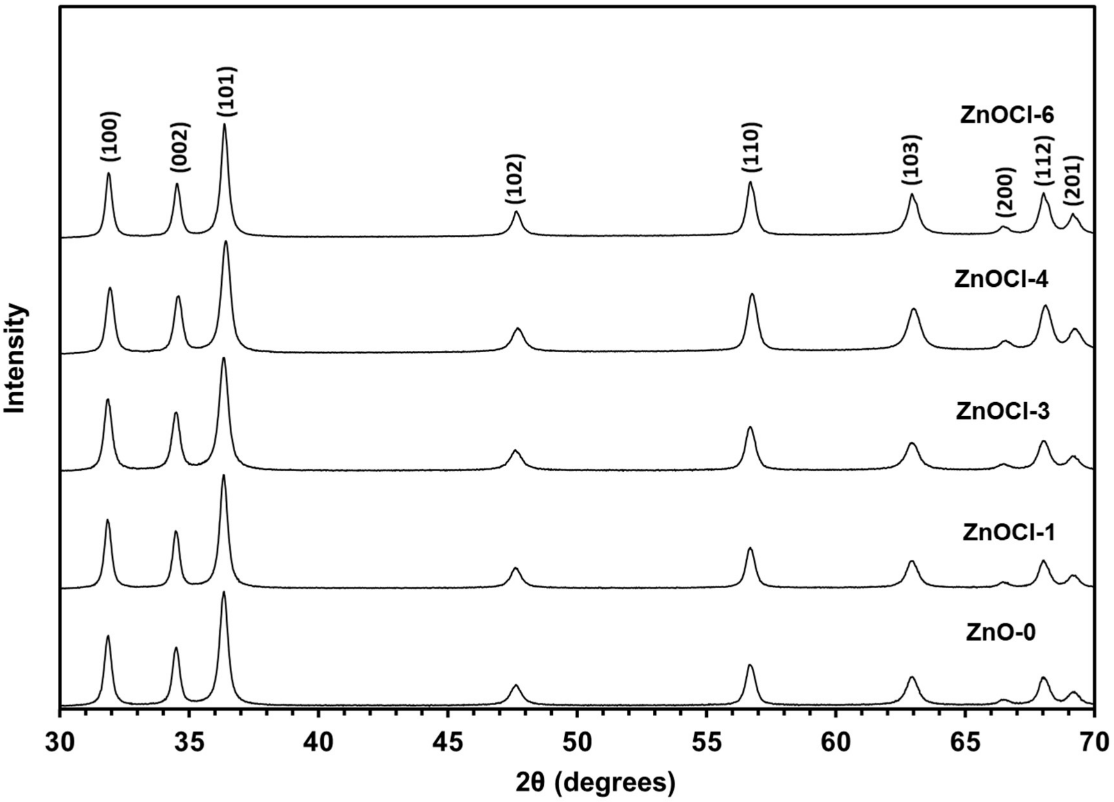

Figure 12. X-ray diffraction patterns of ZnO and Cl⁻-doped ZnO powder samples #1.

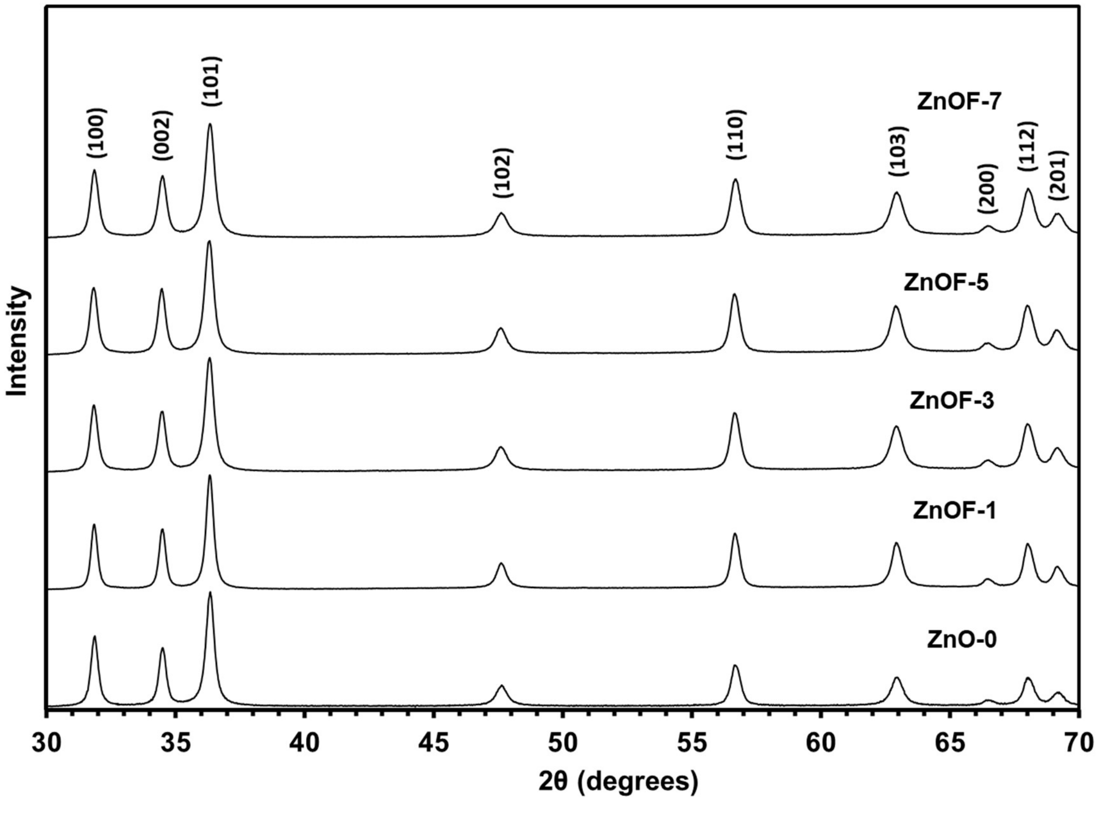

Figure 13. X-ray diffraction patterns of ZnO and F⁻-doped ZnO powder samples #1.

The average crystallite sizes, lattice parameters, and micro strain of the wurtzite crystallites were obtained from a Rietveld analysis on XRD data (Table 4). The crystallite sizes exhibit no clear dependence with Cl^--doping. Such behavior is different from the previous observations of crystallite size dependence on cation dopants [10, 27, 77-87]. A small decrease in the crystallite size around 3 nm (10%) was observed for ZnOCl-3 and ZnOCl-4 samples related to the undoped (ZnO-0). The F^--doped samples showed a more evident trend of reducing crystallite size with F^--doping, similar to cations doping, even with the smallest dosage (ZnOF-1) presenting an increase in crystallite size. Also, the crystallite reduction effect of F^--doping is greater than Cl^--doping, and as recalled in Table 2, in smaller dopant quantities, as the smaller crystallite (ZnOF-7 with 23.3 nm) achieved a reduction of 4.2 nm (15%) related to ZnO-0.

Regarding the lattice parameters, we observe that Cl^--doping caused an increase in all lattice parameters. F^--doping did cause an increase, but less, and not proportionally to the added F^-; on the contrary, it affected more c reaching similar values to the corresponding Cl^- additions. Thus, both dopants caused an expansion of the unit cell, which may be an indication of solid solution formation or surface energy reduction. The maximum increase in unit cell volume was 0.12% for the ZnOCl-6, while only 0.05% for the ZnOF-7. Such minor changes indicate a small solubility of Cl^- and F^- in the bulk of ZnO grains, suggesting that most of the dopants are located at interfaces. Even at these sites, dopants can affect the bond length. In stoichiometric ZnO, the Zn-O distance is 1.95 Å, whereas Zn-Cl (in Cl^--doped ZnO) is a longer bond of approximately 2.33 Å, mainly due to the 29% larger ionic radius of Cl^- (1.81 Å) compared with that of O^{2-} (1.40 Å), which it replaces the lattice [101, 127]. Another supporting argument is the reduced electronegativity of the substitution since Cl has an electronegativity of 3.0 and O of 3.5. On the other hand, F has a higher electronegativity than O, with 4.0 and a shorter Zn-F bond length of 1.77 Å [128].

Table 4. Crystallite sizes, lattice parameters, and Micro Strain of the lattice of ZnO (wurtzite), and Cl^- and F^--doped nanopowders.

Sample	Crystallite Size (nm)	a (Å)	c (Å)	Primitive Unit Cell Volume (Å^3)	Micro Strain (%)
ZnO-0	27.5 ± 0.5	3.2504 ± 0.0002	5.2098 ± 0.0003	47.6678 ± 0.0057	0.347 ± 0.001
ZnOCl-1	29.1 ± 0.2	3.2505 ± 0.0002	5.2098 ± 0.0003	47.6708 ± 0.0057	0.329 ± 0.001
ZnOCl-3	24.7 ± 0.3	3.2505 ± 0.0002	5.2106 ± 0.0004	47.6781 ± 0.0066	0.390 ± 0.002
ZnOCl-4	24.7 ± 0.4	3.2513 ± 0.0005	5.2116 ± 0.0005	47.7107 ± 0.0119	0.391 ± 0.005
ZnOCl-6	28.7 ± 0.5	3.2519 ± 0.0004	5.2114 ± 0.0005	47.7265 ± 0.0104	0.330 ± 0.002
ZnOF-1	30.6 ± 0.7	3.2508 ± 0.0004	5.2098 ± 0.0006	47.6796 ± 0.0114	0.306 ± 0.003
ZnOF-3	25.0 ± 0.8	3.2507 ± 0.0004	5.2107 ± 0.0007	47.6849 ± 0.0123	0.384 ± 0.007
ZnOF-5	24.8 ± 0.6	3.2506 ± 0.0004	5.2101 ± 0.0007	47.6764 ± 0.0123	0.381 ± 0.006
ZnOF-7	23.3 ± 0.3	3.2508 ± 0.0004	5.2111 ± 0.0007	47.6915 ± 0.0123	0.412 ± 0.009

Table 4 shows that lattice parameters increased mainly along the c-axis, and total micro strain increased as expected for Cl^--doping [98]; this was also observed F^--doping. The lattice's micro strain does not correspond directly with the volume of unit cell variation but shows a relatively close match with crystallite size. As presented in Figure 14, with a linear behavior of correspondence, smaller crystallites (ZnOF-7, ZnOF-5, ZnOCl-3, ZnOCl-4) present higher strain than larger crystallites (ZnOF-1, ZnOCl-1, ZnOCl-6). Since both linear trends are overlaid, the micro strain does not seem to be influenced by the dopant but rather how these are affecting interfaces and crystallite size stabilization. This behavior can be explained according to the Young-Laplace equation (Equation 13). At a similar surface energy (γ) level, as crystallite radius (r) increases, the relative pressure (P) over the crystallite decreases, causing a reduction in the lattice micro strain [129, 130].

$$P = \frac{2\,\gamma}{r} \tag{13}$$

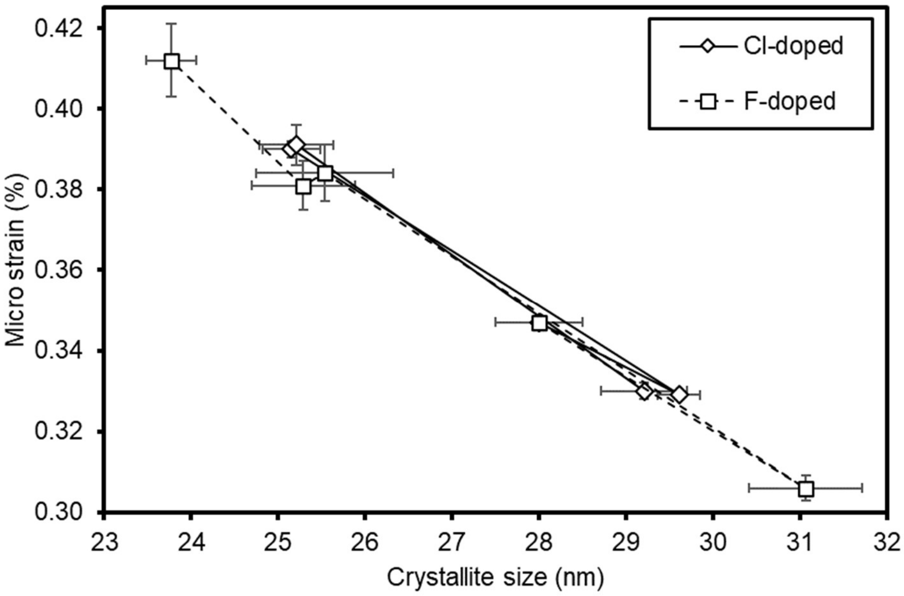

Figure 14. Micro strain of the lattice versus crystallite size for #1 both Cl⁻ and F⁻-doped samples, also the undoped sample.

The second batch exhibited very similar XRD diffractograms as the first one, which for #2 Cl⁻-doped and F⁻-doped ZnO samples are shown in Figures 15 and 16, respectively. The broad peaks observed among all samples indicate the nanosized nature of the crystallites. Wurtzite (JCPDS card no. 36-1451) was the only phase identified, implying single-phase samples.

All lixiviated samples, as well as the pristine powders, exhibit no second phase such as hydrates, at least not in sufficient amounts to be detected by XRD. No drastic changes were seen in the intensity of the peaks, suggesting that a substantial solubilization of the ZnO nanoparticles or changes in the crystallite forms due to the lixiviation method can be safely neglected.

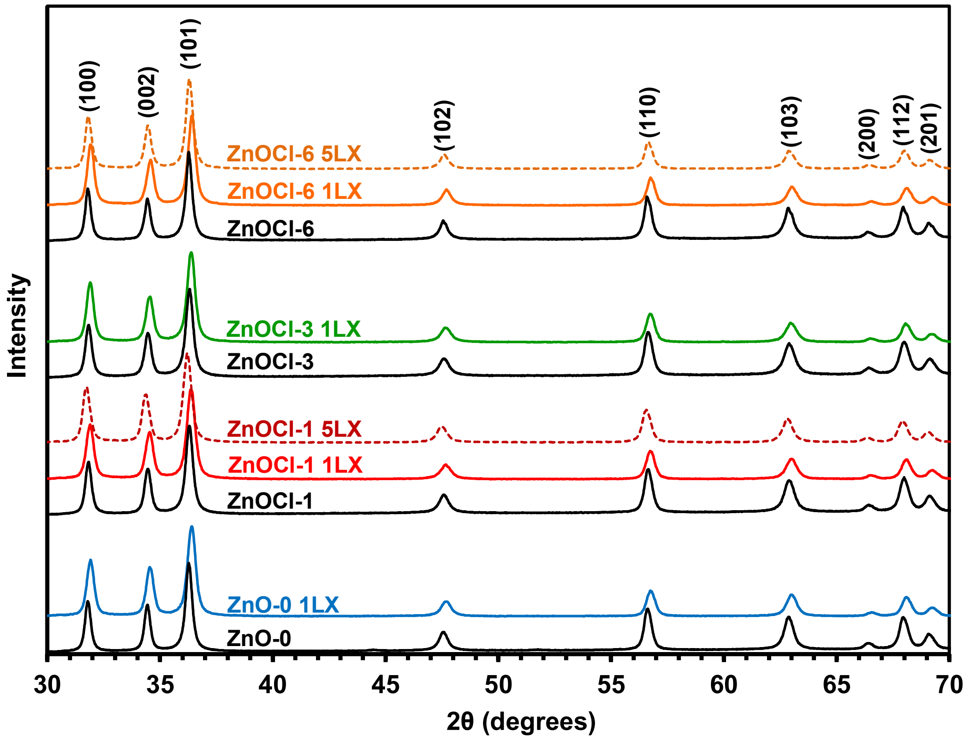

Figure 15. XRD diffractograms of #2 ZnO and Cl⁻-doped ZnO samples: pristine, 1LX and 5LX.

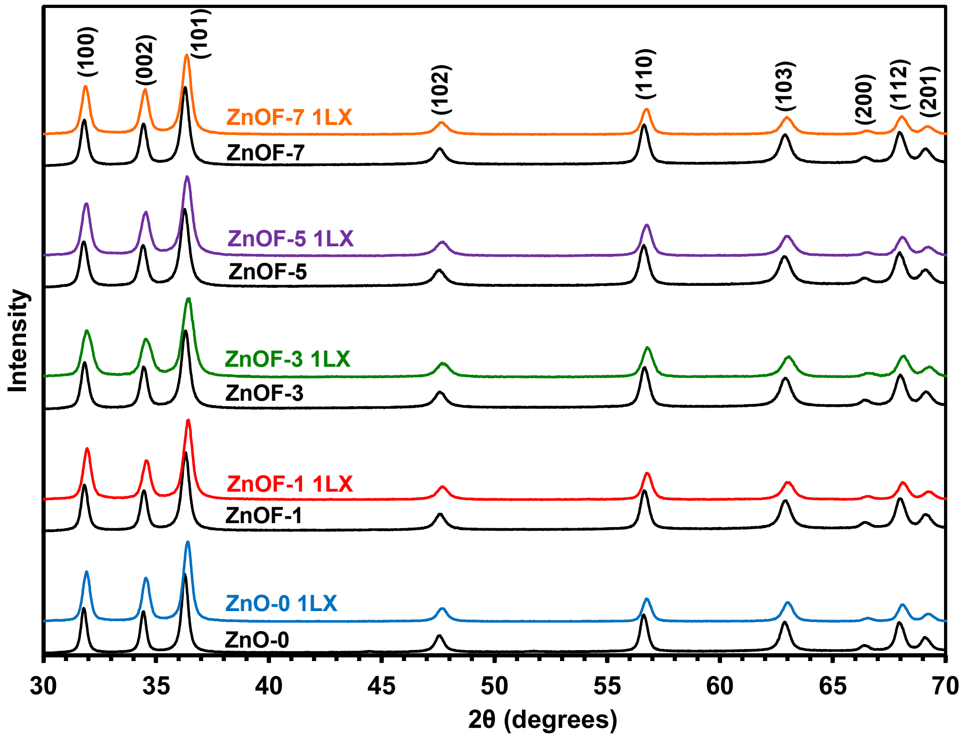

Figure 16. XRD diffractograms of #2 ZnO and F⁻-doped ZnO samples: pristine and 1LX.

The average crystallite size (Rietveld Method) of the #2 Cl⁻-doped and F⁻-doped ZnO nanopowders are listed in Table 5. All synthesized samples were nanosized and smaller than 30 nm. Crystallite sizes revealed no clear dependence on Cl⁻ and F⁻ doping, a behavior that differs from previous findings of crystallite size dependence on cation dopants in nano-oxides [10, 27, 77-87, 131]. While the crystallite sizes show no clear trend, the variations observed might be associated with processing parameters that change the surface energy during evaporation, such as the Cl⁻ and F⁻ loss mechanism, its bulk solubility, and the interface segregation during the synthesis of the nanopowders. Indeed, a prior study of Cl⁻ doping in ZnO points out a similar crystallite size dependence with Cl⁻ loss [48].

ZnO is slightly soluble in water (0.2−0.5 mg/L) at pH 7.0 [132]. However, as observed in Table 5, the 5LX sample's crystallite size did not continue to decrease with lixiviation when compared to that of 1LX samples. On average, the crystallite size reduction was ~4 nm (14%) upon lixiviation of the samples.

Table 5. Crystallite sizes of the #2 Cl⁻-doped and F⁻-doped ZnO nanopowders; pristine, 1LX and 5LX.

Sample	Crystallite size (nm)	Sample	Crystallite size (nm)	Sample	Crystallite size (nm)
ZnO-0	29.7 ± 0.6	ZnO-0 1LX	24.1 ± 0.2	ZnOCl-1 5LX	23.8 ± 0.2
ZnOCl-1	27.2 ± 0.5	ZnOCl-1 1LX	23.2 ± 0.2		
ZnOCl-3	25.8 ± 0.4	ZnOCl-3 1LX	24.4 ± 0.3		
ZnOCl-6	29.8 ± 0.6	ZnOCl-6 1LX	25.6 ± 0.3	ZnOCl-6 5LX	27.5 ± 0.4
ZnOF-1	25.4 ± 0.4	ZnOF-1 1LX	22.1 ± 0.2		
ZnOF-3	23.4 ± 0.4	ZnOF-3 1LX	17.5 ± 0.2		
ZnOF-5	22.4 ± 0.3	ZnOF-5 1LX	19.7 ± 0.2		
ZnOF-7	24.8 ± 0.4	ZnOF-7 1LX	21.8 ± 0.2		

5.1.3 Interface areas

The pycnometry density and the interface areas measured and calculated in all samples, #1 and #2, are presented in Table 6. Specific Surface Area (SSA) measured by N_2 gas adsorption (S_{BET}), shows for #1 Cl⁻-doped a decrease for the smaller dosage (ZnOCl-1), then significantly increases to a maximum of 18.0 m^2/g for ZnOCl-3 and gradually diminishes back until ZnOCl-6 reaches the same value as the undoped ZnO-0. For #1 F^--doped, the lowest dosage (ZnOF-1) also decreases but then continuously increases, with ZnOF-7 reaching a maximum of 18.1 m^2/g. For #2, Cl^--doped and F^--doped showed no clear trend with doping, intermediary dosages reaching the highest SSA. The SSA of 1LX and 5LX samples showed mostly slight increases but, in some cases, minor decreases, over their pristine version. No significant trend deserves an in-depth analysis.

Knowing the crystallite size (d), given in Table 4 and 5, and the pycnometry density (ρ), it is possible to calculate the specific total interface area of crystallites (S_T) (assumed as grains) according to Equation 14. The 7.11 value is a geometric shape factor for truncated octahedron [133], the assumed shape for these particles. The difference of S_T and S_{BET} are of a solid-solid interface, which is mutually shared by at least two grains. Thus Equation 15 shows how to calculate the grain boundary (GB) area (S_{GB}). For lixiviated samples, the pycnometry density was only measured for the two 5LX samples. It was expecting that lixiviation would reduce the density as it removes Cl^- from the surface. Indeed both 5LX presented a ~0.08 g/cm^3 density decrease.

$$S_T = \frac{7.11}{d\,\rho} \tag{14}$$

$$S_{GB} = \frac{(S_T - S_{BET})}{2} \tag{15}$$

Table 6. Density and specific interface areas: surface, total, grain boundary, and the ratio of grain boundary area by surface area.

Sample	Pycnometry Density (g/cm^3)	S_{BET} (m^2/g)	S_T (m^2/g) calculated	S_{GB} (m^2/g) calculated	S_{GB}/S_{BET}
#1ZnO-0	5.632 ± 0.003	15.3 ± 0.1	46.5 ± 0.9	15.6 ± 1.0	1.02 ± 0.08
#1ZnOCl-1	5.645 ± 0.005	14.0 ± 0.1	43.7 ± 0.4	14.8 ± 0.5	1.06 ± 0.04
#1ZnOCl-3	5.526 ± 0.004	18.0 ± 0.1	52.7 ± 0.7	17.4 ± 0.8	0.96 ± 0.06
#1ZnOCl-4	5.423 ± 0.009	17.0 ± 0.1	53.0 ± 1.0	18.0 ± 1.1	1.06 ± 0.09
#1ZnOCl-6	5.281 ± 0.009	15.3 ± 0.1	46.8 ± 0.9	15.8 ± 1.0	1.03 ± 0.08
#1ZnOF-1	5.655 ± 0.004	12.0 ± 0.1	41.5 ± 0.9	14.8 ± 1.0	1.23 ± 0.11
#1ZnOF-3	5.582 ± 0.003	15.8 ± 0.1	51.2 ± 1.6	17.7 ± 1.7	1.12 ± 0.15
#1ZnOF-5	5.611 ± 0.004	16.4 ± 0.1	50.9 ± 1.3	17.2 ± 1.4	1.05 ± 0.11
#1ZnOF-7	5.552 ± 0.003	18.1 ± 0.1	55.6 ± 0.7	18.7 ± 0.8	1.04 ± 0.06
#2ZnO-0	5.446 ± 0.006	13.6 ± 0.1	43.9 ± 0.9	15.1 ± 1.0	1.11 ± 0.08
#2ZnOCl-1	5.468 ± 0.006	14.4 ± 0.1	47.8 ± 0.8	16.7 ± 0.9	1.15 ± 0.07
#2ZnOCl-3	5.438 ± 0.004	16.9 ± 0.1	50.6 ± 0.9	16.8 ± 1.0	0.99 ± 0.06
#2ZnOCl-6	5.406 ± 0.009	16.7 ± 0.1	44.2 ± 0.9	13.7 ± 1.0	0.82 ± 0.06
#2ZnOF-1	5.474 ± 0.006	14.6 ± 0.1	51.1 ± 0.9	18.2 ± 1.0	1.25 ± 0.08
#2ZnOF-3	5.417 ± 0.006	18.1 ± 0.1	56.1 ± 1.0	19.0 ± 1.1	1.05 ± 0.06
#2ZnOF-5	5.439 ± 0.011	16.8 ± 0.1	58.4 ± 1.0	20.8 ± 1.1	1.24 ± 0.07
#2ZnOF-7	5.421 ± 0.008	16.0 ± 0.1	52.8 ± 0.9	18.4 ± 1.0	1.15 ± 0.07
#2ZnO-0 1LX		13.2 ± 0.1			
#2ZnOCl-1 1LX		15.3 ± 0.1			
#2ZnOCl-3 1LX		15.7 ± 0.1			
#2ZnOCl-6 1LX		17.1 ± 0.1			
#2ZnOF-1 1LX		14.3 ± 0.1			
#2ZnOF-3 1LX		17.5 ± 0.1			
#2ZnOF-5 1LX		16.3 ± 0.1			
#2ZnOF-7 1LX		17.3 ± 0.1			
#2ZnOCl-1 5LX	5.387 ± 0.009	14.5 ± 0.1	55.4 ± 0.7	20.5 ± 0.8	1.41 ± 0.06
#2ZnOCl-6 5LX	5.332 ± 0.010	16.8 ± 0.1	48.4 ± 0.7	15.8 ± 0.8	0.94 ± 0.06

The S_T and S_{GB} present a similar behavior as S_{BET} with the Cl^- or F^- dosage, within the deviation of measurements. Thus, the ratio S_{GB}/S_{BET} is maintained at approximately a 1:1 equilibrium between these interface areas (surface and GB). Except for #2 Cl^--doped, where there is a clear correlation between the amount of the dopant and the evolution of the S_{GB}/S_{BET} ratio. The increase of this ratio with the addition of Cl^- suggests an improved stabilization of the surface (solid-gas interface), with respect to the GB (solid-solid interface), with a possible preference of Cl^- segregation to the particle surface. The pycnometry density of #1 is shown in Figure 17, with a relevant decrease with Cl^--doping, and more minor variations with F^--doping. Especially in Cl^--doped ZnOCl-6, the total reduction of density reached 6.2% when compared to ZnO-0. The significant density decreased with Cl^--doped samples might be associated with the creation of punctual defects such as zinc vacancies (V_{Zn}'') [134], which could be induced by Cl^- replacing O^{2-} to maintain electroneutrality. F^- did not affect such a decrease of density, as ZnOF-7 had a 1.4% reduction. For the #2, the same #1 F^--doping variations, with smaller decreases in density, were noticed in Cl^- and F^--doping.

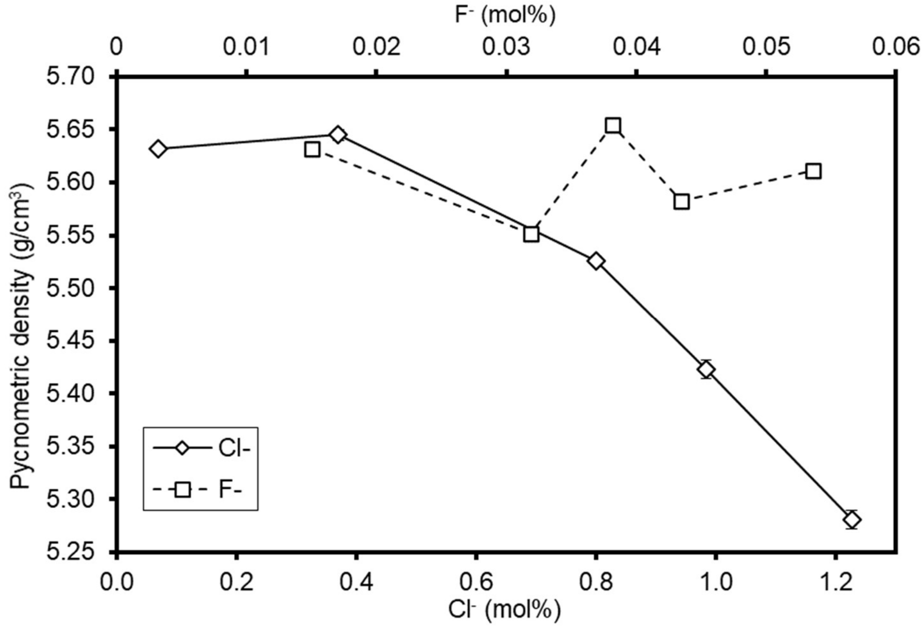

Figure 17. Pycnometry density versus dopant content, for #1 Cl^- and F^--doped samples.

Due to the drop of density for Cl^--doped, and based on the continuous rise of unit cell volume (V) seen in Table 6, we can evaluate a mass (m) balance (V × ρ = m) for ZnO-0 and ZnOCl-6. Taking as reference unitary values for the ZnO-0, where 1V × 1ρ = 1m, while for the ZnOCl-6 1.0012V × 0.938ρ = 0.939m, hence a 6.1% mass reduction. This decrease is not related to interface areas as the two samples have similar interface areas but are a strong indication of the creation of punctual defects such as zinc vacancies ($V_{Zn}^{''}$) reported related to Cl⁻-doped ZnO powders [134].

The grain size, crystallinity, and morphology were analyzed by TEM (Figure 18). Sample #1 ZnOCl-3 was chosen for TEM observation due to its higher SSA and smaller crystallite size. The images revealed grains with irregular shapes, mostly rounded edges, and some hexagonal geometry, which overlaid each other forming agglomerates. The grains visually resemble the ~25 nm average size of the XRD data (Table 4). Figure 18b shows larger crystallites (~40-50 nm), emphasizing the grain boundary shared by two grains. Previous reports showed that Cl⁻-doping might shift the morphology of crystallites from a long hexagonal needle or equiaxial particles to hexagonal disks [100]. However, the TEM images showed that Cl⁻-doping, in the studied range, had no appreciable effect on the particle shape in the present study. Probably, the synthesis method used in this work was the main reason why the particle morphology did not change.

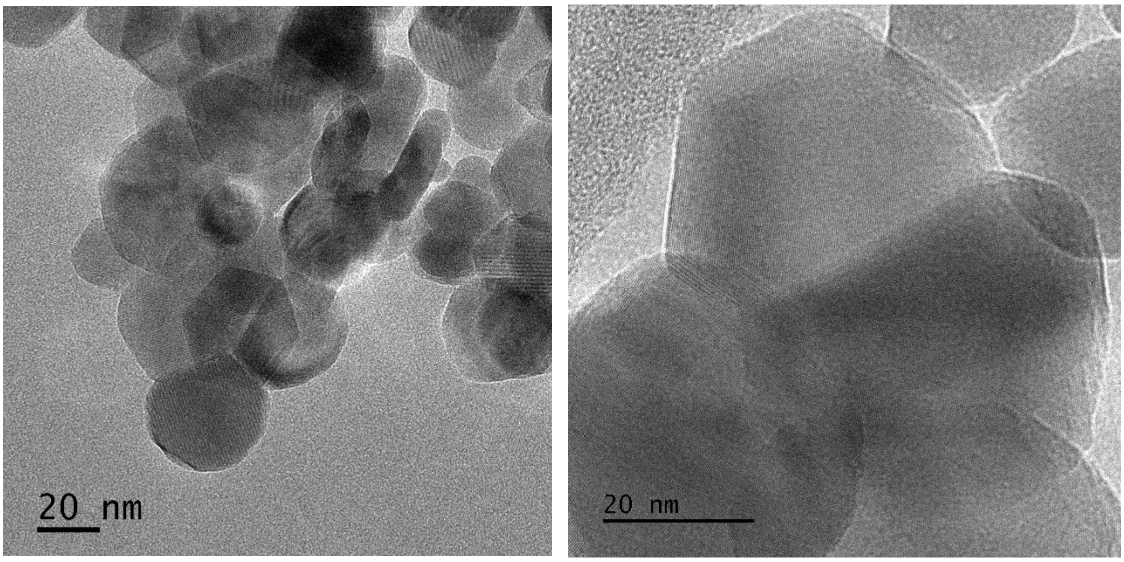

(a) (b)

Figure 18. TEM image of #1 ZnOCl-3 samples (a) Equiaxial and hexagonal grains, and (b) showing a grain boundary shared by 2 grains.

5.1.4 Dopant segregation

The interface excess (Γ) was calculated by measuring the dopant concentration in two solutions with the selective electrode. In one, the total amount of dopant in each sample, by sample dissolution, and in the other, the amount of dopant lixiviated from the ZnO surface. This latter solution gives the amount of dopant at the surface and using

Equation 16. We can calculate the dopant surface excess ($\mathit{\Gamma}_{Dop.}{}^{S}$). Where $n_{Dop.}{}^{S}$ is the number of moles of the dopant in the lixiviated solution per gram of powder.

$$\mathit{\Gamma}_{Dop.}{}^{S} = \frac{n_{Dop.}{}^{S}}{S_{BET}} \tag{16}$$

The GB excess $\mathit{\Gamma}_{Dop.}{}^{GB}$ is calculated with the remaining concentrations, according to Equation 17. Where $n_{Dop.}{}^{T}$ is the total dopant concentration from the dissolved solution, $n_{Dop.}{}^{S}$ the washed-out surface concentration (lixiviated solution), and $n_{Dop.}{}^{bulk}$ the amount in the bulk. These concentrations allow the calculation of the amount imprisoned in the grain boundary, $n_{Dop.}{}^{GB}$ (= $n_{Dop.}{}^{T} - n_{Dop.}{}^{S} - n_{Dop.}{}^{bulk}$). All concentrations are given in number of moles of dopant per gram of powder.

$$\mathit{\Gamma}_{Dop.}{}^{GB} = \frac{n_{Dop.}{}^{T} - n_{Dop.}{}^{S} - n_{Dop.}{}^{bulk}}{S_{GB}} \tag{17}$$

While the $n_{Dop.}{}^{T}$ and the $n_{Dop.}{}^{S}$ can be directly measured by chemical analysis, the $n_{Dop.}{}^{bulk}$ needs to be estimated. We have determined the dopant bulk solubility based on the thermodynamic evidence, according to the following considerations.

As observed in Table 6, the S_{GB}/S_{BET} ratio does not change with Cl^{-}-doping, within samples of the #1. According to Equation 6 [75], the interface area variation (dA_i) is connected to the interface energy (γ_i) with the product of the two is given by the Gibbs free energy variation (dG), which governs the nanostability of a system at constant composition (n), pressure (P), and temperature (T).

$$dG = \sum (\gamma_i dA_i)_{T,P,n} \tag{6}$$

The main driving energy for grain growth on nano-oxides is recognized to be related to the decrease in Gibbs free energy, which is also connected to the reduction in the specific interface area at a given temperature [10]. In our system, the unchanged S_{GB}/S_{BET} ratio throughout the samples suggests that the interface energy ratio (γ^{GB}/γ^{S}) is also constant. Thus, based on Equation 9 (reminded), relating interfacial energies (surface and GBs) to excesses, one may write Equation 18.

$$\gamma = \gamma_0 + \Gamma \, . \Delta H_{seg} \tag{9}$$

$$\frac{(\gamma^{GB} - \gamma_0{}^{GB})}{(\gamma^{S} - \gamma_0{}^{S})} = \frac{\Gamma^{GB} \, . \Delta H_{seg}{}^{GB}}{\Gamma^{S} \, . \Delta H_{seg}{}^{S}} \tag{18}$$

Where γ^{GB} and $\gamma_0{}^{GB}$ are the GB energies with and without solute segregation, Γ^{GB} is the GB excess, and $\Delta H_{seg}{}^{GB}$ is the enthalpy of GB segregation. The denominator represents the same parameters for the interface solid-vapor (surface). This equation suggests that the enthalpy of segregation ratio ($\Delta H_{seg}{}^{GB}/\Delta H_{seg}{}^{S}$) is constant at a given temperature, which leads to a direct proportionality between γ^{GB}/γ^{S}, Γ^{GB}/Γ^{S}, and S_{GB}/S_{BET}. All Γ are presented in Table 7, and the ratio of $\Gamma_{Dop.}{}^{GB}/\Gamma_{Dop.}{}^{S}$ to evaluate the dopant interfaces preferences and tendencies with doping. Also, the total dopant content is recalled for reference.

Considering this thermodynamic evidence, for the Cl^--doped ZnO, we have found that $\Gamma_{Cl}{}^{GB}/\Gamma_{Cl}{}^{S}$ ratio becomes stable ~0.4 for higher Cl^- dosages (Figure 19). Without considering any bulk solubility, the ZnO-0 would have a $\Gamma_{Cl}{}^{GB}/\Gamma_{Cl}{}^{S}$ value of 0.82, which is twice higher than the ratio for the higher Cl^- dosages. Thus, to bring $\Gamma_{Cl}{}^{GB}/\Gamma_{Cl}{}^{S}$ values to the level of around 0.40 within the respective deviations, we determined a value of 1.97 µmol/g (or 0.12 µmol/m^2) to be discounted from the $\Gamma_{Cl}{}^{GB}$ of all samples. Even the eccentricity $\Gamma_{Cl}{}^{GB}/\Gamma_{Cl}{}^{S}$ of 0.15 that occurred with ZnOCl-1, where the $\Gamma_{Cl}{}^{S}$ increased more than $\Gamma_{Cl}{}^{GB}$, and perhaps faster, which caused an unbalance of interface energies that lead to a significant crystallite growth in relation to the undoped. From this optimal ratio of 0.4, we estimated the Cl^- bulk solubility ($n_{Cl}{}^{bulk}$) as 0.016 mol%. Thus, this value was used to calculate the $\Gamma_{Cl}{}^{GB}$ (Equation 17). For #2 Cl^--doping, utilizing the same principle of analysis [48], graphically presented in Figure 20, even though the SSA/SGB drops in the two highest dosages, it is initially maintained at ~1.0. Therefore, we could subtract 5.4 µmol/g of Cl^- from each sample's specific $\Gamma_{Cl}{}^{GB}$ to bring all $\Gamma_{Cl}{}^{GB}/\Gamma_{Cl}{}^{S}$ to ~0.20 as shown in Figure 20. The bulk solubility was thus estimated as 0.044% Cl^-. The bulk solubility estimations of #1 and #2 did not converge, which can be due to the different $\Gamma_{Cl}{}^{GB}/\Gamma_{Cl}{}^{S}$ optimum values, which lead to different specific subtractions of dopant mainly to adjust the undoped sample; and partially due the small solubility values.

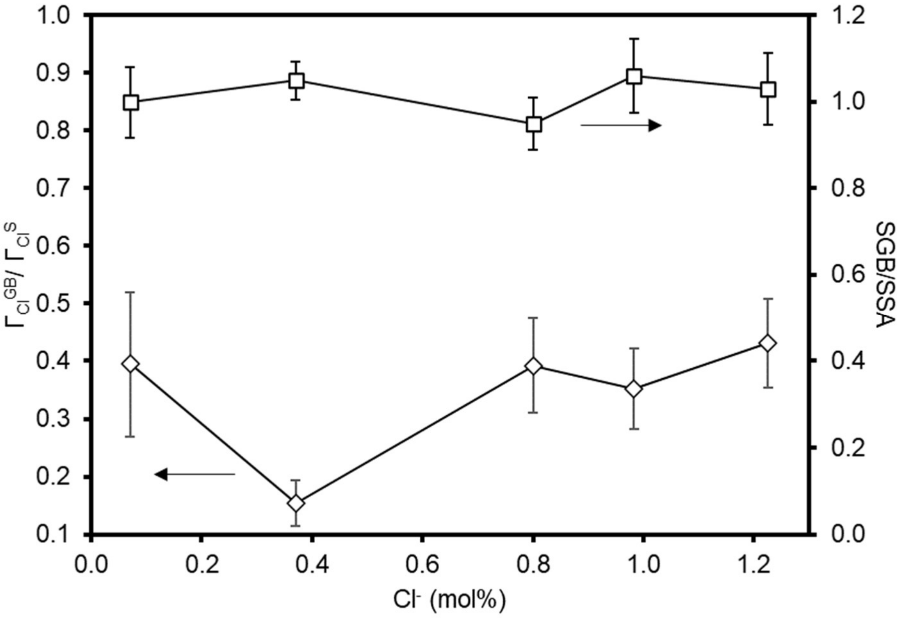

Figure 19. The optimal calculated $\Gamma_{Cl}^{GB}/\Gamma_{Cl}^{S}$ ratio and S_{GB}/S_{BET} ratio versus the total amount of #1 Cl⁻.

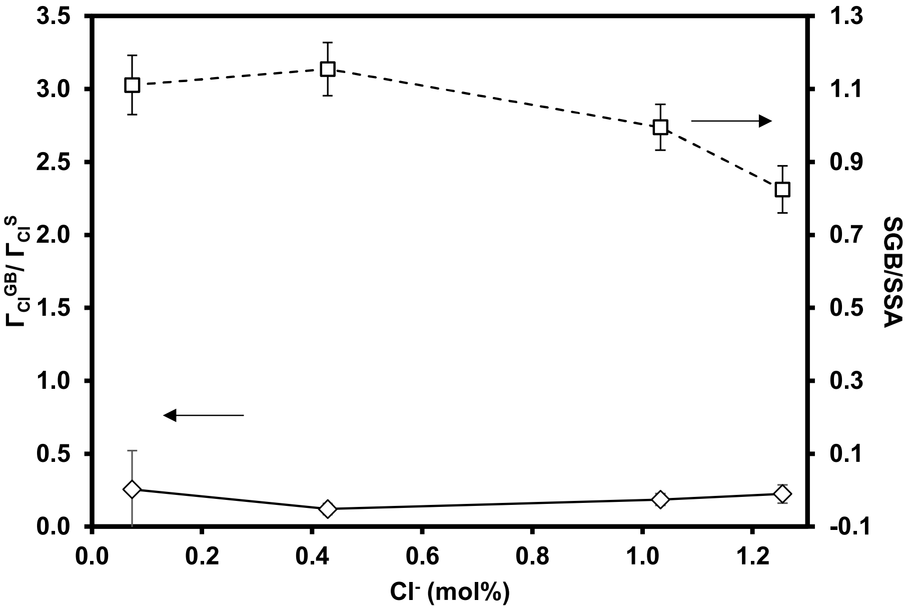

Figure 20. The optimal calculated $\Gamma_{Cl}^{GB}/\Gamma_{Cl}^{S}$ ratio and S_{GB}/S_{BET} ratio versus the total amount of #2 Cl⁻.

For #1 and #2 F⁻-doped the Γ_F^{GB} is dominant above Γ_F^{S} resulting in $\Gamma_F^{GB}/\Gamma_F^{S}$ ratio values greater than 1 (Table 7), with the only exception for #1ZnO-7, where the inverse occurs Γ_F^{S} > Γ_F^{GB} with a ratio of ~0.20. Indeed, the $\Gamma_F^{GB}/\Gamma_F^{S}$ ratio varying significantly, without a pattern to reach a constant value, thus the solubility could not be estimated and a zero bulk solubility was assumed. Figure 21 presents the #1 F⁻-doped $\Gamma_F{}^{GB}/\Gamma_F{}^{S}$ ratio, which had the greatest variation.

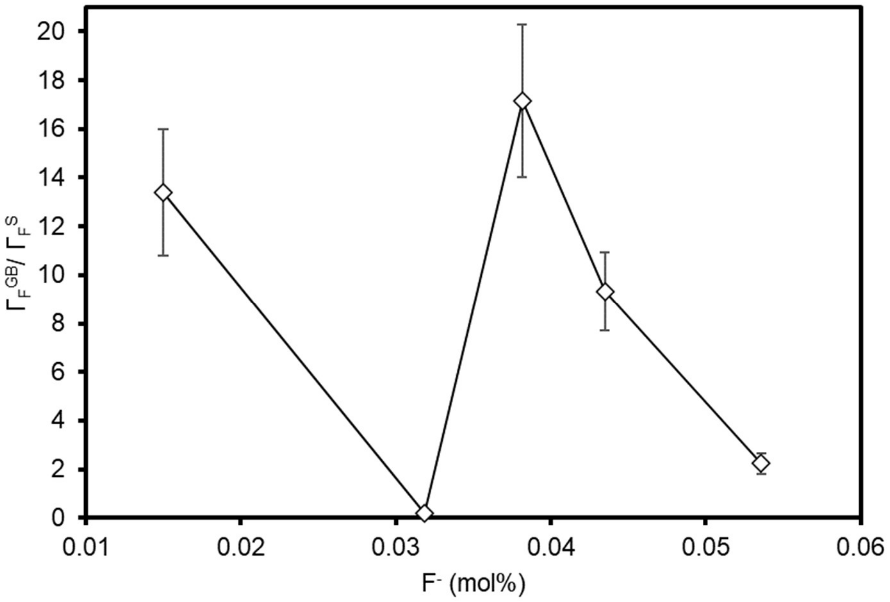

Figure 21. #1 F⁻ excess ratio between interfaces of ZnO, thus the excess in the grain boundary divided by the excess on the surface.

Table 7. Interface excesses on Cl^- and F^--doped ZnO and the undoped sample. Due to F^- relative lower content, three decimal places are shown to ensure at least two significant digits.

Sample	Cl^- (mol%)	Γ_{Cl}^{S} (μmol/m^2)	Γ_{Cl}^{GB} (μmol/m^2)	$\Gamma_{Cl}^{GB}/\Gamma_{Cl}^{S}$
#1ZnO-0	0.07 ± 0.01	0.30 ± 0.02	0.12 ± 0.03	0.39 ± 0.13
#1ZnOCl-1	0.37 ± 0.03	2.66 ± 0.22	0.41 ± 0.07	0.15 ± 0.04
#1ZnOCl-3	0.80 ± 0.07	3.95 ± 0.32	1.55 ± 0.20	0.39 ± 0.08
#1ZnOCl-4	0.98 ± 0.09	5.13 ± 0.44	1.80 ± 0.20	0.35 ± 0.07
#1ZnOCl-6	1.23 ± 0.11	6.77 ± 0.59	2.92 ± 0.27	0.43 ± 0.08
Sample	F^- (mol%)	Γ_{F}^{S} (μmol/m^2)	Γ_{F}^{GB} (μmol/m^2)	$\Gamma_{F}^{GB}/\Gamma_{F}^{S}$
#1ZnO-0	0.015 ± 0.001	0.010 ± 0.001	0.138 ± 0.013	13.41 ± 2.60
#1ZnOF-1	0.038 ± 0.003	0.022 ± 0.002	0.383 ± 0.035	17.17 ± 3.13
#1ZnOF-3	0.043 ± 0.004	0.037 ± 0.003	0.346 ± 0.032	9.31 ± 1.62
#1ZnOF-5	0.054 ± 0.005	0.143 ± 0.013	0.319 ± 0.029	2.23 ± 0.41
#1ZnOF-7	0.032 ± 0.003	0.188 ± 0.017	0.036 ± 0.003	0.19 ± 0.03
Sample	Cl^- (mol%)	Γ_{Cl}^{S} (μmol/m^2)	Γ_{Cl}^{GB} (μmol/m^2)	$\Gamma_{Cl}^{GB}/\Gamma_{Cl}^{S}$
#2ZnO-0	0.07 ± 0.01	0.15 ± 0.01	0.45 ± 0.04	0.26 ± 0.27
#2ZnOCl-1	0.43 ± 0.04	2.14 ± 0.19	1.30 ± 0.11	0.12 ± 0.04
#2ZnOCl-3	1.03 ± 0.09	4.63 ± 0.41	2.92 ± 0.26	0.19 ± 0.04
#2ZnOCl-6	1.25 ± 0.11	6.32 ± 0.55	3.63 ± 0.32	0.23 ± 0.06
#2ZnO-0 1LX	0.06 ± 0.01	0.05 ± 0.01	0.05 ± 0.03	0.99 ± 0.69
#2ZnOCl-1 1LX	0.23 ± 0.02	0.72 ± 0.07	0.18 ± 0.06	0.25 ± 0.11
#2ZnOCl-3 1LX	0.41 ± 0.04	1.48 ± 0.14	0.54 ± 0.10	0.37 ± 0.10
#2ZnOCl-6 1LX	0.47 ± 0.04	1.52 ± 0.14	0.96 ± 0.12	0.63 ± 0.14
#2ZnOCl-1 5LX	0.07 ± 0.01	0.09 ± 0.01	0.09 ± 0.04	1.03 ± 0.53
#2ZnOCl-6 5LX	0.26 ± 0.03	0.17 ± 0.02	1.34 ± 0.18	7.91 ± 1.85
Sample	F^- (mol%)	Γ_{F}^{S} (μmol/m^2)	Γ_{F}^{GB} (μmol/m^2)	$\Gamma_{F}^{GB}/\Gamma_{F}^{S}$
#2ZnO-0	0.012 ± 0.001	0.031 ± 0.003	0.067 ± 0.006	2.18 ± 0.40
#2ZnOF-1	0.011 ± 0.001	0.021 ± 0.002	0.056 ± 0.005	2.61 ± 0.48
#2ZnOF-3	0.013 ± 0.001	0.059 ± 0.005	0.026 ± 0.003	0.45 ± 0.09
#2ZnOF-5	0.034 ± 0.003	0.150 ± 0.014	0.072 ± 0.007	0.48 ± 0.09
#2ZnOF-7	0.033 ± 0.003	0.188 ± 0.017	0.052 ± 0.005	0.27 ± 0.05
#2ZnO-0 1LX	0.018 ± 0.002	0.019 ± 0.002	0.095 ± 0.009	5.07 ± 0.94
#2ZnOF-1 1LX	0.018 ± 0.002	0.018 ± 0.002	0.087 ± 0.008	4.95 ± 0.92
#2ZnOF-3 1LX	0.019 ± 0.002	0.021 ± 0.002	0.066 ± 0.006	3.13 ± 0.58
#2ZnOF-5 1LX	0.021 ± 0.002	0.035 ± 0.003	0.082 ± 0.008	2.32 ± 0.43
#2ZnOF-7 1LX	0.027 ± 0.003	0.034 ± 0.003	0.127 ± 0.012	3.69 ± 0.69

First, analyzing the #1 Cl⁻-doped, Figure 19 exhibits both the interface excesses $\mathit{\Gamma}_{Cl}{}^{S}$ and $\mathit{\Gamma}_{Cl}{}^{GB}$ according to the Cl⁻ content. $\mathit{\Gamma}_{Cl}{}^{S}$ increases for higher amounts of Cl⁻ added to the system, with an approximately linear trend. It is possible to notice that the $\mathit{\Gamma}_{Cl}{}^{S}$ surpasses the grain boundary excess at all tested dosages, which also presents a linear variation with the increase in Cl⁻ content. The #2 Cl⁻-doped interface excesses, in Figure 20, follow the same trend as #1. On lixiviated samples presented in Figure 21, as the total Cl⁻ diminishes in 1 LX, the $\mathit{\Gamma}_{Cl}{}^{S}$ reduces significantly approaching $\mathit{\Gamma}_{Cl}{}^{GB}$, which reduces much less. On the intensive lixiviation, 5LX, the $\mathit{\Gamma}_{Cl}{}^{GB}$ surpasses $\mathit{\Gamma}_{Cl}{}^{S}$, and this difference is greater for the higher dosage.

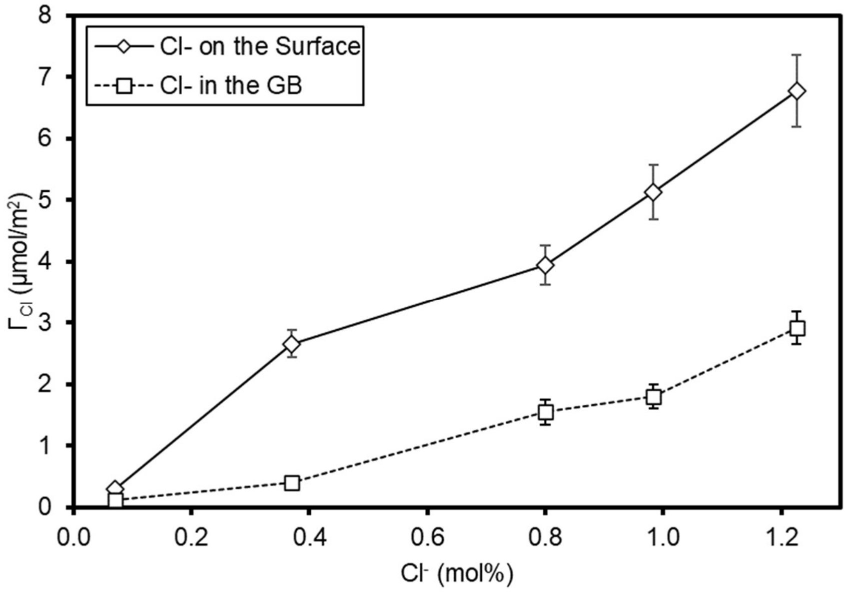

Figure 22. Surface and GB Cl⁻ excess in ZnO #1 according to the total Cl⁻.

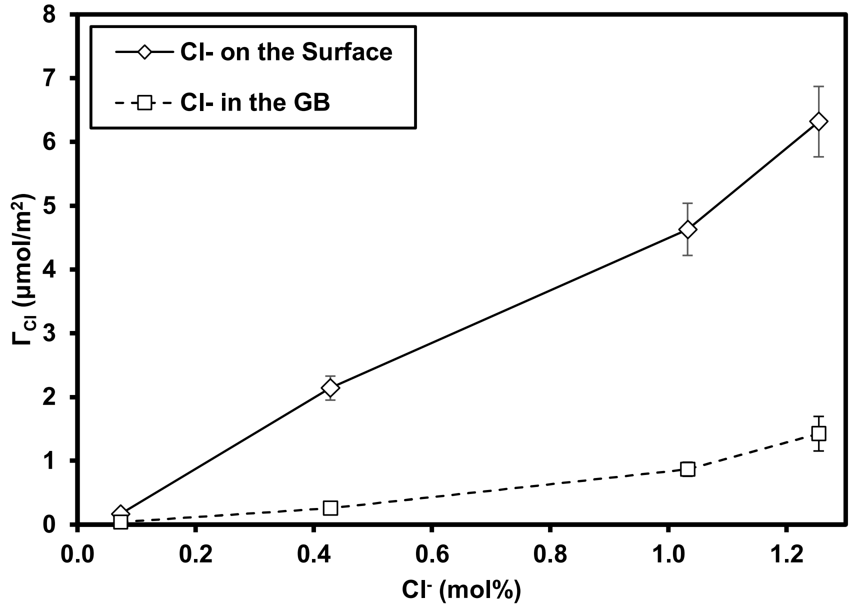

Figure 23. Surface and GB Cl⁻ excess in ZnO #2 according to the total Cl⁻.

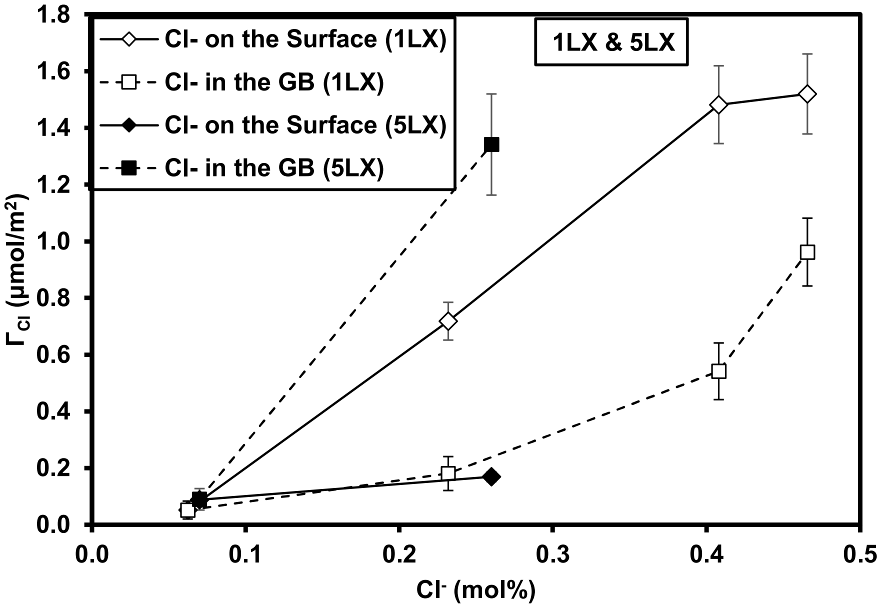

Figure 24. Surface and GB Cl⁻ excess in lixiviated ZnO #2 according to the total Cl⁻.

Second, on the #1 F⁻-doped Γ presented in Figure 22. Differently, from Cl⁻-doping, the ${\Gamma_F}^{GB}$ is most of the time higher than ${\Gamma_F}^{S}$, thus showing a GB preference or the best imprisoning site against thermal loss. The sequence of ZnOF-1, ZnOF-3, and ZnOF-5 (higher F⁻ content samples) noticed a ${\Gamma_F}^{GB}$ decrease while an even higher ${\Gamma_F}^{S}$ increase. This effect cannot be fully explained by the reduction of S_{GB}/S_{BET} ratio of 1.23, 1.12, and 1.05, respectively, because even though the GB concentration was kept constant, averaging ~5.76 µmol/g, the surface concentration increases 0.26, 0.58, and 2.35 µmol/g. Hence, the ${\mathit{\Gamma}_F}^S$ could have led to a threshold that trigged enhanced F⁻ loss because the next increment of F⁻ (ZnOF-7) showed the lowest F⁻ content. Although the ${\mathit{\Gamma}_F}^S$ for ZnOF-7 achieved its highest, the ${\mathit{\Gamma}_F}^{GB}$ dropped dramatically, below the undoped ${\mathit{\Gamma}_F}^{GB}$, almost vanishing. On the contrary, #2 F⁻-doped interface excesses, in Figure 23, show most ${\mathit{\Gamma}_{Cl}}^S$ greater than ${\mathit{\Gamma}_F}^{GB}$, such imprecisions can be attributed to the low retained dopant. However, with one lixiviation procedure, 1LX (Figure 24), all ${\mathit{\Gamma}_{Cl}}^{GB}$ surpasses ${\mathit{\Gamma}_{Cl}}^S$.

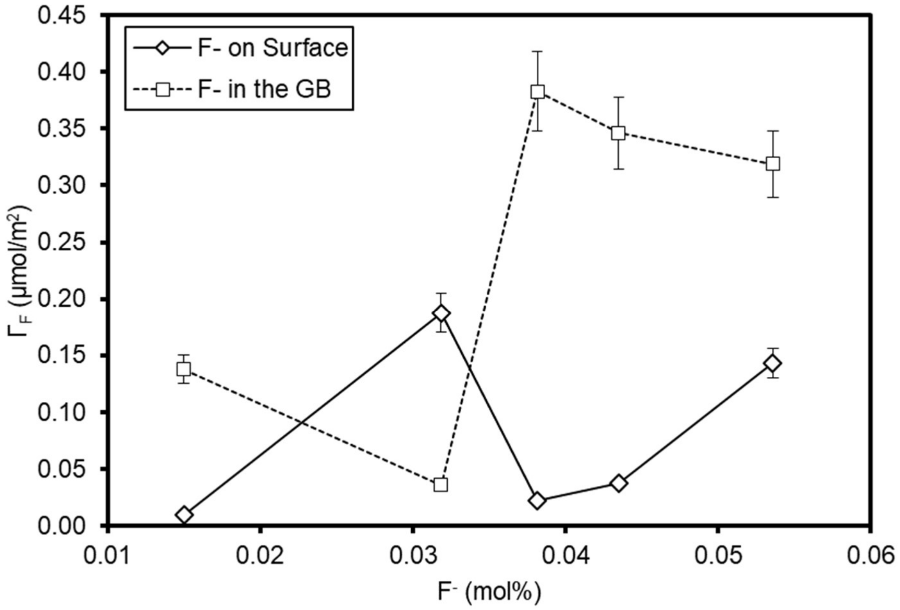

Figure 25. Surface and GB F⁻ excess in ZnO #1 according to the total F⁻.

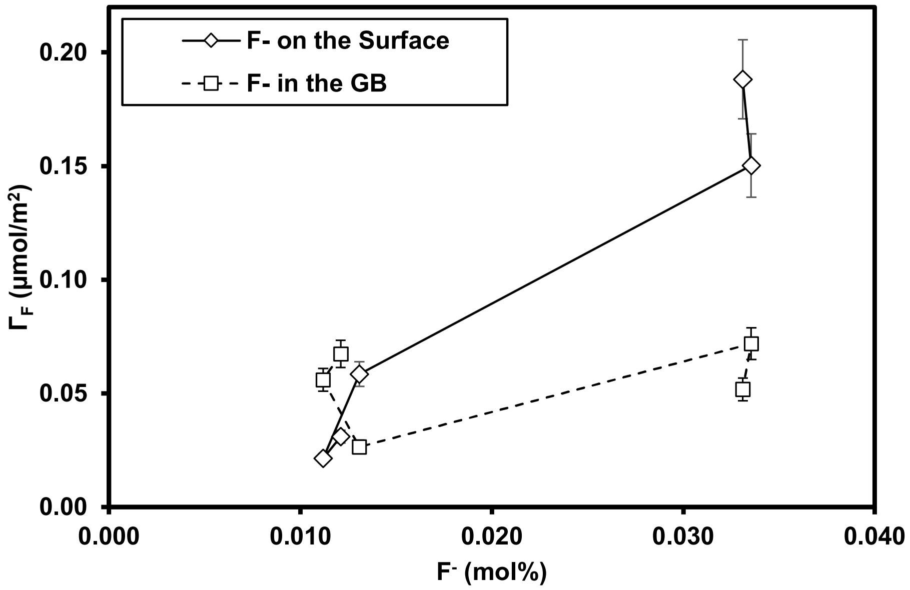

Figure 26. Surface and GB F⁻ excess in ZnO #2 according to the total F⁻.

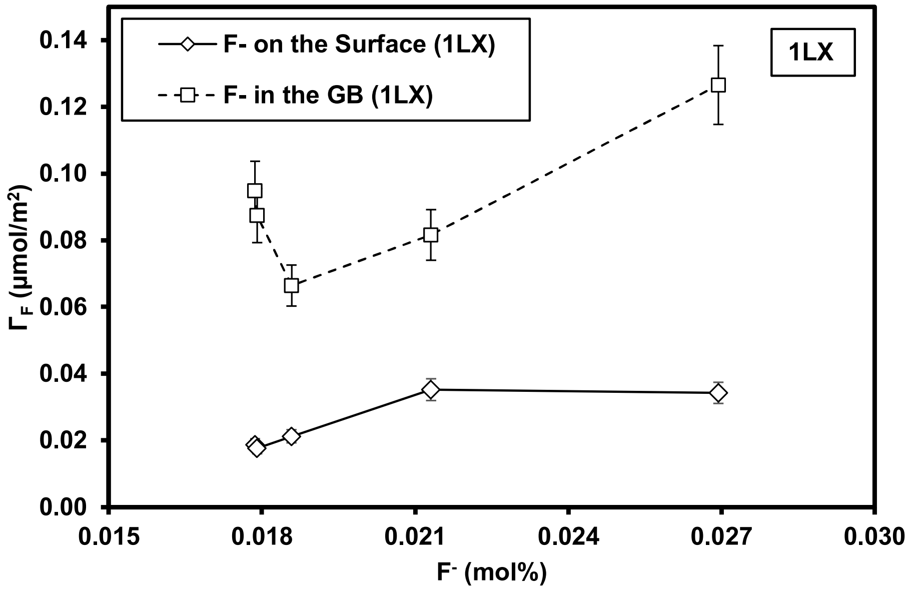

Figure 27. Surface and GB F⁻ excess in lixiviated ZnO #2 according to the total F⁻.

5.2 Electrical conductivity

5.2.1 Impedance analysis of the first batch (#1)

Figures 28 and 29 present the IS diagrams of #1 measured at 150°C for Cl^- and F^--doped ZnO pellets, respectively. Typically, IS data are composed of multiple semicircular arcs representing the relaxations of different microstructural components in the material, such as grains, grain boundaries, and other blocking interfaces such as pores and insulating phases, along with possible electrode polarization. For the prepared pellets, although being monophasic, the unsintered pressed powder possess roughly half of its volume of pores, where conduction path is formed by GB that bridges grains. Thus, such a high porosity significantly increases the tortuosity of the conduction path, which also increases the overall measured electrical resistance. However, all samples in Figures 28 and 29 display semicircular arcs, which is typically ascribed to charge carrier blocking at the grain boundaries and pores [51, 122, 135, 136], the primary resistive interface continuously connecting the solid pellets. The low-frequency contribution dominates and overlaps other possible microstructural features, forming a single irregular semicircular arc. From the raw data of the measurement, the electrical resistance R was determined. Geometrically, according to Equation 19, where A_{Φ} is the circular cross-section area of the pellet and h_p is the height of the cylindrical pellet, we could calculate the electrical resistivity (ρ_e) and its inverse giving the electrical conductivity (σ). Figures 28 and 29 are represented in terms of ρ_e.

$$\sigma = \frac{1}{\rho_e} = \frac{h_p}{R\,A_{\Phi}} \tag{19}$$

In both #1 Cl^- and F^--doped ZnO, the ρ_e was of the undoped material (ZnO-0) followed by the 1 mol% added dopant (ZnOCl-1 and ZnOF-1). For Cl^--doped, the drop of ρ_e happened according to the increase in total Cl^-, while for F^--doped, the ZnOF-7 disrupted tendencies being of significant low F^- content but presenting ρ_e in between the highest F^--samples. However, the Cl^--doped samples presented a 15-times lower ρ_e than the F^--doped. The main outcome is the striking decrease in the electrical resistivity upon Cl^- and F^--doping. Considering that the samples have similar porosities (~46.6 ± 3.5 vol%) and were carefully prepared at the same experimental conditions to minimize adsorbed species in the porous structure of the samples, such a pronounced decrease of the resistivity is mainly related to the effect of doping.

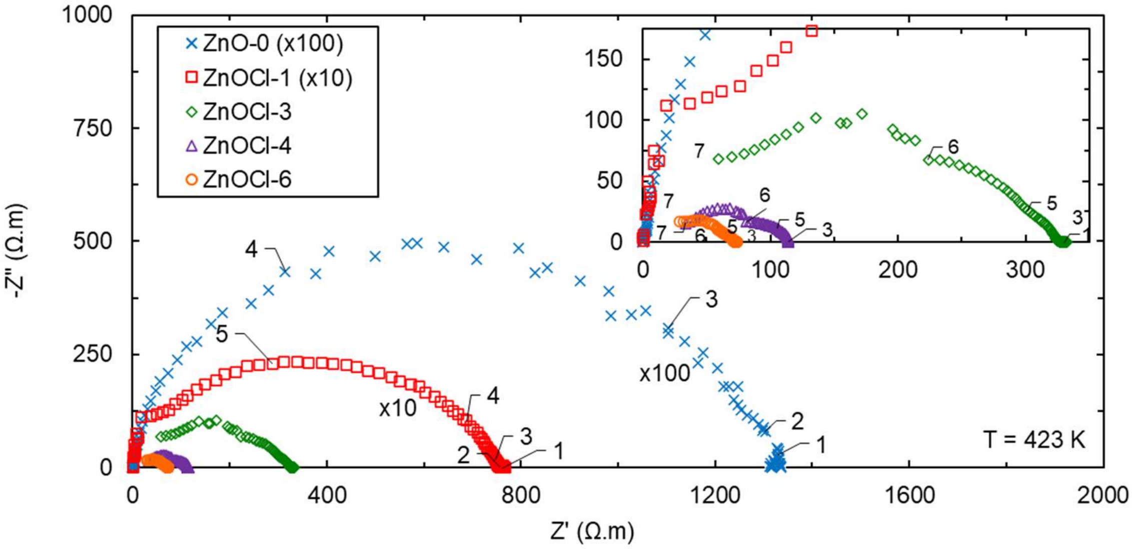

Figure 28. Impedance measurements of #1 Cl⁻-doped ZnO pellets, performed at 150 °C. Numbers indicate the logarithm of the frequency.

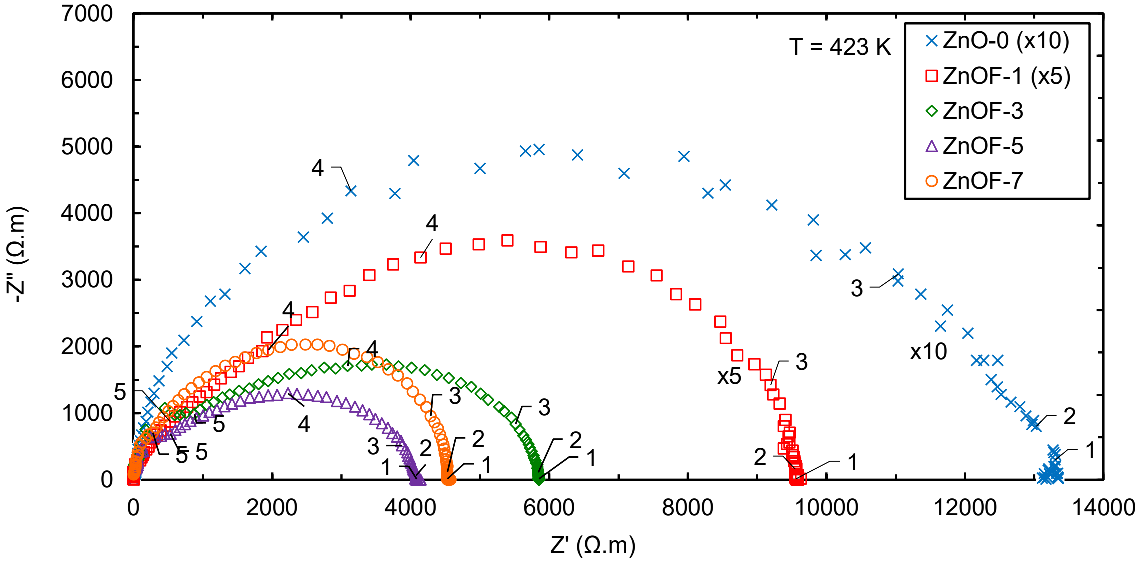

Figure 29. Impedance measurements of #1 F⁻-doped ZnO pellets, performed at 150 °C. Numbers indicate the logarithm of the frequency.

The values of resistance (R) and σ are presented in Table 8, also the dimension of pellets and their porosity. Notably, with the lower R of Cl⁻-doped samples attain a higher σ than the F⁻-doped samples. In comparison, the highest Cl⁻-doped σ, ZnOCl-6, achieved a value of 58-times larger than the most conductive F⁻-doped sample, ZnOF-3. Whereas σ gives us a more direct resemblance of the material as it considers the differences in the dimension of the pellets. Although it does not consider the porosity, which can cause variations, higher porosity would reduce σ. However, the obtained porosity was kept reasonably constant between 40.9 vol% to 50.4 vol%, even regarding the compared samples ZnOCl-6 and ZnOF-3, that show overlaid value of porosity 48.7 ± 1.0 vol% and 49.5 ± 1.6 vol%, respectively.

Table 8. Resistance obtained from impedance tests of #1 Cl^- and F^--doped ZnO pellets at 150°C and the calculated electrical conductivity. The dimension of the pellets and their porosity.

Sample	R (Ω)	σ (150°C) ($\Omega^{-1}\cdot cm^{-1}$)	h_p (mm)	A_Φ (mm^2)	Porosity (vol%)
ZnO-0	6.0×10^6	7.5E−06	4.49 ± 0.01	100.38 ± 0.23	41.7 ± 0.6
ZnOCl-1	3.3×10^5	1.3E−04	4.44 ± 0.01	100.61 ± 0.33	40.9 ± 1.1
ZnOCl-3	1.5×10^4	3.0E−03	4.63 ± 0.01	100.31 ± 0.33	41.8 ± 0.7
ZnOCl-4	6.0×10^3	8.8E−03	5.31 ± 0.00	101.43 ± 0.04	50.2 ± 0.4
ZnOCl-6	3.6×10^3	1.4E−02	5.03 ± 0.01	101.19 ± 0.02	48.7 ± 1.0
ZnOF-1	2.1×10^6	2.3E−05	4.99 ± 0.01	101.96 ± 0.84	48.8 ± 1.4
ZnOF-3	2.7×10^5	1.8E−04	5.00 ± 0.01	101.61 ± 0.35	49.5 ± 1.6
ZnOF-5	2.1×10^5	2.4E−04	5.24 ± 0.00	101.35 ± 0.14	50.4 ± 0.8
ZnOF-7	2.3×10^5	2.2E−04	5.09 ± 0.01	101.36 ± 0.29	49.7 ± 0.4

The increase in electrical conductivity in doped semiconductors is usually associated with an increase in the number of charge carriers (N). In the case of Cl^--doped ZnO, it is usually considered that the Cl^- would form a solid solution with ZnO substituting O^{2-} and generating one electronic charge carrier, which would increase the electrical conductivity proportionally to the amount of N increased. The electrical conductivity (σ) is defined by the number of charge carriers, their mobility (μ), and their charge ($|e| = 1.6 \times 10^{-19}$ C, for electrons), recalling Equation 3 (in a different format: $\sigma \cong \mathrm{N}\, \mu\, |e|$) [58]. By assuming that each Cl^- in the lattice generates a charge carrier, N should increase proportionally to the total amount of Cl^- in the doped samples. Consequently, electrical conductivity would increase proportionally. To determine if this proportionality applies to the present system, we have calculated the increase in charge carrier by assuming that each Cl^- is generating one mobile electron-hole pair. Thus, we have compared this increment to the observed increase in electrical conductivity shown in Table 8. A comparison between the measured increase in σ and the expected increase due to charge carriers (N) increase is presented in Figure 30.

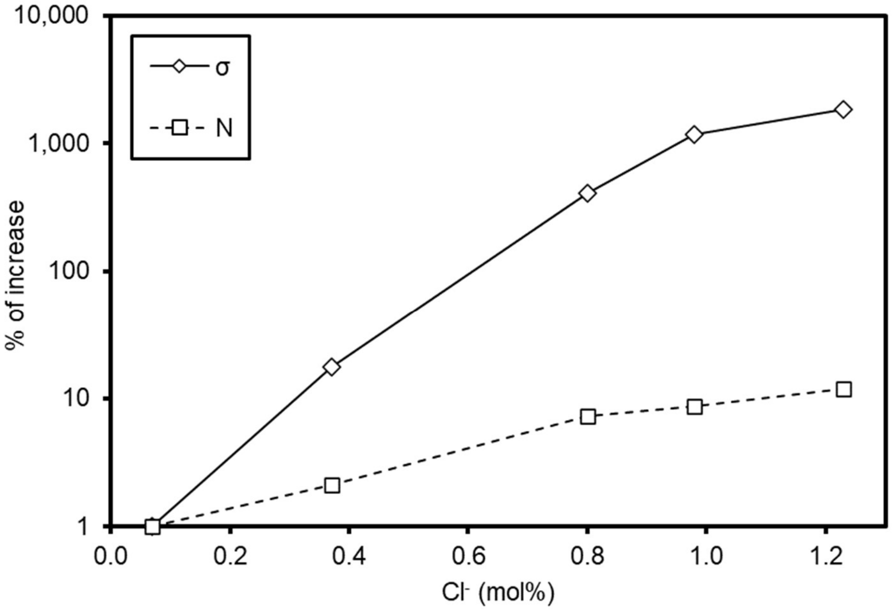

Figure 30. Relative increase (%) in electrical conductivity (σ) and in the number of charge carriers (N) versus total amount of Cl^-.

According to Figure 30, the increase in electrical conductivity measured for our samples significantly surpasses a possible increase due to the number of charge carriers that would be added to the system if each Cl^- generates one N. As the substitution of O^{2-} by Cl^- introduces a shallow donor state derived from Cl 3s states [12]. In such a case, the number of N in the system to fit the electrical conductivity expectations associated with the bulk properties (Equation 3) would be 1N, 8N, 55N, 134N, and 156N for ZnO-0, ZnOCl-1, ZnOCl-3, ZnOCl-4, and ZnOCl-6 samples, respectively. However, the results obtained from our calculations suggest that the phenomenon is not associated with the bulk doping effect. Therefore, electrical conductivity increment is possibly caused by a GB modification. To check the relationship between the total amount of Cl^- and the calculated GB excess with the electrical conductivity, we have plotted Figure 31.

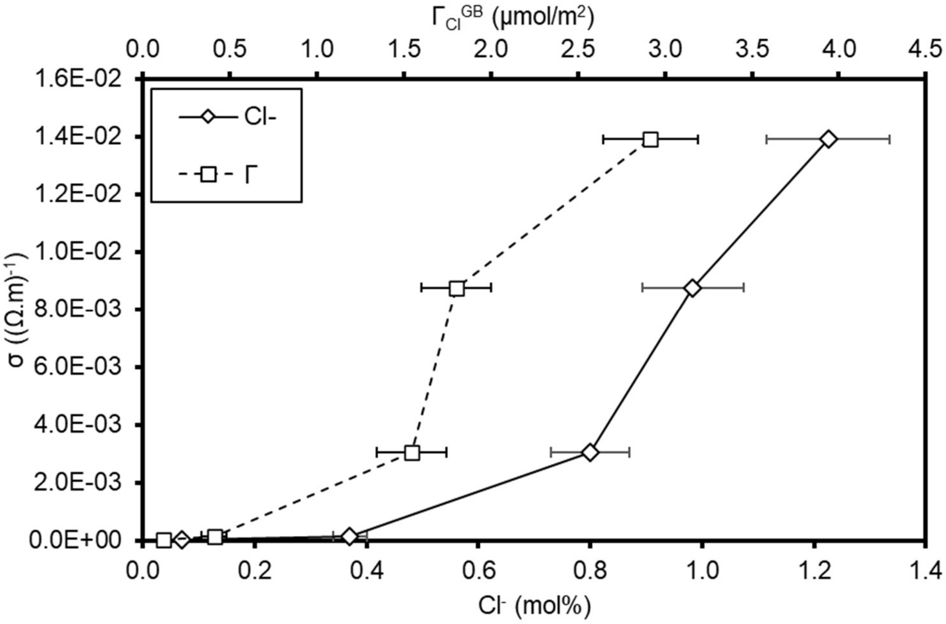

Figure 31. The amount of Cl⁻ and GB excess plotted against the electrical conductivity #1.

From Figure 31 is observed that the electrical conductivity increase matches the increase in the GB excess. The data suggest that the GB segregation plays a crucial role in this matter. A significant improvement in the electrical conductivity of four orders of magnitude (1857 times) that cannot be explained by promoting more electrons in the CB, as evidenced by Figure 30.

In polycrystalline materials, the grain boundary acts as a barrier, which prevents the electrons from moving freely throughout the sample. This barrier is known as space charge layer, which is associated with an electrical potential barrier height (φ_B).This φ_B can be calculated when no external voltage bias is applied (V = 0) by Equation 20 [13, 47]. Where, $|e|$ is the modulus of electron charge (1.6 x 10^{-19} C), ε_0 the permittivity of free space (8.85 x 10^{-12} F/m), ε_r the relative permittivity (ε_r = 8.5 for ZnO [137]), and N_d the charge carrier concentration within the electron depletion layer of thickness d, which for relative calculations, was assumed to be 1 nm in the present system. The determination of N_d is not possible, but considering that each Cl^- from the $\Gamma_{Cl}{}^{GB}$ could cancel one positive charge, we can calculate how a variation in N_d (ΔN_d), from the undoped sample (ZnO-0), relative to the doped ones, could cause a variation in $\Delta\varphi_B$ according to Equation 21.

$$\varphi_B = \frac{|e|^2 \mathrm{d}^2 \mathrm{N_d}}{2\varepsilon_0\varepsilon_r} \tag{20}$$

$$(\Delta\varphi_B) = \frac{|e|^2 \mathrm{d}^2 (\Delta \mathrm{N_d})}{2\varepsilon_0 \varepsilon_r} \tag{21}$$

Figure 32 shows the decrease of $\Delta\varphi_B$, relative to ZnO-0, plotted as a function of the volumetric concentration of Cl⁻ at the GB. Even though the initial electrical potential barrier, φ_{B0} of the undoped ZnO (ZnO-0), was not determined, it decreased linearly with the increasing amount of Cl⁻ at the GB. Such behavior suggests that the ${\Gamma_{Cl}}^{GB}$ plays a decisive role in decreasing the φ_B and, consequently, increasing the electrical conductivity. ZnO potential barrier height has been reported to be 530-800 meV at temperatures up to 400°C [138, 139], thus a reduction of 595 meV (ZnOCl-6) seen in this study is noteworthy, resembling at least a 75% decrease in the potential barrier height.

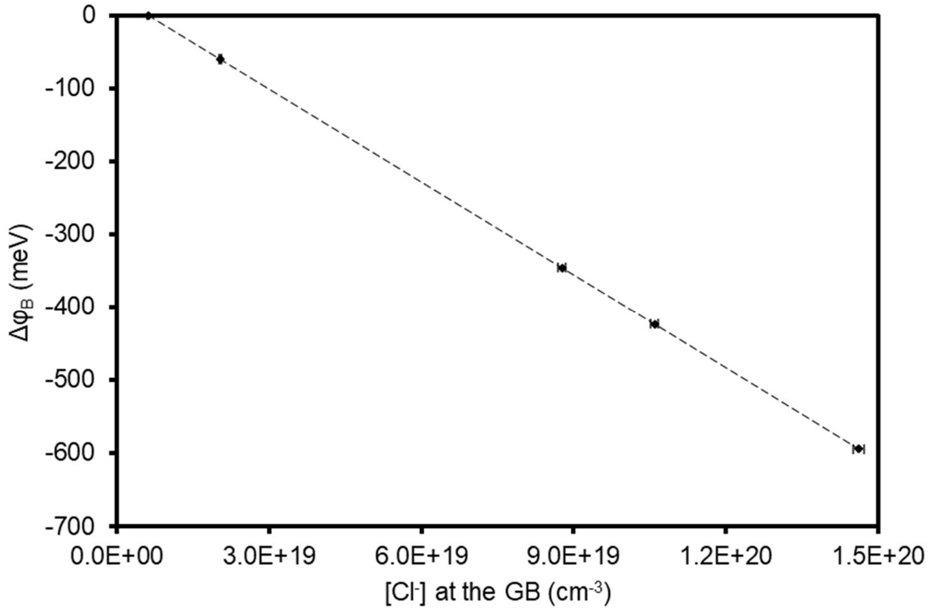

Figure 32. Electrical potential barrier dependence on the Cl⁻ concentration at the GB of #1 Cl⁻-doped ZnO.

Figure 33 gives the grain electrical conductivity (σ_G) with the Cl⁻ content. The σ_G was calculated from the Z' taken before the semicircular behavior of the impedance measurement. Determining this point involved precision issues, but is enough to differentiate the σ_G between the presented results. Samples ZnO-0, ZnOCl-1, and ZnOCl-3, in which the Cl⁻ content is not above 0.80 mol%, present the same σ, while higher dosages exhibited a linear increase in conductivity, reaching twice the value of ZnO-0. This indicates that a higher Cl⁻ concentration dissolved in bulk was active for the

ZnOCl-4 and ZnOCl-6 compositions at 150°C. Nevertheless, again confirming that ${\Gamma_{Cl}}^{GB}$ is more relevant for the overall conductivity than bulk solubility and punctual defects induced by dopant in the bulk.

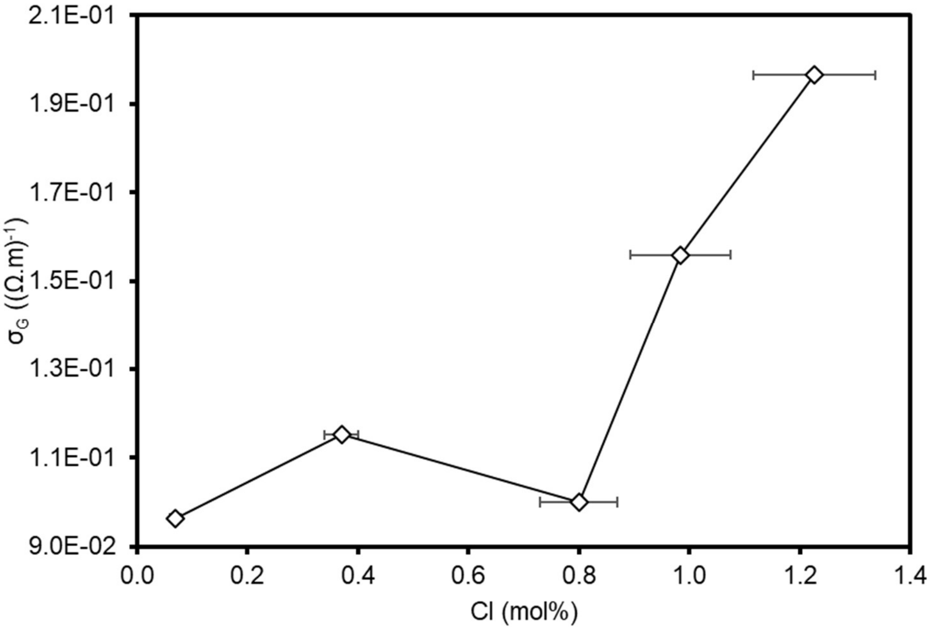

Figure 33. Electrical grain conductivity of Cl⁻-doped nano-ZnO versus total Cl⁻.

In the case of F⁻-doped, Figure 34 shows an odd correlation of total F⁻ and ${\Gamma_F}^{GB}$ with σ, forming two "N-shape" behaviors. The one bending to the right is the total F⁻, and either with low and moderate F⁻, the σ was low, but with a slightly less moderate F⁻, the σ is at the level of the F⁻-richer samples. Regarding ${\Gamma_F}^{GB}$, a "N" bending to the left demonstrates that high or low Γ can either favor high or low σ. Due to this behavior, the assumption that each F⁻ in the bulk would generate a charge carrier N is discarded as the increase of F⁻ is not directly associated with improvement in electrical conductivity. Also, a calculated $\Delta\varphi_B$ with the volumetric concentration of F⁻ at the GB would not be coherent according to Figure 27.

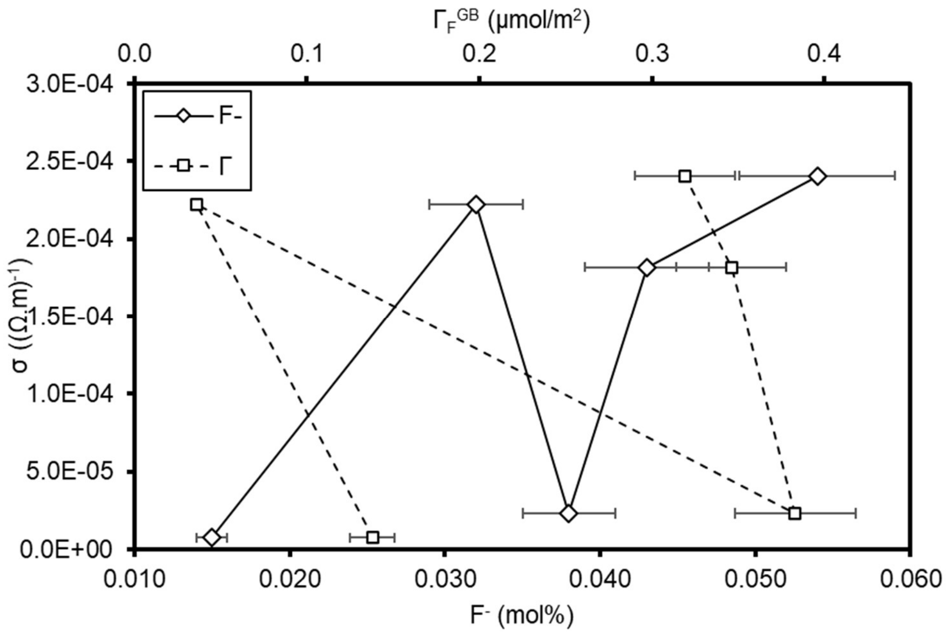

Figure 34. The amount of F^- and GB excess plotted against the electrical conductivity #1.

Hence, a better explanation was sought of how ${\Gamma_F}^S$ could affect the σ, presented in Figure 35. A correlation of higher ${\Gamma_F}^S$ leading to higher σ was found, suggesting a surface electrical current can be the easiest path between grains. As grains were far from densified, residual adsorption groups could be collaborating to improve σ.

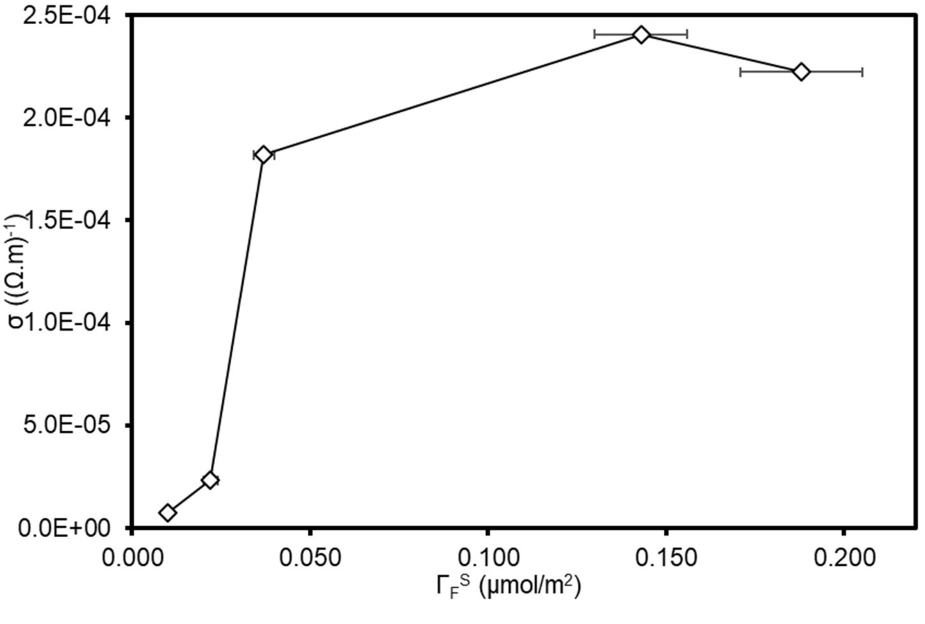

Figure 35. Electrical conductivity of #1 F^--doped nano-ZnO versus F^- surface excess.

Evaluating the σ_G with the F⁻ content, shown in Figure 36, we observe no clear tendency, partially due to the impression of obtaining these values. However, two out of the three F⁻-richest samples show a roughly 30% increase in σ_G. Again, ZnOF-7 differs, showing the highest σ_G, almost twice the ZnO-0. Leading to the hypothesis that F⁻, once located in the GB, for some unknown reason, left to stabilize the surface, and part of it stayed in the bulk.

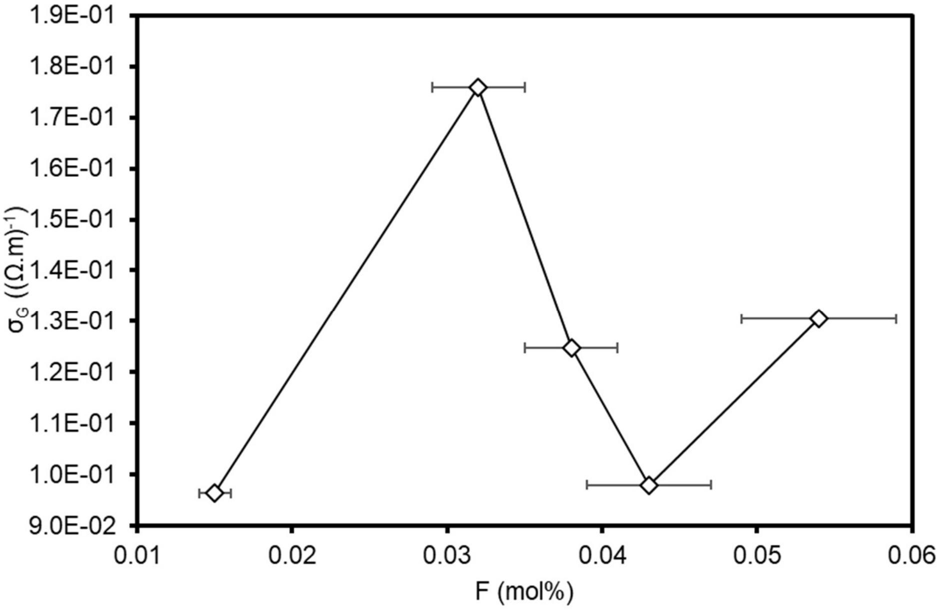

Figure 36. Electrical grain conductivity of #1 F⁻-doped nano-ZnO versus total F⁻.

5.2.2 Activation energy of the first batch (#1)

To further understand the sudden increase in the overall electrical conductivity, we have estimated the activation energy for conduction, according to the Arrhenius equation, Equation 22 [121]. Where σ_i is an intrinsic conductivity in S/cm, T is the absolute temperature given in K, R is the ideal gas constant 0.0000862 eV/K, and E_a is the activation energy in meV (or eV). Hence, we obtained E_a from the angular coefficient of the linear plots (ln σ x 1/T), all shown in Figure 37, using three different temperatures: 200°C, 150°C, and 100°C.

$$\ln \sigma = \ln \sigma_i + \frac{1}{T}\left(\frac{-E_a}{R}\right) \tag{22}$$

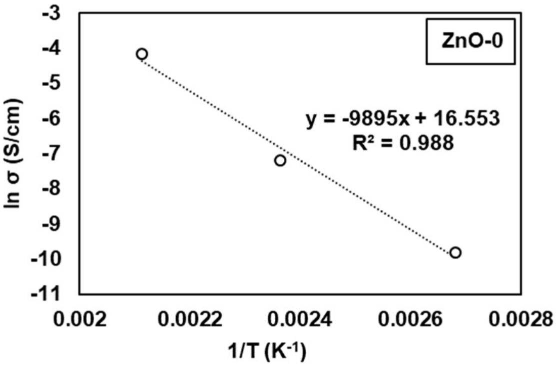
ZnO-0
y = -9895x + 16.553
R² = 0.988
ln σ (S/cm)
-3
-4
-5
-6
-7
-8
-9
-10
-11
0.002
0.0022
0.0024
0.0026
0.0028
1/T (K-1)

(a)

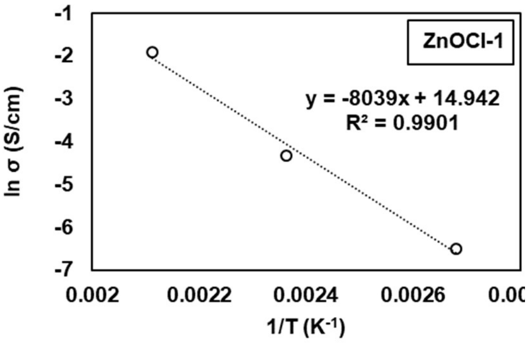
ZnOCl-1
y = -8039x + 14.942
R² = 0.9901
ln σ (S/cm)
-1
-2
-3
-4
-5
-6
-7
0.002
0.0022
0.0024
0.0026
0.00
1/T (K-1)

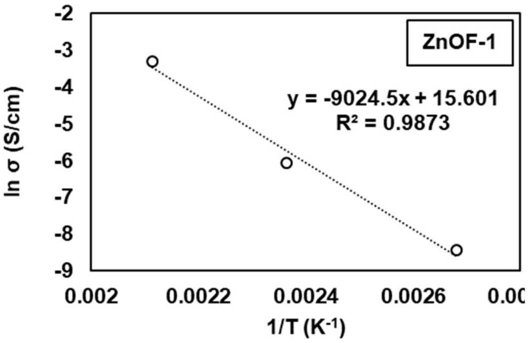
ZnOF-1
y = -9024.5x + 15.601
R² = 0.9873
ln σ (S/cm)
-2
-3
-4
-5
-6
-7
-8
-9
0.002
0.0022
0.0024
0.0026
0.00
1/T (K-1)

(b)

(f)

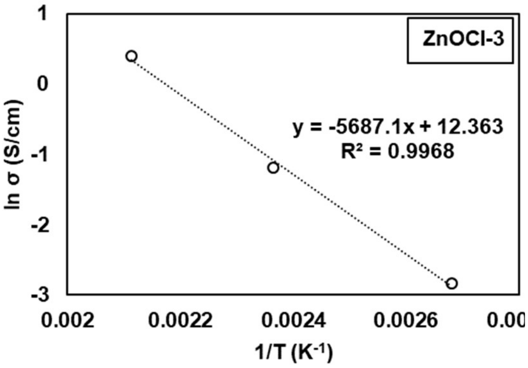
ZnOCl-3
y = -5687.1x + 12.363
R² = 0.9968
ln σ (S/cm)
1
0
-1
-2
-3
0.002
0.0022
0.0024
0.0026
0.00
1/T (K-1)

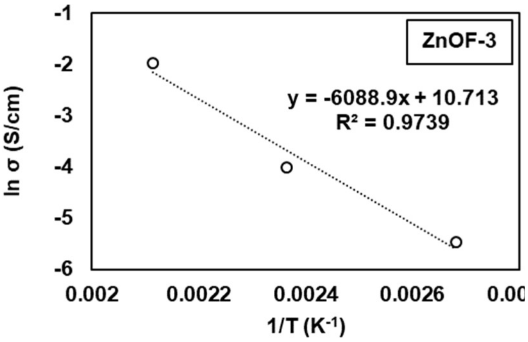
ZnOF-3
y = -6088.9x + 10.713
R² = 0.9739
ln σ (S/cm)
-1
-2
-3
-4
-5
-6
0.002
0.0022
0.0024
0.0026
0.00
1/T (K-1)

(c)

(g)

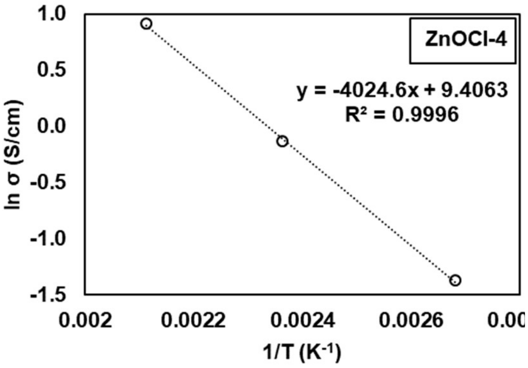
ZnOCl-4
y = -4024.6x + 9.4063
R² = 0.9996
ln σ (S/cm)
1.0
0.5
0.0
-0.5
-1.0
-1.5
0.002
0.0022
0.0024
0.0026
0.00
1/T (K-1)

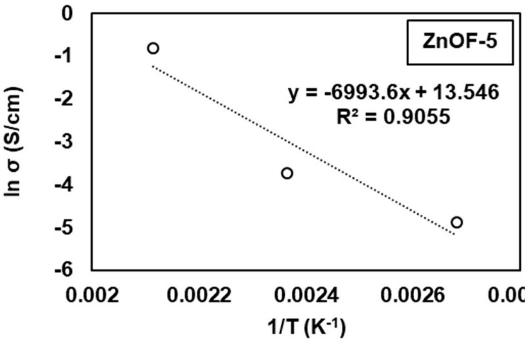
ZnOF-5
y = -6993.6x + 13.546
R² = 0.9055
ln σ (S/cm)
0
-1
-2
-3
-4
-5
-6
0.002
0.0022
0.0024
0.0026
0.00
1/T (K-1)

(d)

(h)

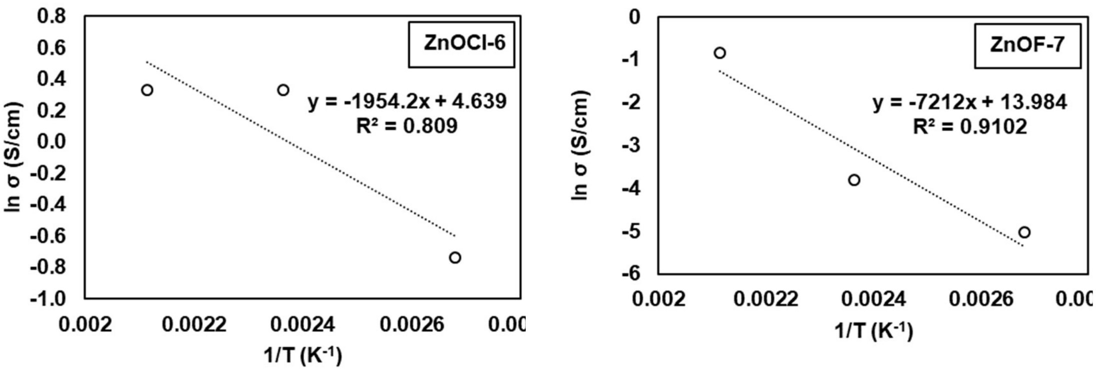

(e) (i)

Figure 37. Linearized Arrhenius equation of electrical conductivity versus the inverse of temperature, to calculate according to Equation 22, the activation energy for electrical conductivity. The angular coefficient of each of these plots is equal to correspondent sample's $-E_a/R$.

The calculated E_a as a function of the amount of Cl^- and F^- in each sample are presented in Figures 38 and 39, respectively.

Figures 37 shows how E_a reduces linearly as the amount of Cl^--doping increases. The calculated E_a decreased from 853 meV (undoped ZnO) to 168 meV (1.23 mol% Cl^--doped ZnO) an 80% decrease. The value for undoped ZnO agrees with the range reported in the literature. Lee et al. [51] have reported the E_a of pure ZnO as 570 meV for crystallite sizes of ~60 nm, while Godarvati et al. [140] have recently reported E_a = 1,081 meV for crystallite sizes of ~40 nm. The reduction of 685 meV in the E_a from undoped to 1.23 mol% Cl^--doped ZnO agrees with the 595 meV reduction in φ_B calculated at an intermediate temperature (150°C) instead of the three temperatures (200, 150, and 100°C) used to calculate the E_a. The equivalent magnitude of these values reinforces that the pronounced improvement in overall electrical conductivity is primarily due to the segregation of Cl^- in the GBs, which reduces the φ_B. Significant changes in the activation energy can be attributed to different transport mechanisms or different charge carriers activated in the material. However, in the case of ZnO, an n-type semiconductor, at a relatively low-temperature range presented in this study (100-200°C), and with the observed correlation with φ_B, it is assured that the conductivity is electronic, having electrons as the main charge carries. This behavior has been associated with the formation of electron donor levels due to the ionization processes that form oxygen vacancies and zinc interstitials [52, 140]. Ionic conductivity has been reported for ZnO at higher temperatures (475-550 °C), where the charge carriers were the extrinsic protons (H^+) with a minor or inexistent contribution of O^{2-} conduction [141]. As ionic conductivity is a thermally activated phenomenon, and the E_a at 475-550°C is ~700 eV [141], at the measured temperatures (100-200 °C), the E_a for ionic conductivity would be much greater than the one for electronic conductivity, and the latter phenomena would prevail.

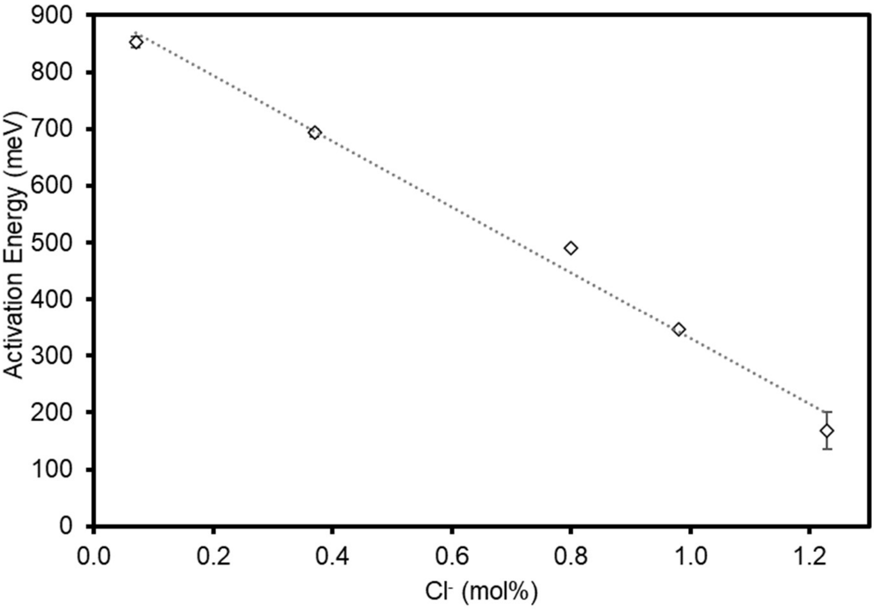

Figure 38. The estimated activation energy (E_a) for conduction of plotted against the total amount of Cl⁻-doped in ZnO nanoparticles.

Figure 39 for F⁻-doped, despite not showing a similar linear trend, also presented a reduction E_a reaching a minimum E_a of 525 meV for ZnOF-3, thus a 38% reduction compared to the undoped.

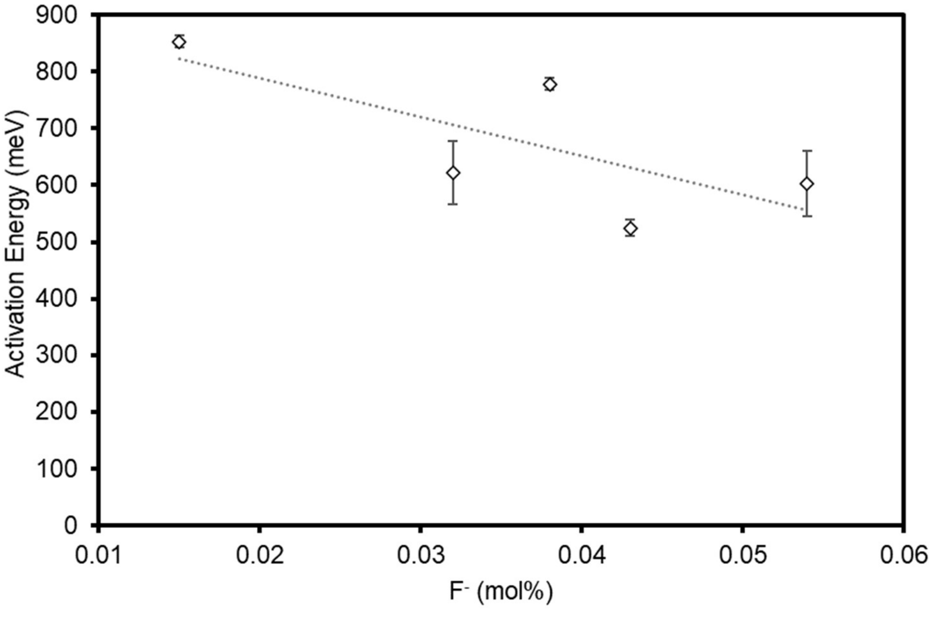

Figure 39. The estimated activation energy (E_a) for conduction of plotted against the total amount of F⁻-doped in ZnO nanoparticles.

5.2.3 Impedance analysis of the second batch (#2)

With this second batch, we intended to investigate the effect of lixiviation on the electrical conductivity.

Figure 40 shows the IS diagrams of the nanopower pressed pellets with similar relative density (46 to 50 vol.%). Table 9 lists the total electrical conductivity at 150°C extracted from IS data, defined as the low-frequency end of the IS diagram intercept with the real axis. It is observed in Figure 40 that Cl^{-}-doping promoted a two-orders of magnitude reduction of total electrical resistivity from ZnO-0 to ZnOCl-3. Such a decrease in the total electrical resistivity follows the increase in both the surface and GB excess shown in Table 7. Further addition of chlorine (> 3% Cl^{-}) increases the total electrical resistivity, and the dependence on the saturation of the GB and surface is no longer observed (Table 7). In all IS diagrams, there are at least two semicircles, corresponding to different electrical contributions, are identified and can be associated with several transport phenomena such as bulk transport, space charge layers, surface ionic diffusion, blocking of charge carriers in pores, and electrode reaction [142].

Table 9. Resistance obtained from impedance tests of #2 Cl^{-} ZnO pellets at 150°C and the calculated electrical conductivity. The dimension of the pellets and their porosity.

Sample	R (Ω)	σ (150°C) ($\Omega^{-1}\cdot cm^{-1}$)	h_p (mm)	A_Φ (mm^2)	Porosity (vol%)
ZnO-0	7.2×10^5	4.14×10^{-6}	3.39 ± 0.00	100.87 ± 0.05	49.0 ± 0.6
ZnOCl-1	4.6×10^4	6.11×10^{-5}	3.56 ± 0.01	100.79 ± 0.17	49.9 ± 1.3
ZnOCl-3	4.3×10^3	6.73×10^{-4}	3.51 ± 0.01	100.95 ± 0.43	48.8 ± 2.4
ZnOCl-6	1.3×10^4	2.22×10^{-4}	3.48 ± 0.02	101.14 ± 0.08	49.6 ± 2.4
ZnO-0 1LX	1.9×10^6	1.65×10^{-6}	3.30 ± 0.01	100.76 ± 0.03	48.8 ± 1.8
ZnOCl-1 1LX	3.0×10^5	9.68×10^{-6}	3.44 ± 0.00	100.64 ± 0.05	48.2 ± 0.7
ZnOCl-3 1LX	1.4×10^5	2.22×10^{-5}	3.31 ± 0.01	100.44 ± 0.05	47.4 ± 2.0
ZnOCl-6 1LX	4.9×10^4	6.11×10^{-5}	3.34 ± 0.01	100.65 ± 0.27	47.8 ± 1.6
ZnOCl-1 5LX	1.6×10^6	1.97×10^{-6}	3.21 ± 0.01	100.35 ± 0.07	46.3 ± 1.8
ZnOCl-6 5LX	2.6×10^5	1.16×10^{-5}	3.30 ± 0.01	100.10 ± 0.24	47.3 ± 1.7

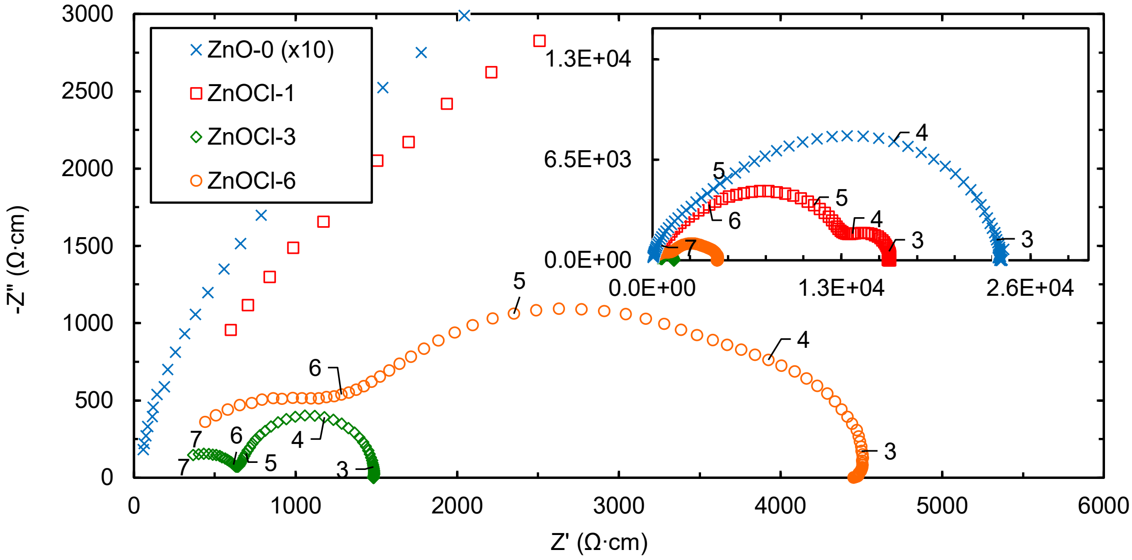

Figure 40. Impedance diagrams of Cl⁻-doped pristine ZnO pellets measured at 150 °C. Numbers indicate the logarithm of the measuring frequency. Emphasizing the comparative scale difference, only ZnO-0 needed a scale reduction (divided by 10) to be compared to ZnOCl-1 and others.

A comparison between the IS data of samples with different Cl⁻ additions and lixiviation steps provided useful insights to elucidate the role played by surface segregation, as shown in Figure 41. The IS data of lixiviated (1LX) samples showed similar behavior as the pristine samples but with a significant decrease in the electrical resistivity with chlorine doping. A remarkable direct correlation of higher Cl⁻ the higher the electrical conductivity. The lixiviation one step decreased the total electrical conductivity as compared to pristine powders. However, the total electrical conductivity of the doped samples, after the lixiviation, continues to be much greater than the undoped ZnO-0 1LX. The IS data could indicate two main features of the transport properties of ZnO upon Cl⁻ doping. First, the surface-segregated Cl⁻ ions are highly mobile and possibly contribute to electrical transport by *ionic* conduction, while also enhancing the *electrical* conductivity by increasing the electron density in the depletion layer reducing the GB potential barrier similar to gas adsorption on gas sensors [49]. Secondly, the Cl⁻ segregation at the GB modifies the electrical double layer, increasing the electronic conductivity, similar to the previously reported data [48]. In terms of these contributions, as shown in Figure 41, the higher Cl⁻ samples exhibit a drastic reduction in the low-frequency contribution. ZnOCl-3 1LX and ZnOCl-6 1LX have the same Cl⁻ excess at the surface and very similar high-frequency contributions; however, the latter sample has roughly twice the Cl⁻ excess in the GB, reflecting in a smaller low-frequency contribution. Therefore, we can associate the low-frequency semicircle with the GB electronic resistivity.

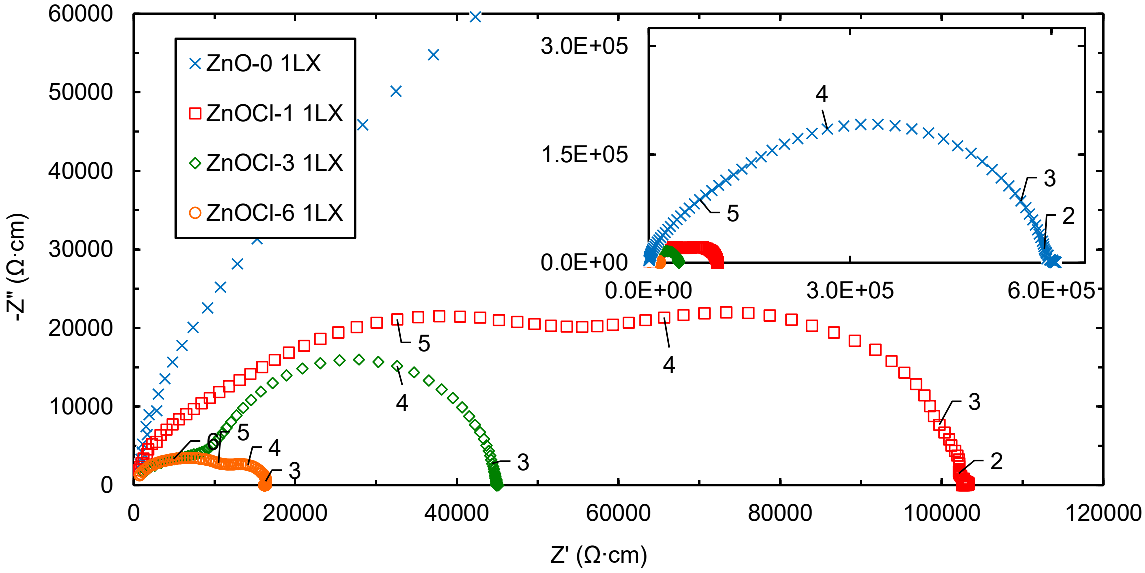

Figure 41. Impedance diagrams of Cl⁻-doped 1LX ZnO pellet measured at 150 °C. Numbers indicate the logarithm of the frequency.

Figure 42 shows the role of Cl⁻ interface excesses on the total electric conductivity. The higher amount of retained Cl⁻ after the lixiviation caused a higher conductivity. The manner the conductivity increases with the total Cl⁻ is a combination of interface excess contributions. At low Cl⁻ levels, surface excess seems to hold conductivity against a steep increase trend of GB excess, but in samples with higher Cl⁻ amounts, where surface excess is not changed with further doping, it is the GB excess that controls the increase in conductivity.

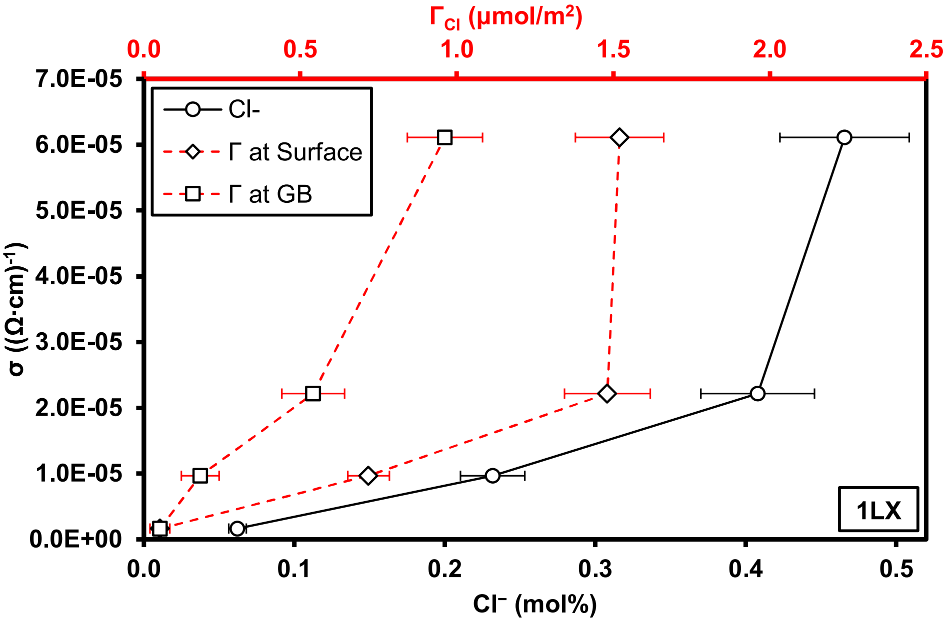

Figure 42. The amount of Cl⁻-doped 1LX ZnO and interface excesses plotted against the electrical conductivity.

The extensive lixiviation of the powders (5LX) showed a similar trend (Figure 43 and Table 9), where the total electrical conductivity is reduced with respect to the once lixiviation and the pristine powders. However, the residual GB-segregated Cl⁻ (Γ_{Cl}^{GB}), comparing both 5LX samples, seems to play a crucial role in the electrical structure of the depletion layer, reducing the electrical barrier in the GB and increasing the total electrical conductivity.

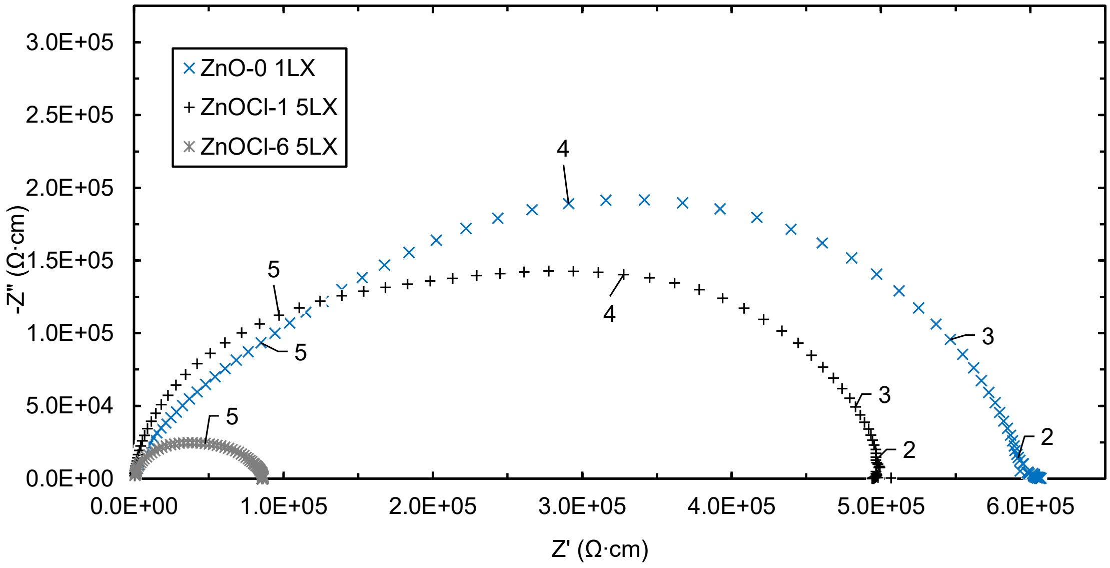

Figure 43. Impedance diagrams of Cl⁻-doped 5LX ZnO pellets at 150 °C. Numbers indicate the logarithm of the frequency.

In the case of F⁻-doped ZnO, Table 10 lists the raw resistance defined as the low-frequency end of the IS diagram intercept with real axis, all pellets parameters, and total electrical conductivity at 150°C extracted from IS data. Figure 44 shows the IS diagrams of the pristine nanopower pressed pellets with similar relative density (48 to 51 vol.%). Differently from #1, on the #2 F⁻-doped ZnO, all samples presented closer total electrical resistivity compared to the undoped (ZnO-0), even with two of them with higher resistivity (ZnOF-1 and ZnOF-7). This could be due to the relatively low GB excess of #2 when compared with #1 (Table 7). No clear correlation between GB excess, surface excess, or the ratio of excesses justified the order of resistivity obtained in Figure 44.

Table 10. Resistance obtained from impedance tests of #2 F⁻-doped ZnO pellets at 150°C and the calculated electrical conductivity. The dimension of the pellets and their porosity.

Sample	R (Ω)	σ (150°C) ($\Omega^{-1}\cdot cm^{-1}$)	h_p (mm)	A_Φ (mm^2)	Porosity (vol%)
ZnO-0	7.2×10^5	4.14×10^{-6}	3.39 ± 0.00	100.87 ± 0.05	49.0 ± 0.6
ZnOF-1	8.4×10^5	3.65×10^{-6}	3.29 ± 0.00	100.81 ± 0.37	48.4 ± 1.1
ZnOF-3	2.2×10^5	1.36×10^{-5}	3.44 ± 0.00	100.93 ± 0.20	49.3 ± 0.8
ZnOF-5	4.9×10^5	5.86×10^{-6}	3.53 ± 0.01	100.77 ± 0.11	51.1 ± 1.2
ZnOF-7	9.1×10^5	3.11×10^{-6}	3.59 ± 0.00	100.93 ± 0.04	50.0 ± 0.7
ZnO-0 1LX	1.9×10^6	1.65×10^{-6}	3.30 ± 0.01	100.76 ± 0.03	48.8 ± 1.8
ZnOF-1 1LX	5.9×10^5	5.19×10^{-6}	3.32 ± 0.00	100.95 ± 0.46	48.4 ± 1.6
ZnOF-3 1LX	3.8×10^4	7.69×10^{-5}	3.44 ± 0.00	101.18 ± 0.66	48.5 ± 2.2
ZnOF-5 1LX	1.4×10^5	2.10×10^{-5}	3.34 ± 0.01	101.18 ± 0.66	48.3 ± 3.0
ZnOF-7 1LX	8.9×10^4	3.34×10^{-5}	3.40 ± 0.01	100.79 ± 0.02	48.2 ± 1.2

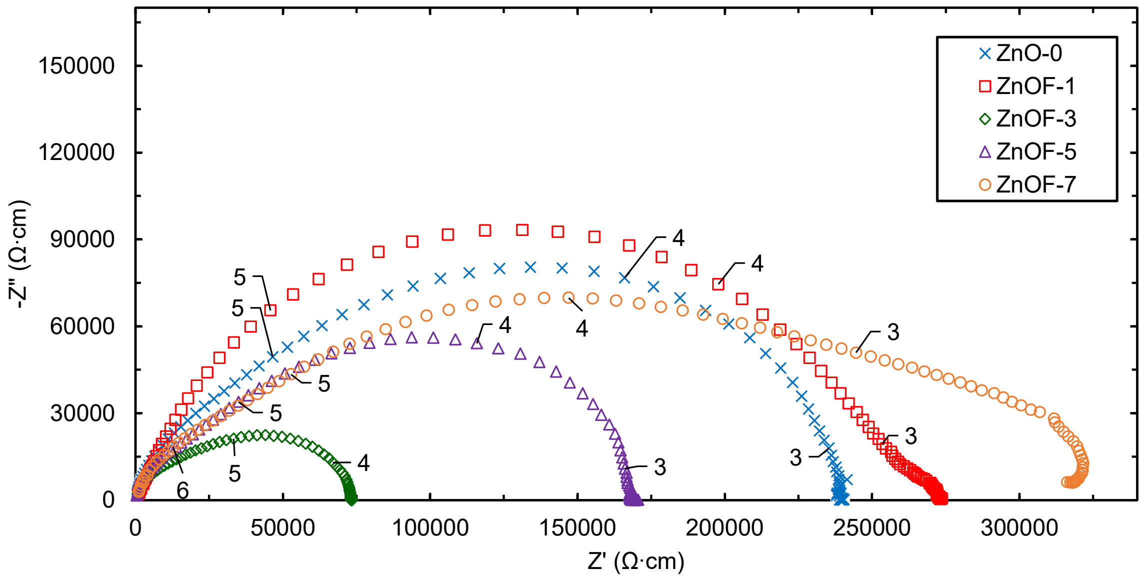

Figure 44. Impedance diagrams of F⁻-doped pristine ZnO pellets measured at 150 °C. Numbers indicate the logarithm of the measuring frequency.

The IS data of a single lixiviation step on F⁻-doped ZnO is presented in Figure 45, highlighting that the removal of F⁻ from the surface resulted in a significant decrease in electrical resistivity. All 1LX F⁻-doped ZnO presented expressively lower resistivity than the ZnO-0. Also, for these lixiviated samples, no clear correlation of GB excess, surface excess, or the ratio of excesses explains the order of resistivity obtained in Figure 45. The greatest resistivity reduction with lixiviation was for ZnOF-7 1LX, where low-frequency resistivity contribution, <10^3 Hz, is inexistent. Relating to Cl⁻ results, we can infer that the lixiviation on F⁻-doped ZnO also removed ionic conductivity. The F⁻ lixiviation drastic drop in resistivity is due to the higher electronegativity of F⁻ compared to O^{2-}, differently than Cl⁻, F⁻ at the surface would strongly attract electrons to the surface, reducing the electron density on the depletion layer, which increases the potential barrier height at the GB.

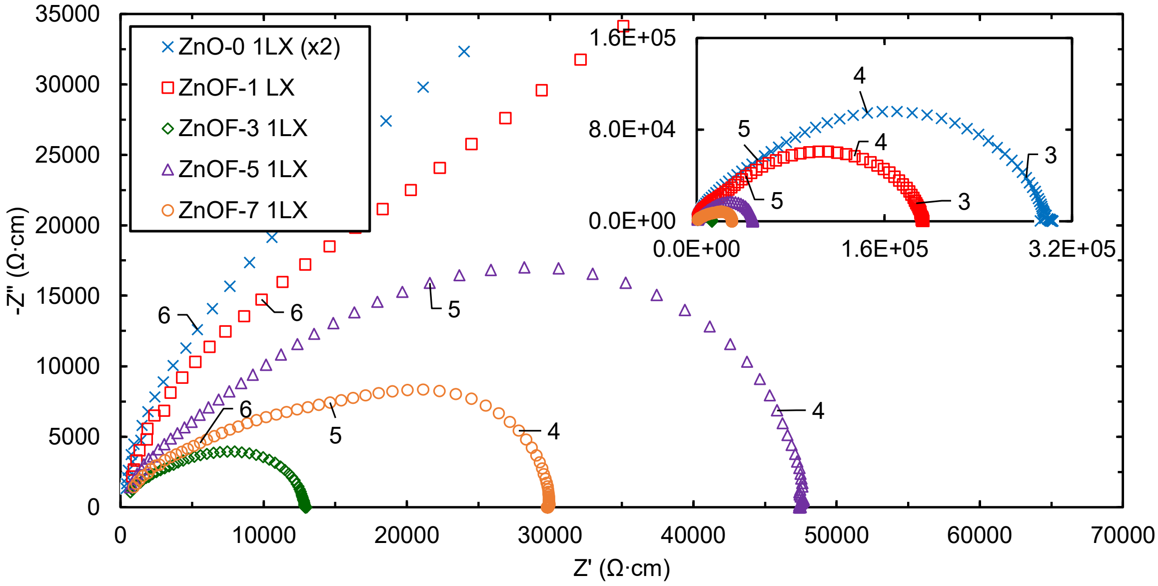

Figure 45. Impedance diagrams of F⁻-doped 1LX ZnO pellets measured at 150 °C. Numbers indicate the logarithm of the measuring frequency. Emphasizing the comparative scale difference, only ZnO-0 needed a scale reduction (divided by 2) to be compared to ZnOF-1 and others.

5.3 Photocatalytic reactivity

The electrical transport properties combined with the observed anions surface excess could give some insights into the photocatalytic behavior of doped ZnO. Previous works have shown that soluble Cl^- can inhibit photocatalytic reactions [107-109]. In this case, surface segregated Cl^- on ZnO nanopowders are susceptible to solubilizing in water during photocatalysis and cause a significant interference of the photocatalysis reaction.

However, the electric conductivity is affected by doping ions and can be modulated depending on where it is segregated, as discussed previously. The increase of the electrical conductivity promoted by Cl^- segregation at the GB can result in an increase in the mean free path of the photogenerated charge carriers (e^- and h^+) and extend their lifetimes, which are essential for the degradation of APAP [110]. Both contributions are expected to change the efficiency of photocatalytic performance.

Acetaminophen (APAP) was selected as a tracer to evaluate the effects of doping and lixiviation on the photocatalytic performance of ZnO. Figure 46 shows the degradation profile of APAP after reaction with the pristine Cl^--doped ZnO samples. The results are normalized by the surface area of the samples. The efficiency of the photocatalytic reaction, measured at 180 min of exposure to UV irradiation, increases from ZnO-0 to ZnOCl-1, but decreases substantially for higher dopant concentrations. As presented in Table 7, the surface and GB segregation increase with the total Cl^- concentration, but at low concentrations, the increase in electrical conductivity seems predominant against the deleterious effects of soluble Cl^- from ZnO surfaces. On the other hand, the high amount of soluble Cl^- from the surfaces of the ZnOCl-6 sample makes this sample the least effective of the series.

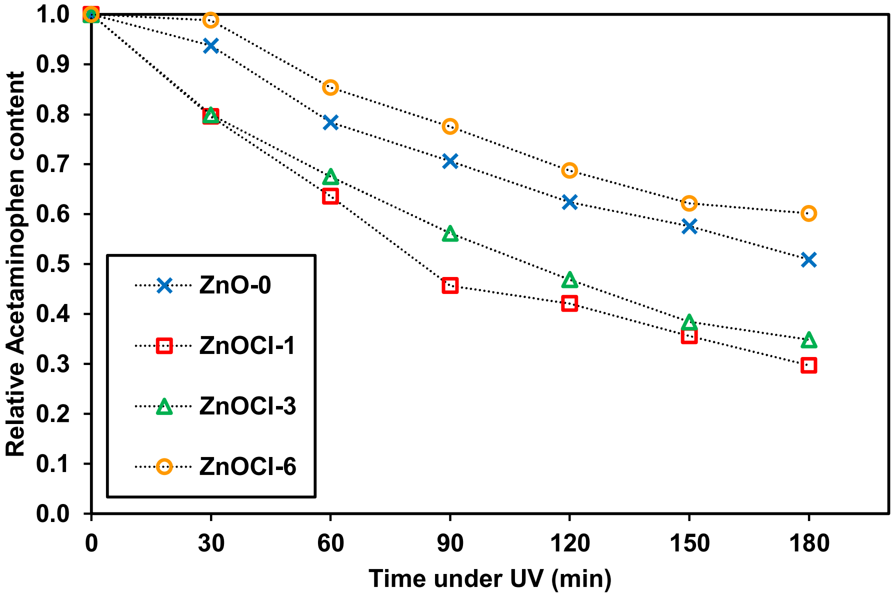

Figure 46. APAP photodegradation of pristine Cl^--doped ZnO, upon irradiation of 4.1 mW/cm^2 of monochromatic UV-A light (370 nm).

New photocatalysis essays were performed using the lixiviated samples to demonstrate that the balance between the GB-segregated Cl^- and the elimination of the soluble surface segregated Cl^- can improve catalysis by promoting a more efficient charge-carrier transport in the absence of detrimental surface-segregated species. Figure 47 presents the APAP photodegradation results that show a modification in the photocatalytic efficiency where the most efficient sample contains the greatest amount of Cl^- segregated at the GB (ZnOCl-6 1LX) and, consequently, the highest electrical conductivity. The combined results of Figure 46 and 47 confirm that controlled Cl^- segregation, without the deleterious effects of surface-segregated soluble Cl^-, at the nano-ZnO interfaces plays a crucial role in photocatalytic processes. This result reinforces the importance of the often-neglected charge-carrier transport properties to design efficient catalysts. From the start of the UV illumination, we perceive two different degradation rates per area (k_{area}), calculated via Equation 23, where C and C_0 are the current and initial APAP concentration in mol/l, *t* is time in minutes, and *S* is the surface area of the sample in m^2. While samples ZnO-0 LX, ZnOCl-1 LX and ZnOCl-3 LX presented k_{area} of 7 - 8.3 x 10^{-2} min^{-1} m^{-2}, the ZnOCl-6 LX exhibited a k_{area} one order of magnitude greater between 1.3 x 10^{-1} min^{-1} m^{-2}.

$$k_{area} = \frac{-\ln\left(\frac{C}{C_0}\right)}{t\ S} \qquad (23)$$

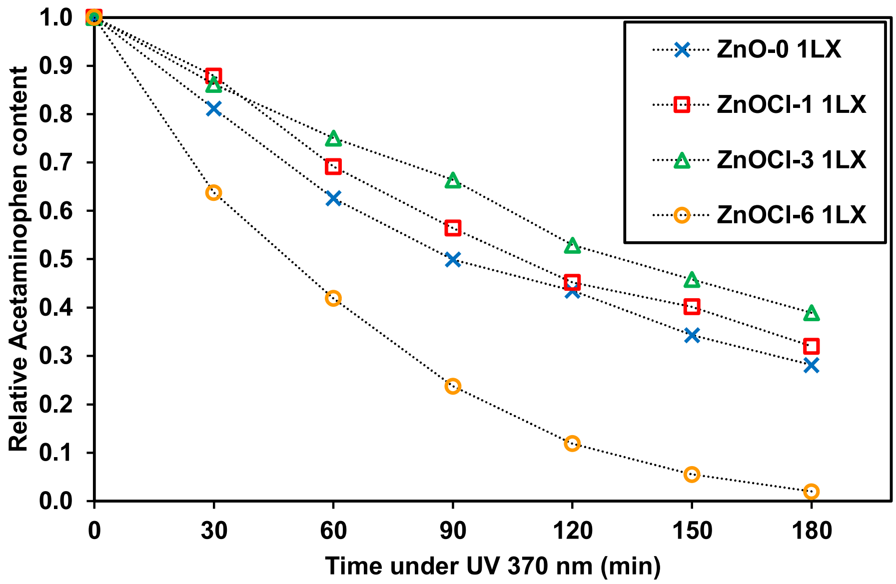

Figure 47. APAP photodegradation of 1LX Cl^--doped ZnO, upon irradiation of 4.1 mW/cm^2 of monochromatic UV-A light (370 nm).

In the case of F^--doped ZnO, Figure 48 shows the degradation profile of APAP after reaction with the pristine F^--doped ZnO samples. The results are normalized by the surface area of the samples. After 180 min of UV illumination, the efficiency of the photocatalytic reaction with F^--doping decreased compared to the undoped ZnO-0, except for ZnOF-3. This sample, which achieved the highest electrical conductivity, is the only one with an improvement in photodegradation of APAP. In the other samples, any possible deleterious effect of F^- on the surface surpassed any increase in electrical conductivity, which are minor for pristine F^--doped samples, thus presenting a lower photodegradation of APAP. Figure 49 shows that as F^- is removed from the surface in one lixiviation and electrical conductivity increases, all F^--doped samples perform better than the ZnO-0. In between lixiviated F⁻ and Cl⁻-doped, although with similar electrical conductivity, the latter achieved a slightly better photodegradation performance.

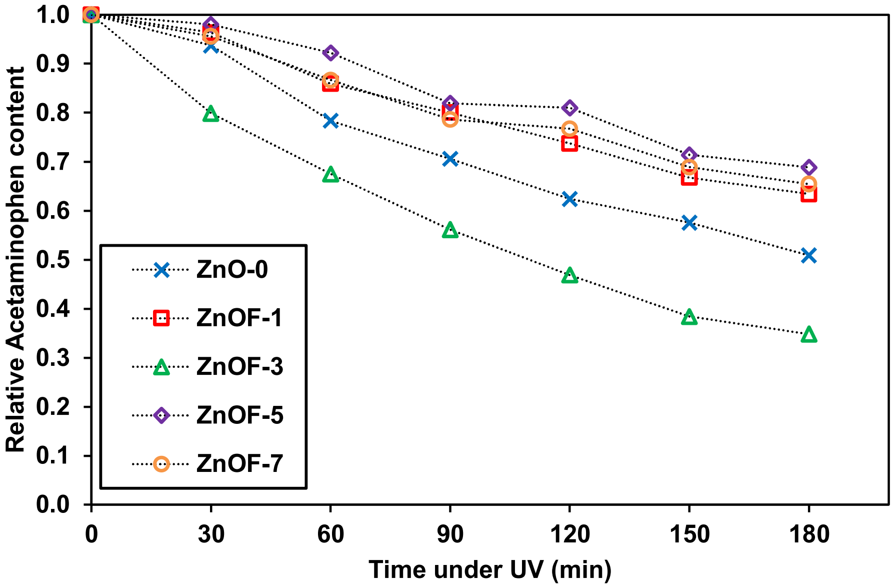

Figure 48. APAP photodegradation of pristine F⁻-doped ZnO upon irradiation of 4.1 mW/cm^2 of monochromatic UV-A light (370 nm).

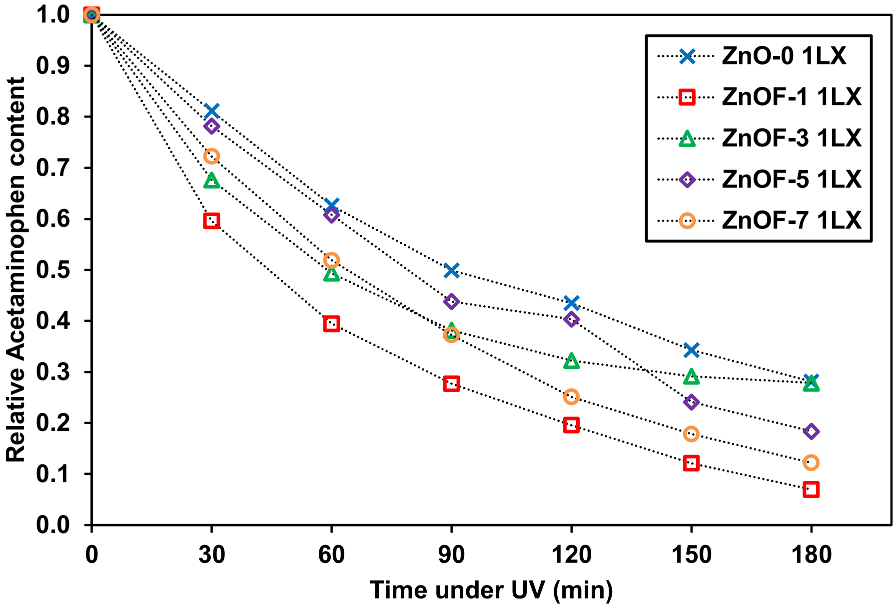

Figure 49. APAP photodegradation of 1LX F⁻-doped ZnO upon irradiation of 4.1 mW/cm^2 of monochromatic UV-A light (370 nm).

5.4 Surface adsorption

5.4.1 DRIFT

DRIFT analysis of the #1 pristine Cl⁻-doped ZnO is shown in Figure 50. All samples showed characteristic bands of H_2O, CO_2, and some CH compounds. As the Cl⁻ amount increases, less carbonate is adsorbed on the surface, and distinct hydroxyl bound to metals with the two distinct bands at 3493 cm^{-1} and 3446 cm^{-1} are observed, characteristic of ZnO prepared from ZnCl precursors [143]. Another study assigns the band 3498 cm^{-1} as a stretching OH vibration of a reversible strong dissociative adsorption of H on a surface O site [144]. While the band 3448 cm^{-1} as OH (or O-H···O) formed by water adsorption on defect sites, without ruling out the possibility of this being related to OH adsorbed at the step edges on the Zn-ZnO surface [144]. Such defects could be caused by Cl⁻ surface segregation. The binary signal at 2360-2320 cm^{-1} is related to CO_2 gas adsorption, as O=C=O-M bond to the metal perpendicularly linear to the surface. The broad band ranging 1430-1640 cm^{-1} is due to a mix of carbonates where the surface oxygen is bonded to the carbon in CO_2 adsorbed, overlapping with the water band around 1600 cm^{-1}. The signals at 2926 cm^{-1} and 2848 cm^{-1} are related to symmetric and asymmetric stretching vibrations of CH_3 and CH_2 groups [145] being less perceived for the ZnOCl-6 sample than for lower Cl⁻ dosages. Overall, the most distinctive feature is how high Cl⁻ content, and consequently higher ${\Gamma_{Cl}}^{S}$, harms CO_2 adsorption at the surface.

The DRIFT analysis of the #1 pristine F⁻-doped ZnO (Figure 51) presents the same adsorbed groups observed in Cl⁻-doped samples, except the distinct Zn-OH bands at 3493 cm^{-1} and 3446 cm^{-1}. F⁻-doped samples, in general, present less CO_2 adsorbed than undoped ZnO-0, according to the reduced intensity of the band 1430-1640 cm^{-1}.

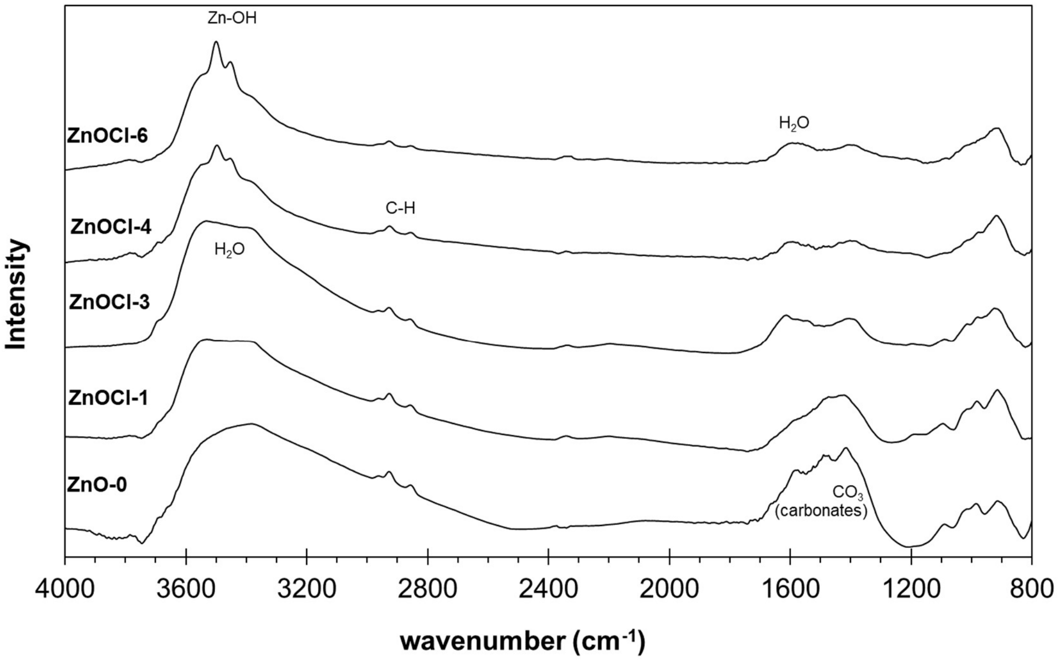

Figure 50. DRIFT of Cl⁻-doped ZnO showing compounds adsorbed at the surface of the powder samples.

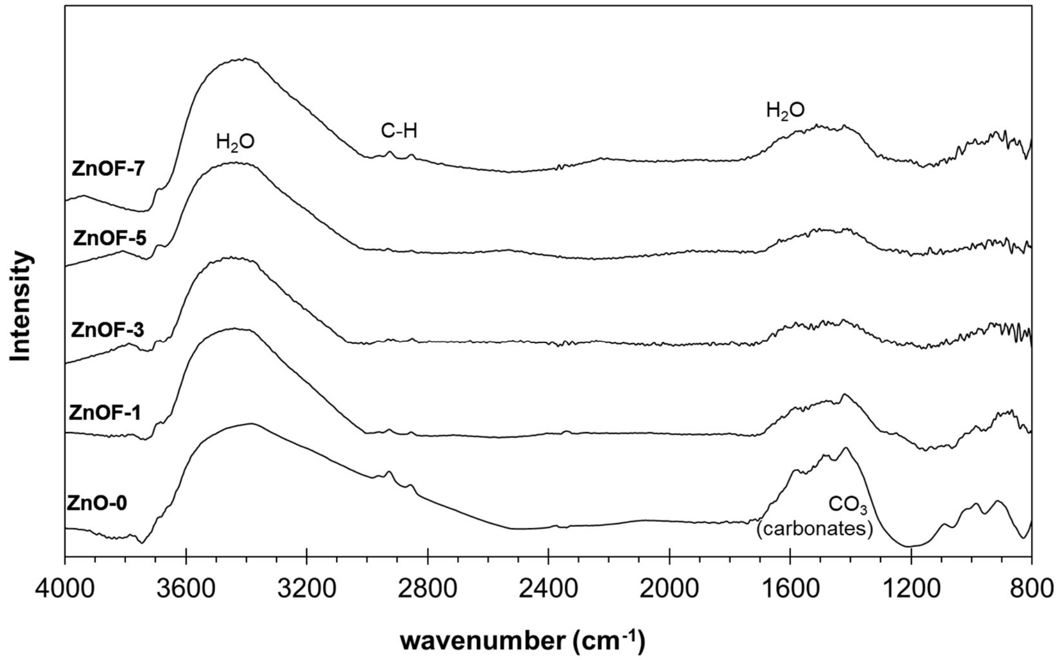

Figure 51. DRIFT of F⁻-doped ZnO showing compounds adsorbed at the surface of the powder samples.

5.4.2 CO_2 and H_2O adsorption and co-adsorption

Figure 52 shows the adsorption of CO_2 on the surface of the undoped ZnO-0 and the ZnOCl-3, both #1 pristine samples. The ZnO-0 surface has adsorption more than twice larger than the Cl^--doped sample. The enthalpy of adsorption of CO_2 on the ZnO-0 and ZnOCl-3 are −53.18 kJ/mol and −12.19 kJ/mol, respectively. The surface, almost free of Cl^-, ZnO-0, has a higher chemical affinity for CO_2, in agreement with the DRIFT (Figure 50).

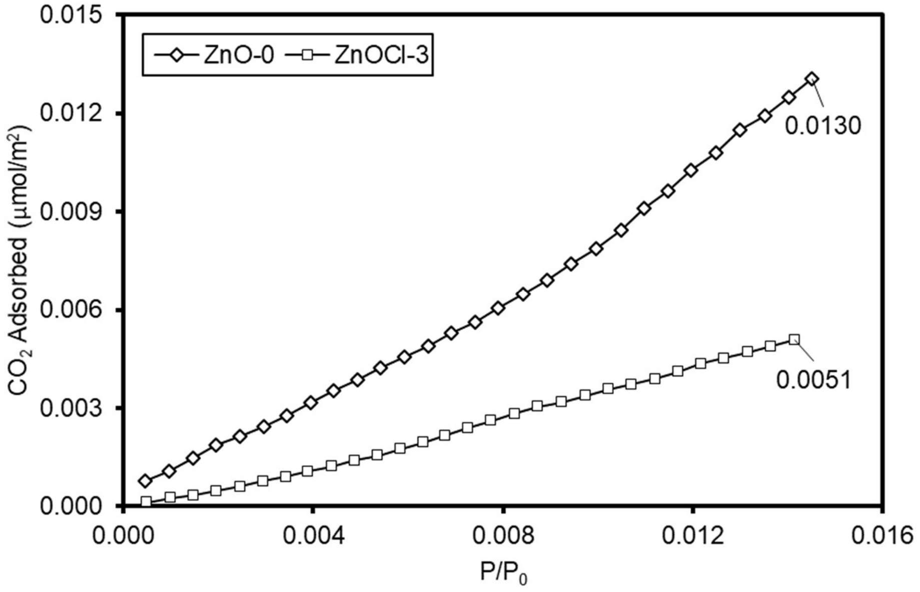

Figure 52. CO_2 adsorption measurement on the surface of ZnO-0 and ZnOCl-3.

CO_2 and H_2O adsorption affinity are desirable characteristics for photocatalysts used in artificial photosynthesis since these are the reaction precursors, and the reaction takes place at the catalyst surface [123]. Despite the remarkable increase in conductivity reached with Cl^--doping, CO_2 adsorption decrease may harm the performance of ZnO as a photocatalyst for AP. A straightforward solution is to perform the same selective lixiviation used before to remove Cl^- and F^- from the surface. That way, as surface-located halogens that inhibit the CO_2 adsorption are eliminated while the imprisoned in the GB enhance electronic conductivity.

5.5 Interface energy

5.5.1 Water adsorption microcalorimetry

Figure 53 presents the adsorption isotherm of water vapor on the pretreated surface of Cl^--doped ZnO, #2 pristine samples. The pattern between all samples is at a similar level of values. Although ZnOCl-1 and ZnOCl-6 showed the most exothermic first adsorption point, their following data appeared closer to the other samples. At the saturation, all samples tended to stabilize at −44 kJ/mol, the enthalpy of water condensation. Figure 54 shows the adsorption for the pretreated surface of F^--doped ZnO, #2 pristine, results appeared even more alike and with less dispersion of data. Unfortunately, higher F^--doped surfaces could not be measured due to the hydrophobic nature of these surfaces. The step at 4 H_2O/nm^2, shown for the undoped and F^--doped ZnO adsorption isotherms can be attributed to the replacement of CO_2 by H_2O. Based on the data presented in Figures 53 and 54, it was possible to calculate the surface energy of each sample; these values are presented in Table 11, which also recalls the total amount of dopant and the dopant surface excess. Within the deviation of the error, both Cl^- and F^--doping did not change the surface energy of ZnO. This agrees with no significant change in crystallite size, as well as interface measured and calculated areas. Therefore, with these two halogens (Cl^- and F^-) in ZnO, anionic doping has proven not to alter the surface energy, contrary to the cationic doping [10, 27, 77-87, 131].

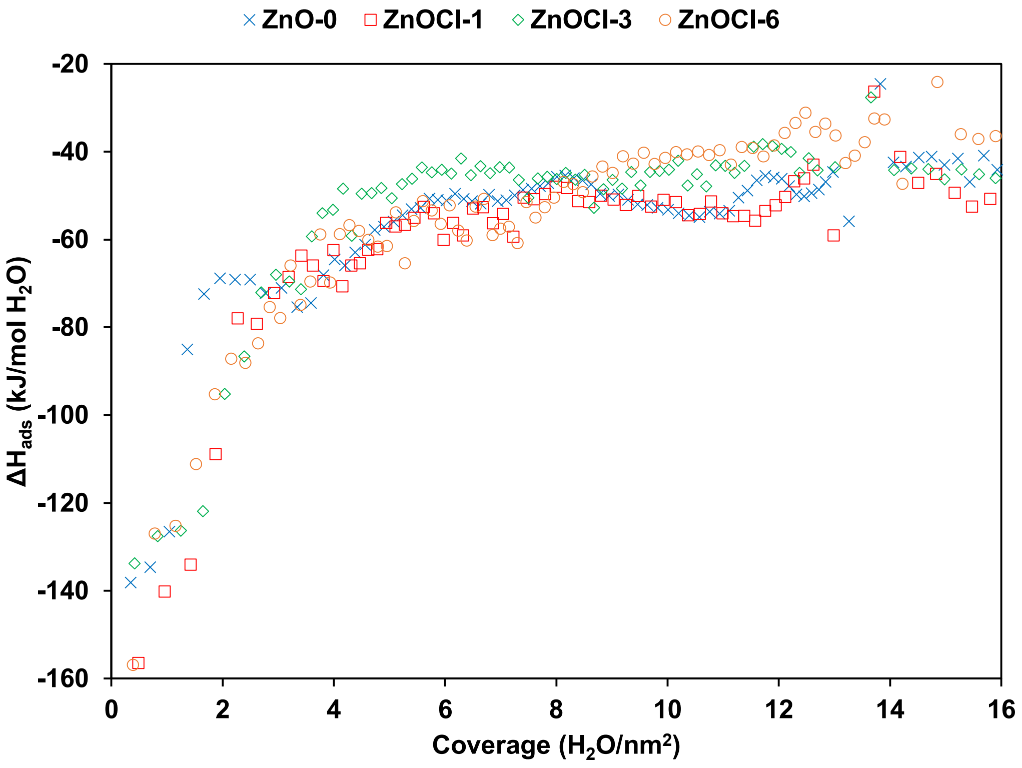

Figure 53. Differential heat of water adsorption as a function of water coverage during water vapor adsorption isotherm of on Cl⁻-doped ZnO powder.

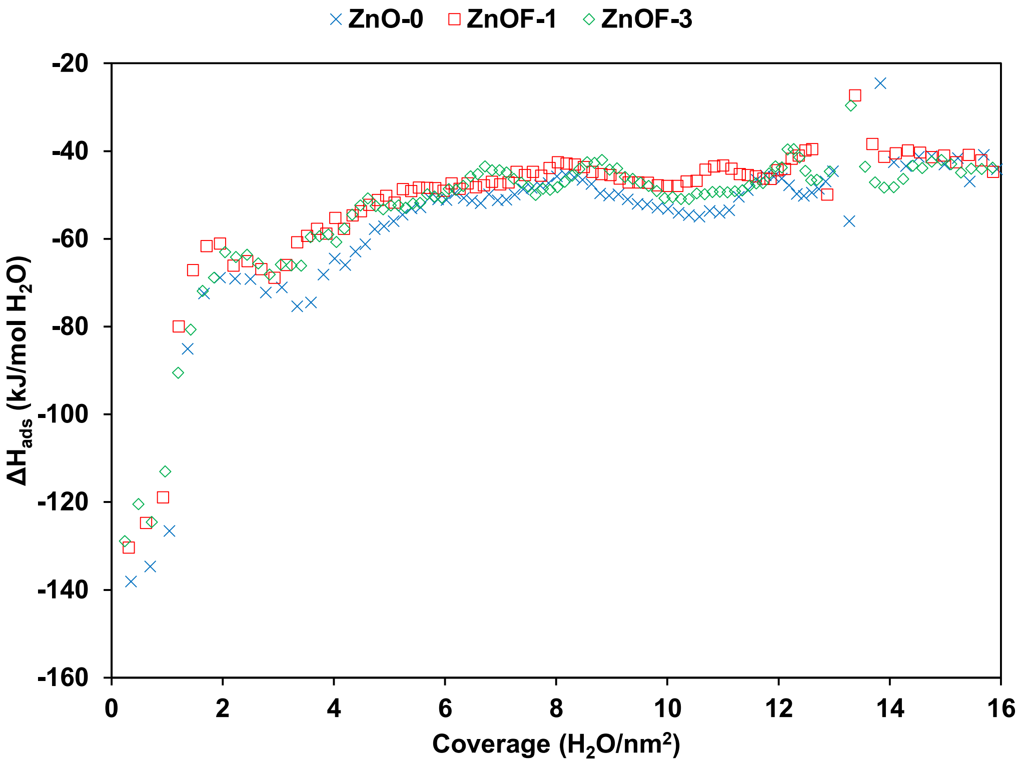

Figure 54. Differential heat of water adsorption as a function of water coverage during water vapor adsorption isotherm of on F⁻-doped ZnO powder. Samples with higher F⁻ at the surface demonstrated a high hydrophobic behavior, making it impossible to perform these adsorption measurements.

Table 11. Surface energy of #2 Cl$^-$ and F$^-$-doped ZnO and the undoped sample. Recalling for comparison the total dopant and its excess on the surface. Due to F$^-$ relative lower content, three decimal places are shown to ensure at least two significant figures.

Sample	Surface Energy (J/m^2)	Cl$^-$ (mol%)	Γ_{Cl}^{S} (μmol/m^2)
ZnO-0	0.72 ± 0.08	0.07 ± 0.01	0.15 ± 0.01
ZnOCl-1	0.79 ± 0.10	0.43 ± 0.04	2.14 ± 0.19
ZnOCl-3	0.74 ± 0.07	1.03 ± 0.09	4.63 ± 0.41
ZnOCl-6	0.82 ± 0.09	1.25 ± 0.11	6.32 ± 0.55
Sample	Surface Energy (J/m^2)	F$^-$ (mol%)	Γ_{F}^{S} (μmol/m^2)
ZnO-0	0.72 ± 0.08	0.012 ± 0.001	0.031 ± 0.003
ZnOF-1	0.66 ± 0.06	0.011 ± 0.001	0.021 ± 0.002
ZnOF-3	0.68 ± 0.06	0.013 ± 0.001	0.059 ± 0.005
ZnOF-5	---	0.034 ± 0.003	0.150 ± 0.014
ZnOF-7	---	0.033 ± 0.003	0.188 ± 0.017

6 CONCLUSIONS

Two batches of Cl$^-$ and F$^-$-doped ZnO nanoparticles were synthesized by the polymeric precursor method, characterized, and analyzed, leading us to the following conclusions:

- Single-phased wurtzite was obtained in the form of ZnO nanoparticles with a crystallite size ranging from 22 nm to 30 nm and SSA of 12 m^2/g to 18 m^2/g.
- Most of the added Cl$^-$ and F$^-$ are lost during pyrolysis, yet the retained Cl$^-$ is ten times greater than retained F$^-$.
- Selective lixiviation tests and total dissolution of samples have proven that dopants are mainly located at the interfaces. Cl$^-$ segregated more towards the surface instead of the grain boundary. F$^-$, however, demonstrated on #1 a preference for the grain boundary rather than the surface, but on #2, surface segregation reached values twice greater than the grain boundary.
- Interface excess or total dopant did not coherently influence crystallite size. For instance, in the #1 Cl$^-$-doped, the smaller crystallites and higher SSA were achieved with intermediate doping #1ZnOCl-3 (0.80 mol%) and

#1ZnOCl-4 (0.98 mol%). On the second batch, #2ZnOCl-3 (1.03 mol%) presented the smallest crystallite size of the set.

- For #1 F^--doped, the smaller crystallites and higher SSA was attained for the highest doping and surface excesses but not related to interface excesses or total dopant. On #2, no apparent interface excesses or total dopant trend was related to crystallite size.
- Both Cl^- and F^--doping improved the electrical conductivity of the pressed pellet in comparison with the undoped sample. The most effective in increasing the electrical conductivity 1857-times fold was on #1 Cl^--doped, while #1 F^--doped showed a maximum enhancement of 32-times fold.
- On #1, Cl^- excess in the grain boundary, which corresponds to total Cl^-, leads to a gradual increase in the electrical conductivity. A potential barrier height plotted versus Cl^- concentration showed a height reduction similar to the reduction of activation energy, both with remarkable correlation, proving that the excess of these ions effectively reduces the potential barrier. Thus, promoting intergranular electronic conductivity.
- On #1, F^- excess in the grain boundary also reduced the activation energy for conductivity compared to the undoped sample. Thus, possibly reducing the grain boundary potential barrier. However, F^- excess on the surface seems to affect the conductivity more than the F^- excess in the grain boundary.
- The #2 did not enhance electrical conductivity as much as #1, although a similar trend was observed. A significant reduction in the total electrical resistivity with increasing Cl^- content. The selective lixiviation of dopants allowed the unraveling of a deeper understanding of the occurring electrically conductive phenomena. An increase in overall electrical conductivity is attributed to surface-segregated Cl^-, which possibly combines ionic conduction and increased electronic conduction, reducing the potential barrier for electronic conduction promoted by GB-segregated Cl^-. The experimental data showed that lixiviation decreased the overall electric conductivity as it gradually reduced the conductivity contribution of Cl^- at the surface, to the point that the electronic conduction through the GB becomes the controlling mechanism.
- The electrical properties were reflected on the photocatalytic properties, where the highest Cl^--doped lixiviated samples with the highest $\Gamma_{Cl}^{GB}/\Gamma_{Cl}^{S}$ achieved the best conversion for APAP photocatalysis. Such an effect is

attributed to (i) a high GB electronic conductivity, which hindered e^-/h^+ recombination, allowing such charged species to participate in redox reactions at the surface; and (ii) a relatively clearer surface (lower Cl^- concentration), which did not solubilize to the solution.

- Cl^- and F^--doping do not change the surface energy of ZnO nanoparticles. However, Cl^- and F^--doped surfaces are less favored than undoped ZnO for the adsorption of CO_2.

Therefore, doping nano-ZnO with Cl^- and F^-, mainly Cl^-, and later selectively lixiviating the dopant with water demonstrated to be a relevant path to obtain an improved photocatalytic material for photodegradation of pharmaceuticals and potentially improve artificial photosynthesis efficiency.

7 REFERENCES

1. CIAMICIAN, G., The Photochemistry of the Future. Science (New York, N.Y.), **36**(926): p. 385-394, 1912.
2. INOUE, T., et al., Photoelectrocatalytic reduction of carbon dioxide in aqueous suspensions of semiconductor powders. Nature, **277**: p. 637-638, 1979.
3. HE, Y., et al., High-efficiency conversion of CO2 to fuel over ZnO/g-C3N4 photocatalyst. Applied Catalysis B: Environmental, **168-169**: p. 1-8, 2015.
4. OLA, O. and M. M. MAROTO-VALER, Transition metal oxide based TiO2 nanoparticles for visible light induced CO2 photoreduction. Applied Catalysis A: General, **502**: p. 114-121, 2015.
5. WATANABE, M., Photosynthesis of methanol and methane from CO2 and H2O molecules on a ZnO surface. Surface Science, **279**(3): p. L236-L242, 1992.
6. GOUVÊA, D., S.V. USHAKOV, and A. NAVROTSKY, Energetics of CO2 and H2O Adsorption on Zinc Oxide. Langmuir, **30**(30): p. 9091-9097, 2014.
7. STRUNK, J., et al., The surface chemistry of ZnO nanoparticles applied as heterogeneous catalysts in methanol synthesis. Surface Science, **603**(10): p. 1776-1783, 2009.
8. BAIZAEE, S.M., M. ARABI, and A.R. BAHADOR, A simple, one-pot, low temperature and pressure route for the synthesis of RGO/ZnO nanocomposite and investigating its photocatalytic activity. Materials Science in Semiconductor Processing, **82**: p. 135-142, 2018.
9. SOHN, Y., W. HUANG, and F. TAGHIPOUR, Recent progress and perspectives in the photocatalytic CO2 reduction of Ti-oxide-based nanomaterials. Applied Surface Science, **396**: p. 1696-1711, 2017.
10. CASTRO, R.H.R. and D. GOUVÊA, Sintering and Nanostability: The Thermodynamic Perspective. Journal of the American Ceramic Society, **99**(4): p. 1105-1121, 2016.
11. GORDON, R.G., Criteria for Choosing Transparent Conductors. MRS Bulletin, **25**(8): p. 52-57, 2011.
12. JIAMPRASERTBOON, A., et al., Photocatalytic and electrically conductive transparent Cl-doped ZnO thin films via aerosol-assisted chemical vapour deposition. Journal of Materials Chemistry A, **6**(26): p. 12682-12692, 2018.
13. HE, J., Metal Oxide Varistors From Microstructure to Macro-Characteristics., Weinheim, Germany: Wiley-VCH Verlag GmbH & Co. KGaA, 2019. p. 1-472.
14. LONG, R., J. LIU, and O.V. PREZHDO, Unravelling the Effects of Grain Boundary and Chemical Doping on Electron–Hole Recombination in CH3NH3PbI3 Perovskite by Time-Domain Atomistic Simulation. Journal of the American Chemical Society, **138**(11): p. 3884-3890, 2016.
15. NOWOTNY, M.K., Solid state chemistry and photocatalysis of titanium dioxide : special topic volume with invited peer reviewed papers only. Stafa-Zuerich: TransTech Publ, 2010. p. 1-340.
16. BLUNDEN J., A.D.S., HARTFIELD G., State of the Climate in 2017. Bulletin of the American Meteorological Society, **99**(8): p. Si–S332, 2018.
17. ETHERIDGE, D.M., et al., Natural and anthropogenic changes in atmospheric CO₂ over the last 1000 years from air in Antarctic ice and firn. Journal of Geophysical Research, **101**: p. 4115-4128, 1996.
18. Intergovernmental Panel on Climate, C. and I. Working Group, Climate change 2001 : the scientific basis. Summary for policymakers. Cambridge; New York: Cambridge University Press, 2001.
19. Annual Mean Global Carbon Dioxide Growth Rates. [cited 2020 February 2020]; Available from: https://www.esrl.noaa.gov/gmd/ccgg/trends/gl_gr.html. 2020.

20. ZHOU, H., et al., Leaf-architectured 3D hierarchical artificial photosynthetic system of perovskite titanates towards CO_2 photoreduction into hydrocarbon fuels. Scientific reports, **3**: p. 1667-1667, 2013.
21. LIN, Z., et al., Multifunctional photocatalytic materials for energy, Duxford; Cambridge; Kidlington: Woodhead Publishing is an imprint of Elsevier, p. 1-344, 2018.
22. MEYER, T.J., Chemical Approaches to Artificial Photosynthesis. Accounts of Chemical Research, **22**(5): p. 163-170, 1989.
23. FUJISHIMA, A. and K. HONDA, Electrochemical Photolysis of Water at a Semiconductor Electrode. Nature, **238**(5358): p. 37-+,1972.
24. BRUNO, R., Artificial photosynthesis. First edition. ed. Advances in botanical research. Amsterdam: Elsevier/Academic Press is an imprint of Elsevier. xii. 2016. p. 1-340.
25. FIECHTER, S., Artificial Photosynthesis - An Inorganic Approach, in Advances in Botanical Research - Artificial photosynthesis, R. BRUNO, Editor, Elsevier/Academic Press is an imprint of Elsevier: Amsterdam. p. xii, 2016 p. 1-248.
26. KHAN, M.M., S.F. ADIL, and A. AL-MAYOUF, Metal oxides as photocatalysts. Journal of Saudi Chemical Society, **19**(5): p. 462-464, 2015.
27. DA SILVA, A.L., Et al., TiO2 Surface Engineering to Improve Nanostability: The Role of Interface Segregation. The Journal of Physical Chemistry C, **123**(8): p. 4949-4960, 2019.
28. ZHAO, Y., et al., Graphene-wrapped Pt/TiO2 photocatalysts with enhanced photogenerated charges separation and reactant adsorption for high selective photoreduction of CO2 to CH4. Applied Catalysis B: Environmental, **226**: p. 360-372, 2018.
29. WANG, L., et al., Preparation of ZnO/ZnS thin films for enhancing the photoelectrochemical performance of ZnO. Vacuum, **148**: p. 201-205, 2018.
30. DULUB, O., B. MEYER, and U. DIEBOLD, Observation of the Dynamical Change in a Water Monolayer Adsorbed on a ZnO Surface. Physical Review Letters, **95**(13): p. 136101, 2005.
31. NOEI, H., et al., Activation of Carbon Dioxide on ZnO Nanoparticles Studied by Vibrational Spectroscopy. The Journal of Physical Chemistry C, **115**(4): p. 908-914, 2011.
32. LIU, Y., et al., High Reactivity of the ZnO(0001) Polar Surface: The Role of Oxygen Adatoms. The Journal of Physical Chemistry C, **121**(29): p. 15711-15718, 2017.
33. WANG, J., B. HOKKANEN, and U. BURGHAUS, Adsorption of CO2 on pristine Zn–ZnO(0001) and defected Zn–ZnO(0001): A thermal desorption spectroscopy study. Surface Science, **577**(2): p. 158-166, 2005.
34. YE, H., et al., Structures and Mechanisms of Water Adsorption on ZnO(0001) and GaN(0001) Surface. The Journal of Physical Chemistry C, **117**(31): p. 15976-15983, 2013.
35. WÖLL, C., The chemistry and physics of zinc oxide surfaces. Progress in Surface Science, **82**(2): p. 55-120, 2007.
36. OZGUR, U., et al., A comprehensive review of ZnO materials and devices. Journal of Applied Physics, **98**(4), 2005.
37. BHUSHAN, B., et al., Handbook of Nanomaterials Properties. Heidelberg: Springer Verlag, 2014. p. 1-1463.
38. KITTEL, C., Introdução à física do estado sólido. Rio de Janeiro: Guanabara Dois, 1978. p. 1-578.
39. O. MADELUNG, U. RÖSSLER, and M. SCHULZ., Zinc oxide (ZnO) distances, ionic radii, further lattice parameters, in II-VI and I-VII Compounds; Semimagnetic Compounds, Springer Berlin Heidelberg: Berlin, Heidelberg. p. 1-4., 1999.

40. State, S. Wurtzite polyhedra. 2008 [cited 2020 February 2020]; Crystal structure of ZnS (wurtzite) with coordination polyhedra]. Available from: https://commons.wikimedia.org/wiki/File:Wurtzite_polyhedra.png.
41. American Elements Z-MITE™ Zinc Oxide Nanopowder. 2020 [cited 2020 March 2020]; Available from: http://www.matweb.com/search/DataSheet.aspx?MatGUID=1057ef602eb5464c9814987488156ea1.
42. KLINGSHIRN, C., ZnO: Material, Physics and Applications. ChemPhysChem, **8**(6): p. 782-803, 2007.
43. NICKEL, N.H., N.A.R.W.o.Z.O.a.a.M.f. Micro, and A. Optoelectronic, Zinc oxide : a material for micro- and optoelectronic applications : [proceedings of the NATO Advanced Research Workshop on Zinc Oxide as a Material for Micro- and Optoelectronic Applications, St. Petersburg, Russia, 23-25 June 2004]. Dordrecht: Springer, 2005.
44. ONG, C.B., L.Y. NG, and A.W. MOHAMMAD, A review of ZnO nanoparticles as solar photocatalysts: Synthesis, mechanisms and applications. Renewable and Sustainable Energy Reviews, **81**: p. 536-551, 2018.
45. KAJIKAWA, Y., Effects of potential barrier height and its fluctuations at grain boundaries on thermoelectric properties of polycrystalline semiconductors. Journal of Applied Physics, **114**(5): p. 053707, 2013.
46. CHOWDHURY, M.H. and M.Z. KABIR, Electrical properties of grain boundaries in polycrystalline materials under intrinsic or low doping. Journal of Physics D: Applied Physics, **44**(1): p. 015102, 2010.
47. CLARKE, D.R., Varistor Ceramics. Journal of the American Ceramic Society, **82**(3): p. 485-502, 1999.
48. FORTES, G.M., et al., Interfacial segregation in Cl−-doped nano-ZnO polycrystalline semiconductors and its effect on electrical properties. Ceramics International, 2021.
49. JI, H., W. ZENG, and Y. LI, Gas sensing mechanisms of metal oxide semiconductors: a focus review. Nanoscale, **11**(47): p. 22664-22684, 2019.
50. CHIANG, Y.-M., et al., Physical ceramics : principles for ceramic science and engineering. Chichester: Wiley, 1997. p. 1-544.
51. LEE, J., et al., Impedance spectroscopy of grain boundaries in nanophase ZnO. Journal of Materials Research, **10**(9): p. 2295-2300, 1995.
52. SIMPSON, J.C. and J.F. CORDARO, Characterization of deep levels in zinc oxide. Journal of Applied Physics, **63**(5): p. 1781-1783, 1988.
53. MINAMI, T., et al., Effect of applied external magnetic field on the relationship between the arrangement of the substrate and the resistivity of aluminium-doped ZnO thin films prepared by r.f. magnetron sputtering. Thin Solid Films, **164**: p. 275-279, 1988.
54. ALBRECHT, J.D., et al., High field electron transport properties of bulk ZnO. Journal of Applied Physics, **86**(12): p. 6864-6867, 1999.
55. VAN DE WALLE, C.G., Defect analysis and engineering in ZnO. Physica B: Condensed Matter, **308-310**: p. 899-903, 2001.
56. MOSBACKER, H.L., et al., Role of near-surface states in ohmic-Schottky conversion of Au contacts to ZnO. Applied Physics Letters, **87**(1), 2005.
57. KOHAN, A.F., et al., First-principles study of native point defects in ZnO. Physical Review B, **61**(22): p. 15019-15027, 2000.
58. CALLISTER, W.D. and D.G. RETHWISCH, Materials science and engineering : an introduction. Hoboken, NJ: John Wiley, 2009. p. 1-370.
59. BUBE, R.H., Photoelectronic properties of semiconductors. Cambridge: Univ. Press, 2004. p. 1-318.
60. RAY, B., Two to six) II-VI compounds. London: Pergamon Press. 1969. p. 1-44.
61. LI, S.S., Semiconductor physical electronics. New York: Plenum. 1993. p. 1-514.

62. ZHU, W., et al., Band gap narrowing of titanium oxide semiconductors by noncompensated anion-Cation codoping for enhanced visible-Light photoactivity. Physical Review Letters, **103**(22), 2009.
63. RABOCKAI, T., Físico-química de superfícies. Secretaria-Geral da Organização dos Estados Americanos, Programa Regional de Desenvolvimento Científico e Tecnológico, 1979. p. 1-128.
64. SORESCU, D.C., W.A. AL-SAIDI, and K.D. JORDAN, CO2 adsorption on TiO2 (101) anatase: A dispersion-corrected density functional theory study. The Journal of chemical physics, **135**(12): p. 124701, 2011.
65. DESJONQUERES, M.C. and D. SPANJIAARD, Concepts in surface physics. 2nd ed. New York: Springer-Verlag, 1998. p. 1-8.
66. PADILHA, A.F., Materiais de engenharia : microestrutra e propriedades. São Paulo (SP): HEMUS. 2007. p. 1-349.
67. SCHIEK, M., et al., Water adsorption on the hydroxylated H-(1× 1) O-ZnO (0001 [combining macron]) surface. Physical Chemistry Chemical Physics, **8**(13): p. 1505-1512, 2006.
68. GLEITER, H., Nanostructured materials: state of the art and perspectives. Nanostructured Materials, **6**(1): p. 3-14, 1995.
69. CASTRO, R.H.R., On the thermodynamic stability of nanocrystalline ceramics. Materials Letters, **96**: p. 45-56, 2013.
70. GLEITER, H., Materials with ultrafine microstructures: Retrospectives and perspectives. Nanostructured Materials, **1**(1): p. 1-19, 1992.
71. BIRRINGER, R., Nanocrystalline materials. Materials Science and Engineering: A, **117**: p. 33-43, 1989.
72. KHAN, I., K. SAEED, and I. KHAN, Nanoparticles: Properties, applications and toxicities. Arabian Journal of Chemistry, **12**(7): p. 908-931, 2019.
73. PECHINI, M.P., Method of preparing lead and alkaline titanates and niobates and coating method using the same to form a capacitor, U.S.P. Office, Editor. United States, 1967:
74. TAI, L.-W. and P.A. LESSING, Modified resin–intermediate processing of perovskite powders: Part I. Optimization of polymeric precursors. Journal of Materials Research, **7**(2): p. 502-510, 2011.
75. WEISSMÜLLER, J., Alloy effects in nanostructures. Nanostructured Materials, **3**(1): p. 261-272, 1993.
76. THANH, N.T.K., N. MACLEAN, and S. MAHIDDINE, Mechanisms of Nucleation and Growth of Nanoparticles in Solution. Chemical Reviews, **114**(15): p. 7610-7630, 2014.
77. SEARCY, A.W. and J.W. BULLARD, Thermodynamics and Kinetics of Surface Area Changes of Faceted Particles. Journal of the American Ceramic Society, **77**(9): p. 2314-2318, 1994.
78. CHIANG, Y.-M., D.P. BIRNIE, and W.D. KINGERY, Physical Ceramics: Principles for Ceramic Science and Engineering. The MIT Series in Materials Science and Engineering. USA: John Wiley & Sons, 1997. p. 1-522.
79. GOUVÊA, D., D.C.C. ROSÁRIO, and L.B. CALIMAN, Surface and grain-boundary excess of ZnO-doped SnO_2 nanopowders by the selective lixiviation method. Journal of the American Ceramic Society, 2017.
80. GOUVÊA, D. and R.H.R. CASTRO, Sintering: the role of interface energies. Applied Surface Science, **217**(1): p. 194-201, 2003.
81. GOUVÊA, D., et al., Quantification of MgO surface excess on the SnO2 nanoparticles and relationship with nanostability and growth. Applied Surface Science,. **257**(9): p. 4219-4226, 2011
82. PEREIRA, G.J., et al., Surface segregation of additives on SnO2 based powders and their relationship with macroscopic properties. Applied Surface Science, **195**(1): p. 277-283, 2002.

83. CASTRO, R.H.R., G.J. PEREIRA, and D. GOUVÊA, Surface modification of SnO2 nanoparticles containing Mg or Fe: Effects on sintering. Applied Surface Science, **253**(10): p. 4581-4585, 2007.
84. WU, L., et al., Surface Segregation on Manganese Doped Ceria Nanoparticles and Relationship with Nanostability. The Journal of Physical Chemistry C, **118**(51): p. 30187-30196, 2014.
85. CASTRO, R.H.R., Overview of Conventional Sintering, in Sintering: Mechanisms of Convention Nanodensification and Field Assisted Processes, R. Castro and K. van Benthem, Editors. Springer Berlin Heidelberg: Berlin, Heidelberg. p. 1-16, 2013.
86. KIRCHHEIM, R., Reducing grain boundary, dislocation line and vacancy formation energies by solute segregation. I. Theoretical background. Acta Materialia, **55**(15): p. 5129-5138, 2007.
87. KIRCHHEIM, R., Reducing grain boundary, dislocation line and vacancy formation energies by solute segregationII. Experimental evidence and consequences. Acta Materialia, **55**(15): p. 5139-5148, 2007.
88. LIU, K.W. and F. MÜCKLICH, Thermal stability of nano-RuAl produced by mechanical alloying. Acta Materialia, **49**(3): p. 395-403, 2001.
89. MEHTA, S.C., D.A. SMITH, and U. ERB, Study of grain growth in electrodeposited nanocrystalline nickel-1.2 wt.% phosphorus alloy. Materials Science and Engineering: A, **204**(1): p. 227-232, 1995.
90. BOYLAN, K., et al., An in-situ tem study of the thermal stability of nanocrystalline NiP. Scripta Metallurgica et Materialia, **25**(12): p. 2711-2716, 1991.
91. LIU, F. and R. KIRCHHEIM, Nano-scale grain growth inhibited by reducing grain boundary energy through solute segregation. Journal of Crystal Growth, **264**(1-3): p. 385-391, 2004.
92. YILDIZ, A., et al., Ni doping effect on electrical conductivity of ZnO nanocrystalline thin films. Journal of Materials Science: Materials in Electronics, **22**(9): p. 1473, 2011.
93. SERIN, T., et al., Electrical conduction properties of In-doped ZnO thin films. Physica Scripta, **84**: p. 065703, 2011.
94. YILDIZ, A., et al., Electrical conduction properties of Co-doped ZnO nanocrystalline thin films. Journal of Materials Science: Materials in Electronics, **23**(2): p. 425-430, 2012.
95. GONG, L., J. LU, and Z. YE, Transparent conductive Ga-doped ZnO/Cu multilayers prepared on polymer substrates at room temperature. Solar Energy Materials and Solar Cells, **95**(7): p. 1826-1830, 2011.
96. TSAY, C.-Y., et al., Effect of Sn-doped on microstructural and optical properties of ZnO thin films deposited by sol–gel method. Thin Solid Films, **517**(3): p. 1032-1036, 2008.
97. ZHANG, Y., et al., Lattice Strain Induced Remarkable Enhancement in Piezoelectric Performance of ZnO-Based Flexible Nanogenerators. ACS Applied Materials & Interfaces, **8**(2): p. 1381-1387, 2016.
98. LIU, C., et al., Improvement in the Piezoelectric Performance of a ZnO Nanogenerator by a Combination of Chemical Doping and Interfacial Modification. The Journal of Physical Chemistry C, **120**(13): p. 6971-6977, 2016.
99. WANG, F., et al., Cl-Doped ZnO Nanowires with Metallic Conductivity and Their Application for High-Performance Photoelectrochemical Electrodes. ACS Applied Materials & Interfaces, **6**(2): p. 1288-1293, 2014.
100. GAUTAM, K., et al., Role of Cl doping on the growth and relaxation dynamics of ZnO nanorods synthesized by hydrothermal method. Chemical Physics Letters, **662**: p. 196-200, 2016.
101. LIU, B., et al., Defect formation in chlorine-doped zinc oxide. Solid State Communications, **171**: p. 30-33, 2013.

102. CHIKOIDZE, E., et al., Effect of chlorine doping on electrical and optical properties of ZnO thin films. Vol. 516. 8146-8149, 2008.
103. OBA, F., et al., Energetics of native defects in ZnO. Journal of Applied Physics, **90**(2): p. 824-828, 2001.
104. BHACHU, D.S., et al., Textured Fluorine-Doped Tin Dioxide Films formed by Chemical Vapour Deposition. Chemistry – A European Journal, **17**(41): p. 11613-11621, 2011.
105. PONJA, S.D., et al., Transparent conductive aluminium and fluorine co-doped zinc oxide films via aerosol assisted chemical vapour deposition. RSC Advances, **4**(91): p. 49723-49728, 2014.
106. YATES, H.M., et al., APCVD of dual layer transparent conductive oxides for photovoltaic applications. Thin Solid Films, **590**: p. 260-265, 2015.
107. RAY, N., et al., Deactivation of low temperature shift catalyst: part Ⅱ poisoning by chlorine. Journal of the research institute for catalysis Hokkaido University, **30**(1): p. 25-37, 1982.
108. PISCOPO, A., D. ROBERT, and J.V. WEBER. Influence of pH and chloride anion on the photocatalytic degradation of organic compounds Part I . Effect on the benzamide and para-hydroxybenzoic acid in TiO 2 aqueous solution. 2001.
109. KRIVEC, M., et al., The nature of chlorine-inhibition of photocatalytic degradation of dichloroacetic acid in a TiO2-based microreactor. Physical Chemistry Chemical Physics, **16**(28): p. 14867-14873, 2014.
110. CHAU, J.H.F., et al., Advanced photocatalytic degradation of acetaminophen using Cu2O/WO3/TiO2 ternary composite under solar irradiation. Catalysis Communications, **163**: p. 106396, 2022.
111. CALIMAN, L.B., Sinterização flash do condutor catiônico beta-alumina sintetizada pelo método dos precursores poliméricos, in Tese (Doutorado em Engenharia Metalúrgica e de Materiais) - Escola Politécnica. Universidade de São Paulo: São Paulo. p. 135. 2015.
112. LESSING, P.A., Mixed-Cation Oxide Powders Via Polymeric Precursors. American Ceramic Society Bulletin, **68**(5): p. 1002-1007, 1989.
113. LEE, H., et al., A novel approach to preparing nano-size Co3O4-coated Ni powder by the Pechini method for MCFC cathodes. Journal of Materials Chemistry, **13**(10): p. 2626-2632, 2003.
114. BARD, A.L., Electrochemical methods fundamentals and applications. New York: John Wiley & Sons. 2001. p. 1-864.
115. YOUNG, R.A., The Rietveld method. [Chester, England]; Oxford: International Union of Crystallograhy; Oxford University Press, 2002.
116. MONSHI, A., M.R. FOROUGHI, and M. MONSHI, Modified Scherrer Equation to Estimate More Accurately Nano-Crystallite Size Using XRD. World Journal of Nano Science and Engineering, **2**: p. 154-160, 2012.
117. DOLLIMORE, D., P. SPOONER, and A. TURNER, The bet method of analysis of gas adsorption data and its relevance to the calculation of surface areas. Surface Technology, **4**(2): p. 121-160, 1976.
118. SILVA, A.L.D., Anatase-Rutile Phase Stability and Photocatalytic Activity of Nb2O5-doped TiO2, in Centro Tecnológico. Universidade Federal de Santa Catarina: Florianópolis, SC - Brasil. p. 163, 2016.
119. WILLIAMS, D.B., C.B. CARTER, and J.C.H. SPENCE, Transmission electron microscopy. a textbook for materials science 1, 1. 2009.
120. CHINAGLIA, D.L., et al., Espectroscopia de impedância no laboratório de ensino. Revista Brasileira de Ensino de Física, **30**, 2008.
121. CALIMAN, L.B., et al., Flash sintering of ionic conductors: The need of a reversible electrochemical reaction. Journal of the European Ceramic Society, **36**(5): p. 1253-1260, 2016.

122. ASOKAN, T. and R. FREER, Grain and grain boundary conduction in zinc oxide varistors before and after DC degradation. Journal of the European Ceramic Society, **11**(6): p. 545-550, 1993.
123. URBAN, M.W., Vibrational spectroscopy of molecules and macromolecules on surfaces. Chichester: Wiley, 1994. p. 1-384.
124. CASTRO, R. and D. QUACH, Analysis of Anhydrous and Hydrated Surface Energies of Gamma-Al2O3 by Water Adsorption Microcalorimetry. The Journal of Physical Chemistry C, **116**: p. 24726–24733, 2012.
125. GANDELMAN, H., et al., Interface excess on Sb-doped TiO2 photocatalysts and its influence on photocatalytic activity. Ceramics International, **47**(1): p. 619-625, 2021.
126. DA SILVA, A.L., et al., Synthesis of TiO2 microspheres by ultrasonic spray pyrolysis and photocatalytic activity evaluation. Ceramics International, **48**(7): p. 9739-9745, 2022.
127. LIU, H., et al., Electrochemical impedance spectroscopy of ZnO nanostructures. Electrochemistry Communications, **11**(5): p. 945-949, 2009.
128. LAANE, J., Frontiers of Molecular Spectroscopy. Amsterdam, 2011. p. 1-740.
129. BARNARD, A.S. and P. ZAPOL, A model for the phase stability of arbitrary nanoparticles as a function of size and shape. The Journal of Chemical Physics, **121**(9): p. 4276-4283, 2004.
130. DIEHM, P.M., P. ÁGOSTON, and K. ALBE, Size-Dependent Lattice Expansion in Nanoparticles: Reality or Anomaly? ChemPhysChem, **13**(10): p. 2443-2454, 2012.
131. GANDELMAN, H., et al., Surface and grain boundary excess of ZnO-doped TiO2 anatase nanopowders. Ceramics International, **44**(10): p. 11390-11396, 2018.
132. ESCORIHUELA, L., et al., Molecular dynamics simulations of zinc oxide solubility: From bulk down to nanoparticles. Food and Chemical Toxicology, **112**: p. 518-525, 2018.
133. CHANG, C.-H., S. DEY, and R.H.R. CASTRO, Energetics of Oriented Attachment of Mn-Doped SnO2 Nanoparticles. The Journal of Physical Chemistry C, **119**(35): p. 20662-20672, 2015.
134. RENAUD, A., et al., Unravelling the origin of the giant Zn deficiency in wurtzite type ZnO nanoparticles. Scientific Reports, **5**(1): p. 12914, 2015.
135. LASIA, A., Electrochemical impedance spectroscopy and its applications. New York [etc.]: Springer. 2014. p. 1-369.
136. ANSARI, S.A., et al., Investigation on structural, optical and dielectric properties of Co doped ZnO nanoparticles synthesized by gel-combustion route. Materials Science and Engineering: B, **177**(5): p. 428-435, 2012.
137. REYNOLDS, D.C., C.W. LITTON, and T.C. COLLINS, Some Optical Properties of Group II–VI Semiconductors (II). physica status solidi (b), **12**(1): p. 3-55, 1965.
138. BAPTISTA, J.L. and P.Q. MANTAS, High Temperature Characterization of Electrical Barriers in ZnO Varistors*. Journal of Electroceramics, **4**(1): p. 215-224, 2000.
139. MAJOR, R.W., et al., Polarization currents in zinc oxide varistors from 77 to 450 K. Journal of Applied Physics, **76**(11): p. 7367-7371, 1994.
140. GODAVARTI, U., V.D. MOTE, and M. DASARI, Role of cobalt doping on the electrical conductivity of ZnO nanoparticles. Journal of Asian Ceramic Societies, **5**(4): p. 391-396, 2017.
141. XIA, C., et al., Study on Zinc Oxide-Based Electrolytes in Low-Temperature Solid Oxide Fuel Cells. Materials (Basel, Switzerland), **11**(1): p. 40, 2017.
142. LEE, J., et al., Impedance spectroscopy of grain boundaries in nanophase ZnO. Journal of Materials Research, **10**(9): p. 2295-2300, 2011.
143. MRAD, M., B. CHOUCHENE, and T.B. CHAABANE, Effects of zinc precursor, basicity and temperature on the aqueous synthesis of ZnO nanocrystals. South African Journal of Chemistry, **71**: p. 103-110, 2018.

144. NOEI, H., et al., The identification of hydroxyl groups on ZnO nanoparticles by infrared spectroscopy. Physical Chemistry Chemical Physics, **10**(47): p. 7092-7097, 2008.
145. EGBUCHUNAM, T. and D. BALKÖSE, Effect of Supercritical Ethanol Drying on the Properties of Zinc Oxide Nanoparticles. Drying Technology - DRY TECHNOL, **30**: p. 739-749, 2012.